Electronic Thesis and Dissertation Repository

4-4-2022 10:00 AM

A dislocation-based crystal plasticity model for hexagonal close-packed polycrystals

Omid Sedaghat, *The University of Western Ontario*

Supervisor: Abdolvand, Hamidreza, *The University of Western Ontario*
A thesis submitted in partial fulfillment of the requirements for the Doctor of Philosophy degree in Mechanical and Materials Engineering
© Omid Sedaghat 2022

Follow this and additional works at: https://ir.lib.uwo.ca/etd

Part of the Mechanics of Materials Commons, and the Nuclear Engineering Commons

Abstract

Due to their low neutron absorption cross-section and good corrosion properties, zirconium and its alloys have been widely used as the structural material in the core of nuclear reactors. These alloys are exposed to an intensive neutron flux which may lead to dimensional instabilities and the degradation of the mechanical properties of the alloy over the service time of the reactor. The changes in deformation behavior and mechanical properties can be traced back to the formation, evolution, and interaction of the irradiation-induced microstructural defects, e.g., point defect clusters, dislocation loops, and complex dislocation line networks. However, the materials constitutive models are rarely correlated to the irradiated-induced defects at the grain scale. Further, the available modeling approaches for simulating the deformation of irradiated materials are mostly empirical and generally do not incorporate the effects of microstructure or defect densities.

To simulate the mechanical behavior of zirconium alloys exposed to neutron radiation, the present research focuses on updating a crystal plasticity finite element model by firstly including the effects of dislocation densities. The results of the model are compared against previously published data for a series of in-situ neutron diffraction and high angular resolution electron backscatter diffraction (HR-EBSD) experiments conducted on un-irradiated α-zirconium specimens. The effects of implementing different formulations for determining dislocation densities are also investigated. It is shown that the calculated dislocation densities, stress, and rotation fields, as well as internal elastic strains, agree with the measured ones. The effects of irradiation growth are subsequently integrated into the model and the numerical results are compared to the previously published data. It is shown that the model is capable of determining the effects of material texture, grain size, and prior cold work on the evolution of average growth strain. It is shown, for the first time, that the growth strain is non-uniformly distributed among different grains and localized at the grain boundaries or slip bands.

Keywords

Summary for Lay Audience

When any engineering device is designed, there is a fundamental question that needs to be answered: Will the product fail under the operating condition? The answer to this question is extremely important, to ensure the safe operation of the engineering component. To accurately assess the life cycle of engineering components, there has been an increasing demand in advanced numerical models. In this research, we are updating and providing a physical-based numerical tool which can be used to simulate the deformation of nuclear reactor core components made of zirconium. The presented numerical model can help nuclear engineers understand the performance of nuclear reactors core components. The model links the effects of zirconium microstructure to its macroscopic mechanical behaviour. It simulates the localization of stress and strain fields that might affect the failure of engineering components.

Co-Authorship Statement

This thesis is presented in the manuscript format with four manuscripts, which are published or submitted for publication.

Chapter 3: O. Sedaghat, H. Abdolvand, A non-local crystal plasticity constitutive model for hexagonal close-packed polycrystals, Interntional Journal of Plasticity, 136 (2021) 102883. https://doi.org/10.1016/j.ijplas.2020.102883.

Author contributions: OS updated the CPFE model by adding a strain-gradient hardening law. OS conducted all simulations, prepared the first draft of the manuscript and all figures presented. HA developed the original model, the implemented formulation, and the nonlocal subroutines. HA conducted the HR-BESD experiments.

Chapter 4: O. Sedaghat, H. Abdolvand, Strain-gradient crystal plasticity finite element modeling of slip band formation in α-zirconium, Crystals. 11 (2021). https://doi.org/10.3390/cryst11111382.

Author contributions: OS updated the CPFE model by adding a strain-gradient hardening law. OS conducted all simulations, prepared the first draft of the manuscript and all figures presented. HA developed the original model and the nonlocal subroutines. HA conducted the HR-BESD experiments.

Chapter 5: O. Sedaghat, H. Abdolvand, Dislocation-based crystal plasticity finite element modeling of irradiation growth in α-zirconium, Submitted.

Author contributions: OS updated the CPFE model by integrating an irradiation subroutine to the strain-gradient model. OS conducted all simulations, prepared the first draft of the manuscript, and all figures presented. HA developed the original model and the nonlocal subroutines.

Chapter 6: H. Abdolvand, O. Sedaghat, Y. Guo, Nucleation and growth of $\{11\bar{2}2\}$ twins in titanium: Elastic energy and stress fields at the vicinity of twins, Materialia. 2 (2018). https://doi.org/10.1016/j.mtla.2018.06.012.

Acknowledgments

Table of Contents

List of Tables

List of Figures

List of Abbreviations

BCC	Body-centered cubic
CPFE	Crystal plasticity finite element
CRSS	Critical resolved shear stress
DD	Dislocation dynamics
EBSD	Electron backscatter diffraction
FCC	Face-centered cubic
FE	Finite element
FFT	Fast Fourier transform
GND	Geometrically necessary dislocation
HCP	Hexagonal close-packed
HR-EBSD	High angular resolution electron backscatter diffraction
IP	Integration point
MD	Molecular dynamics
ND	Normal direction
RD	Rolling direction
RSS	Resolved shear stress
SDV	Solution dependent state variables
SEM	Scanning electron microscopy
SSD	Statistically stored dislocation
TD	Transverse direction
TEM	Transmission electron microscopy
UMAT	User material

List of Symbols

F	Total deformation gradient tensor
F^e	Elastic part of deformation gradient tensor
F^p	Plastic part of deformation gradient tensor
L	Total velocity gradient tensor
L^e	Elastic part of velocity gradient tensor
L^p	Plastic part of velocity gradient tensor
D	Deformation rate tensor
Ω	Spin tensor
P^α	Symmetric part of the Schmid tensor
W^α	Asymmetric part of the Schmid tensor
ψ	Kirchhoff stress tensor
$\breve{\psi}$	Jaumann rate of Kirchhoff stress
σ	Global Cauchy stress tensor
σ^L	Local stress
ε	Strain tensor
S^α	Schmid tensor
$\dot{\gamma}^\alpha$	Shear rate of αth slip system
$\vec{m}^\alpha$	Slip direction of αth slip system
$\vec{n}^\alpha$	Slip plane normal of αth slip system
$\dot{\gamma}_0^\alpha$	Reference shear strain rate
τ^α	Resolved shear stress of the αth slip system
g^α	Critical resolved shear stress of the αth slip system
$\mathbb{C}$	Elastic stiffness tensor
g_0^α	Initial critical resolved shear stress of the αth slip system
θ_1^α	Asymptotic hardening rate of the αth slip system
θ_0^α	Initial hardening rate of the αth slip system
g_1^α	A parameter for critical resolved shear stress of the αth slip system
Γ	Accumulated shear strain on all slip systems
H^α	Hall-Petch parameter of the αth slip system
ζ	A material constant
G	shear modulus
b^α	Size of the Burgers vector
$q^{\alpha\beta}$	Hardening matrix
δ_{ij}	Kronocker delta
ρ_{GND}^α	GND density of αth slip system
ρ_{SSD}^α	SSD density of αth slip system
t^α	Dislocation line vector of αth slip system
K^α	Accumulation constant of SSDs of αth slip system
y_c^α	Critical annihilation length of the dislocations of αth slip system
ϵ_{irq}	Permutation tensor
N^i	Element shape function
ξ_i	Local element coordinate system
x_i	Global element coordinate system
E	Elastic energy

$\boldsymbol{\omega}$	Rotation tenor
$\varphi_{v,i}^{a,max}$	Irradiation dose at the end of the nucleation stage for the prismatic loops
$N_{v,i}^{a,\,max}$	The maximum density of prismatic loops
φ_{v0}^{c}	Irradiation dose at the start of the nucleation stage for the basal loops
$\varphi_{v}^{c,max}$	Irradiation dose at the end of the nucleation stage for the basal loops
$N_{v}^{c,max}$	The maximum density of basal loops
A	A dimensionless parameter for the evolution of basal loop density
r_{cd}	Capture radius of dislocations for interstitial clusters
f_{cl}^{i}	Fraction of the interstitial point defects which are clustered
D_i	Diffusivity of interstitial point defects
D_v	Diffusivity of vacancy point defects
C_i	Concentration of the interstitial point defects
C_v	Concentration of the vacancy point defects
D_{cl}	Diffusivity of the interstitial clusters
C_{cl}	Concentration of the interstitial clusters
K_{cl}^{2}	Sink strength of the interstitial clusters
K_{GB}	Sink strength of the grain boundary
ρ_j	Total dislocation density
N_i^{j}	Interstitial loop number density
N_v^{j}	Vacancy loop number density
r_i^{j}	Interstitial loop radius
r_v^{j}	Vacancy loop radius
r_{cd}	Capture radius of dislocations for interstitial clusters
f_c	Fraction of the point defects that are recombined
f_i^{cl}	Fraction of the interstitial point defects which are clustered
k_v^{2}	Sink strength of vacancy loops for interstitial clusters
k_i^{2}	Sink strength of interstitial loops for interstitial clusters
r_{cvl}	Capture radius of vacancy type prismatic loops for clusters
r_{cil}	Capture radius of interstitial type prismatic loops for clusters

Chapter 1

1   Introduction

1.1   Background

Hexagonal close-packed (HCP) zirconium polycrystals are used in fuel assemblies of nuclear reactors, due to their good corrosion and creep resistance as well as their low neutron absorption cross section [1]. During the operation of nuclear reactors, zirconium alloys are exposed to an intensive neutron flux from the fission of uranium atoms. During neutron irradiation, the atoms of zirconium are displaced and different types of nano-scale defects, e.g., point defects, interstitial clusters, and dislocation loops are formed. The interaction of dislocation lines and loops with the irradiation-induced defects affects the mechanical properties of the alloys during the lifetime of the reactors.

The interaction between neutrons and zirconium atoms can cause irradiation hardening, irradiation softening, irradiation growth, and irradiation-enhanced creep [2–4]. Irradiation hardening happens when the microstructural defects, introduced by irradiation, impede the movement of dislocations during plastic deformation [2]. Irradiation hardening increases the flow stress of zirconium alloys. At higher applied stresses, the resolved shear stress acting on dislocations will be high enough to overcome the internal forces induced by radiation defects. At this stage, dislocations move through and annihilate a portion of the existing defects, leading to a phenomenon known as irradiation softening [5]. The localized plastic deformation can cause crack initiation and failure of the irradiated material [6].

High energy neutrons can cause formation of two different types of dislocation loops in HCP zirconium: interstitial loops and vacancy loops [2–4]. Formation of these loops is

respectively accompanied by the expansion and contraction of the HCP crystal along its c- and a-axis. That is, an anisotropic dimensional change takes place in the HCP crystal, even in the absence of an externally applied load- this is called irradiation growth. Irradiation growth is significantly affected by the texture and microstructure of the zirconium polycrystal, as well as the amount of prior cold-work [4]. In the presence of an externally applied load, irradiation-enhanced creep may take place due to the strong interaction between dislocations and the internal forces from irradiation-induced point defects.

1.2 Motivation

Due to the aging of nuclear reactors, understanding the mechanisms that control the performance of reactors core components have become important. For example, in CANada Deuterium Uranium (CANDU) reactors, irradiation-induced creep can lead to the excessive dimensional change of the fuel channel assembly. Although the separation between the pressure tube and calandria tube is maintained by the use of garter spring spacers, the excessive sag of pressure tubes can lead to the contact between the hot pressure tube and the cold calandria tube [7,8]. This contact leads to the deuterium ingress into the zirconium lattice, which can result in the formation of hydride blisters and cracking of the pressure tube [9].

The accurate determination of materials lifetime requires the development of numerical methods that can simulate the "true" deformation mechanisms of the material, even in the presence of neutron irradiation. As such, the present research focuses on the updating a crystal plasticity finite element (CPFE) model to include the effects of line defects and their interactions with the irradiation-induced point defects. The CPFE model is a user material (UMAT) subroutine that links to finite element solvers.

1.3 Objectives

This research aims to update a CPFE model to study the mechanical behavior of HCP zirconium alloys exposed to neutron irradiation. Due to the presence of many different mechanisms, the main attention is given to the evolution of dislocation densities in the absence of neutron irradiation, as well as including the effects of irradiation growth. Hence, the following research objectives are determined:

1. Adding the effects of dislocation line densities, i.e., geometrically necessary dislocations (GNDs) and statically stored dislocations (SSDs) to the CPFE model.
2. Studying the capability of the updated model in simulating the formation of slip bands and localized plastic zones for un-irradiated HCP zirconium polycrystals.
3. Incorporating the effects of irradiation growth and irradiation hardening to the model and studying their subsequent effects on the development of localized strain fields at the grain scale.

1.4 Structure of the thesis

After an introduction in Chapter 1, a literature review is provided in Chapter 2. The rest of the thesis is presented in a manuscript-format. Chapter 3 discusses the steps taken for updating the CPFE model by integrating the densities of GNDs and SSDs. The updated model is used to replicate the previously published data for in-situ neutron diffraction experiments [11] as well as high resolution electron backscatter diffraction experiments [12]. HCP zirconium polycrystals are used for the numerical simulations and experimental measurements. Chapter 3 is published in the International Journal of Plasticity [10]. Chapter 4 discusses the results of the model for using different methods for determining dislocation densities. The capability of each method in simulating the formation of slip bands is discussed. Chapter 4 is published in Crystals [13]. Chapter 5

discusses the steps taken for adding irradiation growth to the CPFE model. Previously published experimental data for single crystals [14] and polycrystalline specimens [15] are used for model validation. Chapter 6 represents the initial attempt taken to understand the structure of the original CPFE model, which includes a study on how twins form in a titanium micro-pillar. The results of the model are compared with those measured during an in-situ high resolution electron backscatter diffraction experiment. This chapter is also published in Materialia [16]. Finally, Chapter 7 includes the conclusions made in previous chapters and discusses the possible future studies.

References

[1]   K.L. Murty, I. Charit, Texture development and anisotropic deformation of zircaloys, Prog. Nucl. Energy. 48 (2006) 325–359. https://doi.org/10.1016/j.pnucene.2005.09.011.

[2]   G.S. Was, Fundamentals of Radiation Material Science: Metals and Alloys, Springer, Berlin, 2007.

[3]   M. Griffiths, R.A. Holt, A. Rogerson, Microstructural aspects of accelerated deformation of Zircaloy nuclear reactor components during service, J. Nucl. Mater. 225 (1995) 245–258. https://doi.org/10.1016/0022-3115(94)00687-3.

[4]   R.B. Adamson, C.E. Coleman, M. Griffiths, Irradiation creep and growth of zirconium alloys: A critical review, J. Nucl. Mater. 521 (2019) 167–244. https://doi.org/10.1016/j.jnucmat.2019.04.021.

[5]   F. Onimus, C. Prioul, P. Pilvin, A statistical TEM investigation of dislocation channeling mechanism in neutron irradiated zirconium alloys, J. Nucl. Mater. 328 (2004) 165–179. https://doi.org/10.1016/j.jnucmat.2004.04.337.

[6]   M.D. McMurtrey, B. Cui, I. Robertson, D. Farkas, G.S. Was, Mechanism of dislocation channel-induced irradiation assisted stress corrosion crack initiation in austenitic stainless steel, Curr. Opin. Solid State Mater. Sci. 19 (2015) 305–314. https://doi.org/10.1016/j.cossms.2015.04.001.

[7]   E.G. Price, Highlights of the Metallurgical Behaviour of Candu Pressure Tubes.,

At. Energy Canada Limited, AECL. (1984).

[8]   S.R. Prabhu, M.D. Pandey, N. Christodoulou, An efficient method for probabilistic finite element analysis with application to contact assessment of CANDU fuel channels, Nucl. Eng. Des. 387 (2022) 111609. https://doi.org/10.1016/j.nucengdes.2021.111609.

[9]   R.N. Singh, R. Kishore, T.K. Sinha, B.P. Kashyap, Hydride blister formation in Zr-2.5wt%Nb pressure tube alloy, J. Nucl. Mater. 301 (2002) 153–164. https://doi.org/10.1016/S0022-3115(02)00708-0.

[10]   O. Sedaghat, H. Abdolvand, A non-local crystal plasticity constitutive model for hexagonal close-packed polycrystals, Int. J. Plast. 136 (2021) 102883.

[11]   F. Xu, R.A. Holt, M.R. Daymond, Modeling lattice strain evolution during uniaxial deformation of textured Zircaloy-2, Acta Mater. 56 (2008) 3672–3687. https://doi.org/10.1016/j.actamat.2008.04.019.

[12]   H. Abdolvand, A.J. Wilkinson, On the effects of reorientation and shear transfer during twin formation : Comparison between high resolution electron backscatter diffraction experiments and a crystal plasticity finite element model, Int. J. Plast. 84 (2016) 160–182. https://doi.org/10.1016/j.ijplas.2016.05.006.

[13]   O. Sedaghat, H. Abdolvand, Strain-gradient crystal plasticity finite element modeling of slip band formation in α-zirconium, Crystals. 11 (2021). https://doi.org/10.3390/cryst11111382.

[14]   G.J.C. Carpenter, R. Zee, A. Rogerson, Irradiation Growth of Zirconium Single-Crystals - a Review, J. Nucl. Mater. 159 (1988) 86–100. https://doi.org/10.1016/0022-3115(88)90087-6.

[15]   A. Rogerson, Irradiation growth in annealed and 25% cold-worked Zircaloy-2 between 353-673 K, J. Nucl. Mater. 154 (1988) 276–285. https://doi.org/10.1016/0022-3115(88)90364-9.

[16]   H. Abdolvand, O. Sedaghat, Y. Guo, Nucleation and growth of $\{11\bar{2}2\}$ twins in titanium: Elastic energy and stress fields at the vicinity of twins, Materialia. 2 (2018). https://doi.org/10.1016/j.mtla.2018.06.012.

Chapter 2

2 Literature review

This chapter focuses on providing a literature review of the modeling attempts done so far for understanding deformation mechanisms of polycrystalline materials exposed to neutron irradiation. Attention is given to α-zirconium alloys. Crystal plasticity finite element (CPFE) is firstly introduced since it is the main methodology used in this thesis. A comparison between the conventional and non-local CPFE approaches is provided which is followed by an introduction to the experimental techniques used for model validation. In addition, the published numerical and experimental studies focusing on the deformation mechanisms of zirconium alloys under irradiation are reviewed. Lastly, the knowledge gap in the literature is highlighted for further investigation in this thesis.

2.1 Modeling frameworks

Generally, two approaches are used for modeling irradiation damage: empirical and mechanistic. Empirical models are mainly based on curve fitting and rely excessively on the measured experimental data. For example, in the study conducted by Franklin, an empirical model was proposed to determine irradiation growth strain as a function of fast-neutron fluence [1]. Further, Limback formulated an empirical irradiation creep model with considering the effects of stress, temperature and irradiation doze on the creep rate of in-reactor materials [2]. Although these models account for texture, irradiation dose, and temperature effects on the material deformation, none of them incorporate the mechanistic basis or the explicit effects of microstructural features. Therefore, these empirical models are solely valid for the range of the temperatures or stresses that their parameters are fitted for [3]. More importantly, the interaction between crystallographic texture, grain morphologies, and irradiation damage is neglected [1].

The other approach is the physically-based mechanistic approach that incorporates the micromechanics of plastic deformation under irradiation condition. Molecular dynamics (MD) and dislocation dynamics (DD) are two nano-scale approaches used to understand the interaction between dislocations with point defects, as well as to calculate their densities or distributions during irradiation cascades [4–10]. For instance, Subramanian et al. used an MD approach to study the absorption rate of interstitials and vacancies by various sinks such as dislocations and grain boundaries [6]. Such atomistic simulations provide valuable information for better understanding the nature of interaction between point defects and line defects. However, MD and DD simulation of polycrystals are computationally costly for engineering length scales or even impossible for large strains. In addition, the time scale of these atomistic-level methods is in the order of microseconds, which is not representative of what happens in a nuclear reactor.

2.2   Conventional crystal plasticity

Crystal plasticity is a set of constitutive equations that can be used to study heterogeneous deformation of individual or clusters of grains. It is a meso-scale modeling approach, where plastic strain is calculated by determining the slip that occurs on all possible active slip systems. The model scale can vary from a couple of nanometers within a grain to a couple of millimeters that represent thousands of grains. Therefore, each calculation (integration) point can represent a dislocation, group of dislocations, or even an entire grain. Hence, crystal plasticity model is one of the few existing numerical methods that can be used to study deformation across length scales.

Crystal plasticity has been implemented in different frameworks, e.g., self-consistent [11], fast Fourier transform (FFT) [12,13], and finite element (FE) [14,15]. In the self-consistent framework, each grain interacts with a homogenous medium that represents the average properties of the polycrystal except for the grain that is investigated.

Although this framework is naturally fast, the "true" interaction among neighboring grains is ignored. However, such interactions can be investigated using FFT or FE frameworks [16–19]. For example, local stress variations, stress concentration within individual grain, and the effects of local neighborhood on the response of each grain are studied using crystal plasticity finite element (CPFE) analysis [16,18,20].

CPFE modeling framework suffers from several limitations. Firstly, since the crystal plasticity is a meso-scale technique, it not capable to capture the nano-scale effects, e.g. interaction between individual dislocations or other atomistic scale defects. In addition, the macro-scale quantities need to be averaged over a large number of grains and elements, which makes the CPFE framework computationally expensive. Finally, comparing to the empirical models, the constitutive equations are more complicated, which makes the implementation of the equations more difficult.

Plastic deformation in zirconium polycrystals is accommodated by slip or twinning, depending on the crystal orientation and applied loading condition. For slip to occur, dislocations should overcome both short-range and long-range obstacles. The primary short-range obstacles are generally assumed to be the other dislocations that intersect the slip plane and impede the movement of dislocations. On the other hand, the long-range obstacles may include the elastic stress fields due to grain boundaries or far field dislocations and defects. While the short-range obstacles can mainly be overcome by thermal activation, the long-range obstacles are generally independent from temperature and can be overcome by increasing the resolved shear stress (RSS) that acts on the slip system [21]. Many studies have attempted to incorporate the effects of both short- and long-range obstacles in material hardening models within the crystal plasticity framework [22,23]. For example, Evers et al. assumed that the resistance induced by the long-range obstacles is a function of the spatial gradient of geometrically necessary dislocations

(GND) densities, while that of short-range obstacles was assumed to be dependent on both total GND and statistically stored dislocation (SSD) densities [23]. Therefore, it was assumed that SSDs do not have any long-range effects, while the evolution of both SSDs and GNDs during crystallographic slip equally increase the short-range interactions [23,24]. In the conventional form of crystal plasticity, no differentiation is made between the two types of obstacles and the critical resolved shear stress (CRSS) required for dislocation movement solely depends on the state of deformation in the current calculation point.

2.3   Non-local crystal plasticity

In the "non-local" crystal plasticity framework, dislocation densities are calculated based on the gradients of the plastic strain; such gradients depend on the deformation of the neighboring regions. Therefore, both short- and long-range effects can be introduced using the non-local approach [25–30]. This framework is also called strain-gradient crystal plasticity. Since non-local crystal plasticity models are based on strain gradient theory, unlike the conventional crystal plasticity, it is possible to study the geometrical "size effects" [31,32].

Two forms of non-local plasticity theories are available in the literature: the lower-order and higher-order theories [33]. In the lower-order form [34–36], the effects of strain gradients are only included in the materials hardening laws. In this form, the force-equilibrium equations or boundary conditions are not affected by the strain gradient effects. This approach is usually implemented in crystal plasticity framework by determining GND densities based on the gradient of the plastic strain. It is generally incorporated into the materials hardening equations. The drawback of this approach is that it may result in unrealistic higher strain gradients and formation of unusual localized deformation fields [33]. In the higher-order non-local plasticity theory [37–40], both

materials hardening law as well as force-equilibrium equations are modified by introducing an extra term which represents localized micro-scale stresses. The micro-scale stress terms depend on the second order gradient of the plastic strain. In order to solve the modified force-equilibrium equations, additional boundary conditions are generally required.

In the lower-order strain gradient crystal plasticity models, the non-local effects are taken into account by introducing the GND density term into the material hardening equation. During plastic deformation, GNDs are formed as a result of the lattice curvature and their densities can be determined using the gradients of plastic strain [41]. The derivation of dislocation densities from the "curl" of the deformation gradient in the Nye equation has been accompanied with inconsistencies in the literature, some of which have been reported by Das et al. [42]. Two methods are generally used in the literature for extracting GNDs using Nye equations. In the first method, the contribution of each slip system, e.g. α, to GND density is assumed to be proportional to the plastic shear accommodated on the same slip system α. Hence, the number of linear equations that should be solved is equal to the number of unknowns, i.e., GNDs on each slip system α. This is called the direct method where the density of GNDs on each slip system is determined unambiguously. The direct method was initially proposed by Dai [43] and was subsequently implemented in the CPFE models [23,31,35,44,45]. In the second method, the cumulative contribution of plastic shears on all slip systems to the total GND densities on all slip systems is assumed to be proportional to the Nye tensor [46-49]. This usually results in an under-determined system of equations where the number of unknowns is more than the number of equations. In contrast to the direct method which provides a unique solution for the GND density on each slip system, the minimization approach leads to non-unique solutions. Therefore, an investigation is required to

compare the magnitudes and distributions of the obtained GND densities from these two methods.

2.4   Experimental diffraction methods

Diffraction based experimental techniques are mainly used for measuring internal or localized stress and strain fields as well as the density of dislocations. In this section, neutron diffraction and high angular resolution electron backscatter diffraction (HR-EBSD) techniques are briefly introduced. The results of the previously conducted experiments using these two techniques are used in this thesis to validate the developed CPFE model.

Neutron diffraction is an experimental technique that can be used to measure internal elastic lattice strains in polycrystalline materials [50,51]. In this technique, the thermal neutrons with wavelength close to lattice spacing can penetrate up to several centimeters. Contribution of large volume and number of grains is an advantage of this method, which is useful for measuring the average mechanical behavior of a polycrystalline material. The spacing between different lattice planes can be determined using the Bragg`s law [52-53]. Accordingly, the lattice strain, which is the elastic strain inside a group of grains that satisfy the Bragg condition for an incident beam, can be measured. The deflections observed in lattice strains correspond to activation of various slip or twinning modes of deformation. This property of lattice strains can be used to study deformation mechanism of polycrystals.

Electron backscatter diffraction (EBSD) is an experimental technique that can be used to measure the orientations of the grains located at the surface of polycrystals. Briefly, in a scanning electron microscope, backscattered electrons can form Kikuchi bands on the EBSD detector. Kikuchi bands can be used to define orientation of each crystal. With

HR-EBSD technique, it is possible to measure elastic strains, stresses, and GND densities in many grains, yet close to the sample surface. For this purpose, the Kikuchi diffraction patterns measured within a grain are cross correlated with respect to a pattern collected at a reference point within the same grain. The displacement gradient can subsequently be calculated and used to extract the "relative" elastic strain and lattice rotation fields. Assuming that the stress normal to surface is zero, it is possible to calculate the "relative" stress tensor [54–56]. Since the "relative" elastic lattice rotations are known, it is also possible to calculate GND densities using Nye tensor [57].

2.5   Deformation mechanisms

2.5.1   Slip and twinning

Deformation by slip and twinning are reported to be the two main plastic deformation mechanism of zirconium alloys at room temperature. Slip in HCP zirconium is generally controlled by 18 slip systems, i.e. three prism ($\{10\bar{1}0\}, \langle11\bar{2}0\rangle$), three basal ($\{0001\}, \langle11\bar{2}0\rangle$) and twelve pyramidal <c+a> ($\{10\bar{1}1\}, \langle11\bar{2}3\rangle$) [58]. The twinning systems for HCP zirconium are $\{10\bar{1}2\}\langle10\bar{1}1\rangle$ and $\{11\bar{2}1\}\langle11\bar{2}6\rangle$ during tension and $\{10\bar{1}1\}\langle10\bar{1}2\rangle$ and $\{11\bar{2}2\}\langle11\bar{2}3\rangle$ during contraction [58]. The $\{10\bar{1}2\}\langle10\bar{1}1\rangle$ tensile twinning is reportedly the most active twinning system.

2.5.2   Irradiation growth

Over the last decades, many experimental studies have been conducted to investigate the effects of irradiation damage on the deformation mechanisms of zirconium alloys [59]. In this section, the studies associated with the irradiation growth are reviewed. Irradiation growth strain is affected by neutrons fluence and energy, the operating temperature of the reactor, as well as zirconium's composition, texture, prior cold work, and average grain size. The role of grain boundaries as sinks for irradiation-induced defects was

investigated by Rogerson, where it was shown that irradiation growth in annealed polycrystalline zirconium is significantly greater than that of single crystals [60]. In another study by Fidleris [61], it was shown that irradiation growth increases with decreasing the average grain size in annealed polycrystalline zirconium. This grain size dependency of the irradiation growth was also reported by Murgatroyd and Rogerson [62]. Cann et al. [63] showed that for the polycrytals with the grain sizes bigger than 50 μm, the growth strain may not be affected by grain size anymore. The growth strain of the zirconium is also significantly affected by the prior cold work. An experimental study by Rogerson showed that cold-worked specimens with smaller grain sizes have significantly higher growth strains compared to annealed ones with bigger grains [60]. In addition, it was shown that the irradiation growth strain increases with cold working [64,65]. Although macroscale measurements are conducted to study the evolution of irradiation growth strain, there is not many grain scale experimental data for the growth strain at. Modeling techniques can be helpful for such cases.

Irradiation growth models have primarily been developed based on a rate-theory approach [5,66–69]. A comprehensive review of the various physically-based irradiation growth models is provided in [59]. Most of these models are based on a simple assumption that the primary damage in the atomic scale is in the form of Frenkel pairs, i.e., equal number of vacancy and interstitial point defects are generated as a result of the collision cascade. That is, the formation of clusters is neglected in these models. However, MD simulations have shown that a large number of interstitial point defects are found in small clusters [70]. Accordingly, a reaction-diffusion model for irradiation growth of HCP materials was proposed by Golubov et al. [69]. In this model, the evolution of vacancy and interstitial loops follows a dose-dependent formulation, resulting in a dose-dependent irradiation growth model for single crystal HCP zirconium. This model was implemented in a self-consistent crystal plasticity framework to study the

evolution of grain-average growth strain [71]. It was shown that the effects of texture and grain size on the calculated growth strain are significant. However, the possible effects of the local grain neighborhood were ignored. In addition, the distribution of growth strain between and within grains was not studied. Such studies can be conducted in dislocation-based CPFE models.

2.5.3   Irradiation hardening and softening

There have been extensive experimental studies to understand the effects of irradiation damage on the deformation by slip in zirconium [72–77]. For example, Cogez et al., conducted uniaxial tensile experiments on a set of neutron irradiated Zircaloy-2 samples with different neutron fluences and measured the macroscopic stress strain curves [73]. Long et al. measured not only the average stress-strain curves, but also the elastic lattice strains of neutron irradiated Zr-2.5Nb polycrystal using the neutron diffraction technique [77]. Balough et al. measured the development of the polycrystal average dislocation density during a post-irradiation uniaxial tensile test for a Zr-2.5Nb polycrystal using neutron diffraction line profile analysis [72]. It was shown that while plastic deformation of non-irradiated material equally increases the dislocation density on all slip systems, post irradiation plastic deformation only increases the pyramidal type dislocation densities. In another study by Qiang et al., Zr-2.5Nb sample was irradiated by Zr ions, followed by nano-indentation tests [75]. It was shown that the yield stress of the irradiated sample is more effected when the indentation is along the direction where the prism and basal slip systems are the dominant ones.

Several numerical studies have been recently conducted to account for the effects of irradiation defects using crystal plasticity modeling [78–84]. A few of them, however, have simulated irradiated zirconium alloys, e.g., [80,81,85]. Although modeling irradiation hardening is rather straightforward, different models have been proposed in

the literature for irradiation softening. For example, a CPFE model is used to simulate strain localization due to irradiation softening in body-centered cubic (BCC) iron by Barton et al. [78], and in BCC steel by Patra and McDowell [79]. In both models, the dislocation loop annihilation rate depends on the current dislocation loop density accumulated on each slip system and the resolved shear strain rate on the same slip system. Similarly, Erinosho and Dunne [80] used a CPFE framework to study irradiation softening effects in HCP zirconium. In their model, the strength of slip systems was approximated using a linear relationship with respect to the accumulated resolved shear strain. Recently, Onimus et al. [81] have incorporated the effects of irradiation softening of zirconium in a self-consistent framework . In this model, the evolution law for dislocation loop density was formulated as a function of shear strain and current dislocation loop density.

2.6   The knowledge gaps

The available macro-scale models used for simulating zirconium alloys are mostly empirical. Depending on the complexity of the proposed empirical model, a large number of parameters need to be calibrated by fitting the parameters against extensive data sets that are mainly measured at "macro-scales". Therefore, these models do not incorporate the true deformation mechanism of zirconium alloys and are solely valid over the range of the temperatures, doses, or deformation rates, that their parameters are fitted. Further, although the MD or DD nano-scale models provide valuable insights toward understanding the interaction between line and point defects, they are rarely capable of modeling deformation of zirconium for their real service time or at engineering length scales. Hence, there is a need to develop physical based meso-scale models to link the scales and to study the various effects of irradiation-induced defects.

Several studies have focused on incorporating dislocation-based crystal plasticity constitutive models in the self-consistent framework to investigate the effects of neutron irradiation on the plastic deformation of HCP zirconium. However, it is not possible to study grain-grain interaction in the self-consistent framework. In addition, the effects of strain or stress localization are not included in this mesoscale modeling framework. Hence, this thesis focuses on adding the effects of dislocation densities into a CPFE model to study such grain-grain interactions and strain or stress localization in the presence or absence of irradiation growth in HCP zirconium polycrystals.

References

[1] D. G. Franklin, Zircaloy-4 Cladding Deformation during Power Reactor Irradiation, in: ASTM STP 754, Am. Soc. Test. Mater., 1982: pp. 235–267.

[2] M. Limbäck, T. Andersson, A Model for Analysis of the Effect of Final Annealing on the In and Out-of-Reactor Creep Behavior of Zircaloy Cladding, in: Zircon. Nucl. Ind. Elev. Int. Symp. Int. Symp., 1990: pp. 448–468.

[3] R. Montgomery, C. Tomé, W. Liu, A. Alankar, G. Subramanian, C. Stanek, Use of multiscale zirconium alloy deformation models in nuclear fuel behavior analysis, J. Comput. Phys. 328 (2017) 278–300. https://doi.org/10.1016/j.jcp.2016.09.051.

[4] F. Christien, A. Barbu, Cluster Dynamics modelling of irradiation growth of zirconium single crystals, J. Nucl. Mater. 393 (2009) 153–161. https://doi.org/10.1016/j.jnucmat.2009.05.016.

[5] R.A. Holt, C.H. Woo, C.K. Chow, Production bias - a potential driving force for irradiation growth, J. Nucl. Mater. 205 (1993) 293–300. https://doi.org/10.1016/0022-3115(93)90092-D.

[6] G. Subramanian, C. Tome, Progress report on the incorporation of lower lengthscales into polycrystal plasticity models, Los Alamos Report, LA-UR 12-25613, 2012.

[7] Y. Li, N. Ghoniem, Cluster dynamics modeling of irradiation growth in single crystal Zr, J. Nucl. Mater. 540 (2020) 152312.

https://doi.org/10.1016/j.jnucmat.2020.152312.

[8]   M.E. Cazado, E. Goldberg, M.A. Togneri, A. Denis, A. Soba, A new irradiation growth model for Zr-based components of nuclear reactors for the DIONISIO code, Nucl. Eng. Des. 373 (2021) 111009. https://doi.org/10.1016/j.nucengdes.2020.111009.

[9]   F. Christien, A. Barbu, Effect of self-interstitial diffusion anisotropy in electron-irradiated zirconium: A cluster dynamics modeling, J. Nucl. Mater. 346 (2005) 272–281. https://doi.org/10.1016/j.jnucmat.2005.06.024.

[10]   S. Il Choi, G.G. Lee, J. Kwon, J.H. Kim, Modeling of sink-induced irradiation growth of single-crystal and polycrystal zirconiums in nuclear reactors, J. Nucl. Mater. 468 (2016) 56–70. https://doi.org/10.1016/j.jnucmat.2015.11.014.

[11]   C. Mareau, M.R. Daymond, Study of internal strain evolution in Zircaloy-2 using polycrystalline models : Comparison between a rate-dependent and a rate-independent formulation, Acta Mater. 58 (2010) 3313–3325. https://doi.org/10.1016/j.actamat.2010.02.005.

[12]   R.A. Lebensohn, A. Needleman, Numerical implementation of non-local polycrystal plasticity using fast Fourier transforms, J. Mech. Phys. Solids. 97 (2016) 333–351. https://doi.org/10.1016/j.jmps.2016.03.023.

[13]   H. Wang, P.D. Wu, J. Wang, C.N. Tomé, A crystal plasticity model for hexagonal close packed (HCP) crystals including twinning and de-twinning mechanisms, Int. J. Plast. 49 (2013) 36–52. https://doi.org/10.1016/j.ijplas.2013.02.016.

[14]   A. Patra, D.L. Mcdowell, Acta Materialia Crystal plasticity investigation of the microstructural factors in fl uencing dislocation channeling in a model irradiated bcc material, Acta Mater. 110 (2016) 364–376. https://doi.org/10.1016/j.actamat.2016.03.041.

[15]   H. Abdolvand, Progressive modelling and experimentation of hydrogen diffusion and precipitation in anisotropic polycrystals, Int. J. Plast. 116 (2019) 39–61. https://doi.org/10.1016/j.ijplas.2018.12.005.

[16]   P.W. Liu, Z. Wang, Y.H. Xiao, R.A. Lebensohn, Y.C. Liu, M.F. Horstemeyer, X.Y. Cui, L. Chen, Integration of phase-field model and crystal plasticity for the prediction of process-structure-property relation of additively manufactured metallic materials, Int. J. Plast. 128 (2020) 102670.

https://doi.org/10.1016/j.ijplas.2020.102670.

[17] S. Berbenni, V. Taupin, R.A. Lebensohn, A fast Fourier transform-based mesoscale field dislocation mechanics study of grain size effects and reversible plasticity in polycrystals R, J. Mech. Phys. Solids. 135 (2020) 1–23. https://doi.org/10.1016/j.jmps.2019.103808.

[18] A. Eghtesad, K. Germaschewski, R.A. Lebensohn, M. Knezevic, A multi-GPU implementation of a full-field crystal plasticity solver for efficient modeling of high-resolution microstructures, Comput. Phys. Commun. 254 (2020) 107231. https://doi.org/10.1016/j.cpc.2020.107231.

[19] C. Mareau, M.R. Daymond, Micromechanical modelling of twinning in polycrystalline materials : Application to magnesium, Int. J. Plast. 85 (2016) 156–171. https://doi.org/10.1016/j.ijplas.2016.07.007.

[20] H. Abdolvand, J. Wright, A. Wilkinson, Strong grain neighbour effects in polycrystals, Nat. Commun. 9, 171 (2018). https://doi.org/10.1038/s41467-017-02213-9.

[21] S. Nemat-nasser, L. Ni, T. Okinaka, A constitutive model for fcc crystals with application to polycrystalline OFHC copper, Mech. Mater. 30 (1998) 325–341.

[22] X. Lu, X. Zhang, M. Shi, F. Roters, G. Kang, Dislocation mechanism based size-dependent crystal plasticity modeling and simulation of gradient nano-grained copper, Int. J. Plast. 113 (2019) 52–73. https://doi.org/10.1016/j.ijplas.2018.09.007.

[23] L.P. Evers, W.A.M. Brekelmans, M.G.D. Geers, Non-local crystal plasticity model with intrinsic SSD and GND effects, J. Mech. Phys. Solids. 52 (2004) 2379–2401. https://doi.org/10.1016/j.jmps.2004.03.007.

[24] U.F. Kocks, A.S. Argon, M.F. Ashby, Thermodynamics and kinetics of slip, Pergamon Press, 1975.

[25] M.F. Ashby, The deformation of plastically non-homogeneous materials, Philos. Mag. Philos. Mag. 21 (1970) 399–424.

[26] G.I. Taylor, The Mechanism of Plastic Deformation of Crystals. Part1. Theoretical, Proceeding R. Soc. 538 (1934) 362–387.

[27] A. Arsenlis, D.M. Parks, Modeling the evolution of crystallographic dislocation density in crystal plasticity, J. Mech. Phys. Solids. 50 (2002) 1979–2009.

[28] A. Arsenlis, D.M. Parks, R. Becker, V. V Bulatov, On the evolution of crystallographic dislocation density in non-homogeneously deforming crystals, J. Mech. Phys. Solids. 52 (2004) 1213–1246. https://doi.org/10.1016/j.jmps.2003.12.007.

[29] A. Arsenlis, Modeling Dislocation Density Evolution in Continuum Crystal Plasticity, PhD thesis, Massachusetts Institute of Technology, 2001.

[30] M.E. Gurtin, A gradient theory of single-crystal viscoplasticity that accounts for geometrically necessary dislocations, J. Mech. Phys. Solids. 50 (2002) 5–32.

[31] F.P.E. Dunne, D. Rugg, A. Walker, Lengthscale-dependent, elastically anisotropic, physically-based hcp crystal plasticity: Application to cold-dwell fatigue in Ti alloys, Int. J. Plast. 23 (2007) 1061–1083. https://doi.org/10.1016/j.ijplas.2006.10.013.

[32] L.P. Evers, W. Brekelmans, M.G.D. Geers, Scale dependent crystal plasticity framework with dislocation density and grain boundary effects, Int. J. Solids Struct. 41 (2004) 5209–5230. https://doi.org/10.1016/j.ijsolstr.2004.04.021.

[33] C.F. Niordson, J.W. Hutchinson, On lower order strain gradient plasticity theories, Eur. J. Mech. A/Solids. 22 (2003) 771–778. https://doi.org/10.1016/S0997-7538(03)00069-X.

[34] J.L. Bassani, Incompatibility and a simple gradient theory of plasticity, J. Mech. Phys. Solids. 49 (2001) 1983–1996. https://doi.org/10.1016/S0022-5096(01)00037-0.

[35] E.P. Busso, F.T. Meissonnier, N.P.O. Dowd, Gradient-dependent deformation of two-phase single crystals, J. Mech. Phys. Solids. 48 (2000) 2333–2361.

[36] A. Arsenlis, D.M. parks, Crystallographic aspects of geometrically nesesary and statistically stored dislocation density, Acta Mater. 47 (1999) 1597–1611.

[37] R. De Borst, H. -B Mühlhaus, Gradient-dependent plasticity: Formulation and algorithmic aspects, Int. J. Numer. Methods Eng. 35 (1992) 521–539. https://doi.org/10.1002/nme.1620350307.

[38] H. Gao, Y. Huang, W.D. Nix, J.W. Hutchinson, Mechanism-based strain gradient plasticity - I. Theory, J. Mech. Phys. Solids. 47 (1999) 1239–1263. https://doi.org/10.1016/S0022-5096(98)00103-3.

[39] G. Yun, K.C. Hwang, Y. Huang, P.D. Wu, A reformulation of mechanism-based strain gradient plasticity, Philos. Mag. 85 (2005) 4011–4029. https://doi.org/10.1080/14786430500363338.

[40] M.E. Gurtin, On the plasticity of single crystals: Free energy, microforces, plastic-strain gradients, J. Mech. Phys. Solids. 48 (2000) 989–1036. https://doi.org/10.1016/S0022-5096(99)00059-9.

[41] J.F. Nye, Some geometrical relations in dislocated crystals, Acta Metall. 1 (1953) 153–162.

[42] S. Das, F. Hofmann, E. Tarleton, Consistent determination of geometrically necessary dislocation density from simulations and experiments, Int. J. Plast. 109 (2018) 18–42. https://doi.org/10.1016/j.ijplas.2018.05.001.

[43] H. Dai, Geometrically-necessary dislocation density in continuum plasticity theory, FEM Implement. Appl. (1997).

[44] A. Ma, F. Roters, D. Raabe, A dislocation density based constitutive model for crystal plasticity FEM including geometrically necessary dislocations, Acta Mater. 54 (2006) 2169–2179. https://doi.org/10.1016/j.actamat.2006.01.005.

[45] S. Waheed, Z. Zheng, D.S. Balint, F.P.E. Dunne, Microstructural effects on strain rate and dwell sensitivity in dual-phase titanium alloys, Acta Mater. 162 (2019) 136–148. https://doi.org/10.1016/j.actamat.2018.09.035.

[46] B. Chen, K. Jansenss, F.P.E. Dunne, Role of geometrically necessary dislocation density in multiaxial and non-proportional fatigue crack nucleation, Int. J. Fatigue. 135 (2020) 105517. https://doi.org/10.1016/j.ijfatigue.2020.105517.

[47] D. Wilson, F.P.E. Dunne, A mechanistic modelling methodology for microstructure-sensitive fatigue crack growth, J. Mech. Phys. Solids. 124 (2019) 827–848. https://doi.org/10.1016/j.jmps.2018.11.023.

[48] F.P.E. Dunne, R. Kiwanuka, A.J. Wilkinson, Crystal plasticity analysis of micro-deformation , lattice rotation and geometrically necessary dislocation density, Proc. R. Soc. A Math. Phys. Eng. Sci. (2012).

https://doi.org/10.1098/rspa.2012.0050.

[49] J. Cheng, S. Ghosh, A crystal plasticity FE model for deformation with twin nucleation in magnesium alloys, Int. J. Plast. 67 (2015) 148–170. https://doi.org/10.1016/j.ijplas.2014.10.005.

[50] M.T. Hutchings, P.J. Withers, T.M. Holden, T. Lorentzen, Introduction to the Characterization of Residual Stress by Neutron Diffraction, 2005.

[51] O. Engler, V. Randle, Introduction to TEXTURE ANALYSIS, CRC press, Taylor and Francis Group, 2010.

[52] W.H. Bragg, W.L. Bragg, The reflection of X-rays by crystals, in: Proceeding R. Soc. A, London, 1913: pp. 428–438.

[53] F. Xu, R.A. Holt, M.R. Daymond, R.B. Rogge, E.C. Oliver, Development of internal strains in textured Zircaloy-2 during uni-axial deformation, 488 (2008) 172–185. https://doi.org/10.1016/j.msea.2007.11.018.

[54] A.J. Wilkinson, G. Meaden, D.J. Dingley, High-resolution elastic strain measurement from electron backscatter diffraction patterns: New levels of sensitivity, Ultramicroscopy. 106 (2006) 307–313. https://doi.org/10.1016/j.ultramic.2005.10.001.

[55] A.J. Wilkinson, Measurement of elastic strains and small lattice rotations using electron back scatter diffraction, Ultramicroscopy. 62 (1996) 237–247.

[56] K. Troost, P. van der Sluis, D. Gravesteijn, Microscale elastic-strain determination by backscatter Kikuchi diffraction in the scanning electron microscope, Appl. Phys. Lett. 62 (1993) 1110–1112.

[57] T.B. Britton, a. J. Wilkinson, High resolution electron backscatter diffraction measurements of elastic strain variations in the presence of larger lattice rotations, Ultramicroscopy. 114 (2012) 82–95. https://doi.org/10.1016/j.ultramic.2012.01.004.

[58] Tenckhoff E. 2005 Review of deformation mechanisms, texture, and mechanical anisotropy in zirconium and zirconium base alloys. Zirconium in the Nuclear Industry: 14th Int. Symp. 1467, 25–50.

[59] R.B. Adamson, C.E. Coleman, M. Griffiths, Irradiation creep and growth of

zirconium alloys: A critical review, J. Nucl. Mater. 521 (2019) 167–244. https://doi.org/10.1016/j.jnucmat.2019.04.021.

[60] A. Rogerson, Irradiation growth in zirconium and its alloys, J. Nucl. Mater. 159 (1988) 43–61. https://doi.org/10.1016/0022-3115(88)90084-0.

[61] V. Fidleris, The irradiation creep and growth phenomena, J. Nucl. Mater. 159 (1988) 22–42. https://doi.org/10.1016/0022-3115(88)90083-9.

[62] R.A. Murgatroyd, A. Rogerson, An assessment of the influence of microstructure and test conditions on the irradiation growth phenomenon in zirconium alloys, J. Nucl. Mater. 90 (1980) 240–248. https://doi.org/10.1016/0022-3115(80)90261-5.

[63] C.D. Cann, D. Faulkner, K. Nuttall, R.C. Styles, A.J. Shillinglaw, C.K. Chow, A.J. Rogowski, Irradiation Growth in Zirconium and Zirconium Alloys Irradiated in the Dounreay Fast Reactor Croissance Par Irradiation Du Zirconium, 1986.

[64] R.A. Holt, Mechanisms of irradiation growth of alpha-zirconium alloys, J. Nucl. Mater. 159 (1988) 310–338. https://doi.org/10.1016/0022-3115(88)90099-2.

[65] R. Holt, A. Causey, N. Christodoulou, M. Griffiths, E. Ho, C. Woo, Non-Linear Irradiation Growth of Cold-Worked Zircaloy-2, Zircon. Nucl. Ind. Elev. Int. Symp. (1997) 623–637. https://doi.org/10.1520/STP16193S.

[66] C.N. Tomé, N. Christodoulou, P.A. Turner, M.A. Miller, C.H. Woo, J. Root, T.M. Holden, Role of internal stresses in the transient of irradiation growth of Zircaloy-2, J. Nucl. Mater. 227 (1996) 237–250. https://doi.org/10.1016/0022-3115(95)00140-9.

[67] C.H. Woo, Modeling irradiation growth of zirconium and its alloys, Radiat. Eff. Defects Solids. 144 (1998) 145–169. https://doi.org/10.1080/10420159808229674.

[68] A. V Barashev, S.I. Golubov, R.E. Stoller, Theoretical investigation of microstructure evolution and deformation of zirconium under neutron irradiation, J. Nucl. Mater. 461 (2015) 85–94. https://doi.org/10.1016/j.jnucmat.2015.02.001.

[69] S.I. Golubov, A. V. Barashev, R.E. Stoller, On the origin of radiation growth of hcp crystal, ORNL/TM-2011/473. (2011).

[70] R.E. Stoller, Primary Radiation Damage Formation, 1st ed., Elsevier Inc., 2012. https://doi.org/10.1016/B978-0-08-056033-5.00027-6.

[71]   A. Patra, C.N. Tomé, S.I. Golubov, Crystal plasticity modeling of irradiation growth in Zircaloy-2, Philos. Mag. 97 (2017) 2018–2051. https://doi.org/10.1080/14786435.2017.1324648.

[72]   L. Balogh, D.W. Brown, P. Mosbrucker, F. Long, M.R. Daymond, Dislocation structure evolution induced by irradiation and plastic deformation in the Zr-2.5Nb nuclear structural material determined by neutron diffraction line profile analysis, Acta Mater. 60 (2012) 5567–5577. https://doi.org/10.1016/j.actamat.2012.06.062.

[73]   L. Cogez, W. Li, O.T. Woo, MECHANICAL PROPERTIES OF ZIRCALOY-2 NEUTRON IRRADIATED TO HIGH FLUENCE, CNL Nucl. Rev. 6 (2017) 221–230.

[74]   R. Thomas, D. Lunt, M.D. Atkinson, J. Quinta, M. Preuss, F. Barton, J.O. Hanlon, P. Frankel, R. Plc, Characterisation of irradiation enhanced strain localisation in a zirconium alloy, Materialia. 5 (2019) 100248. https://doi.org/10.1016/j.mtla.2019.100248.

[75]   Q. Wang, F. Long, Z. Wang, N. Guo, M.R. Daymond, Orientation dependent evolution of plasticity of irradiated Zr-2.5Nb pressure tube alloy studied by nanoindentation and finite element modeling, J. Nucl. Mater. 512 (2018) 371–384. https://doi.org/10.1016/j.jnucmat.2018.10.033.

[76]   Q. Wang, C. Cochrane, T. Skippon, Z. Wang, H. Abdolvand, M.R. Daymond, Orientation-dependent irradiation hardening in pure Zr studied by nanoindentation, electron microscopies, and crystal plasticity finite element modeling, Int. J. Plast. 124 (2020) 133–154. https://doi.org/10.1016/j.ijplas.2019.08.007.

[77]   F. Long, L. Balogh, D.W. Brown, P. Mosbrucker, T. Skippon, C.D. Judge, M.R. Daymond, Effect of neutron irradiation on deformation mechanisms operating during tensile testing of Zr e 2 . 5Nb, Acta Mater. 102 (2016) 352–363. https://doi.org/10.1016/j.actamat.2015.09.032.

[78]   N.R. Barton, A. Arsenlis, J. Marian, A polycrystal plasticity model of strain localization in irradiated iron, J. Mech. Phys. Solids. 61 (2013) 341–351. https://doi.org/10.1016/j.jmps.2012.10.009.

[79]   A. Patra, D.L. McDowell, Continuum modeling of localized deformation in irradiated bcc materials, J. Nucl. Mater. 432 (2013) 414–427. https://doi.org/10.1016/j.jnucmat.2012.08.021.

[80]   T.O. Erinosho, F.P.E. Dunne, Strain localization and failure in irradiated zircaloy with crystal plasticity, Int. J. Plast. 71 (2015) 170–194. https://doi.org/10.1016/j.ijplas.2015.05.008.

[81]   F. Onimus, M. Bono, B. Verhaeghe, A. Soniak, P. Pilvin, Polycrystalline modeling of the behavior of neutron-irradiated recrystallized zirconium alloys during strain path change tests, Int. J. Plast. 134 (2020) 102835. https://doi.org/10.1016/j.ijplas.2020.102835.

[82]   J. Hure, S. El Shawish, L. Cizelj, B. Tanguy, Intergranular stress distributions in polycrystalline aggregates of irradiated stainless steel, J. Nucl. Mater. 476 (2016) 231–242. https://doi.org/10.1016/j.jnucmat.2016.04.017.

[83]   X. Xiao, D. Terentyev, L. Yu, A. Bakaev, Z. Jin, H. Duan, Investigation of the thermo-mechanical behavior of neutron-irradiated Fe-Cr alloys by self-consistent plasticity theory, J. Nucl. Mater. 477 (2016) 123–133. https://doi.org/10.1016/j.jnucmat.2016.05.012.

[84]   P. Chakraborty, S. Bulent Biner, Crystal plasticity modeling of irradiation effects on flow stress in pure-iron and iron-copper alloys, Mech. Mater. 101 (2016) 71–80. https://doi.org/10.1016/j.mechmat.2016.07.013.

[85]   F. Onimus, J. Béchade, A polycrystalline modeling of the mechanical behavior of neutron irradiated zirconium alloys, J. Nucl. Mater. 384 (2009) 163–174. https://doi.org/10.1016/j.jnucmat.2008.11.006.

Chapter 3

3 A non-local crystal plasticity constitutive model for hexagonal close-packed polycrystals

A strain gradient crystal plasticity finite element model is developed to study the evolution of internal and localized elastic strains in hexagonal close-packed polycrystals. The results of the model are firstly compared to the previously published data for a series of in-situ neutron diffraction experiments conducted on α-zirconium specimens. The development of internal lattice strains is studied first without considering the possible effects of grain morphologies and locations. This is followed by importing the "as-measured" grain maps into the model, and investigating the development of localized lattice rotation fields, geometrically necessary dislocation densities, and statistically stored dislocation densities in the vicinity of twins. The numerical results are compared to those measured for a deformed α-zirconium specimen using high angular resolution electron back scatter diffraction technique. To understand the benefits of using non-local formulation, numerical results are further compared to those from a conventional crystal plasticity model. It is shown that while the calculated lattice strains and lattice rotations from both models are in agreement with the measured ones, the non-local model provides a better estimation of localized stresses in the regions with a sharp strain gradient. This difference is more pronounced in the vicinity of twins, where the calculated stresses and geometrically necessary dislocation densities by the non-local model are in better agreement with the measurements.

3.1 Introduction

Understanding the deformation mechanism of hexagonal closed-packed (HCP) polycrystals has been in the center of many studies for decades [1–5]. These polycrystals

are being used in various industrial sectors. For example, zirconium and its alloys are used for manufacturing the core components of nuclear reactors due to their low neutron absorption cross section and good corrosion resistance. Magnesium and titanium alloys are used in automotive and aerospace industries due to their low density and good mechanical properties. During fabrication or in service, these materials may undergo macroscopic or localized microscopic plastic deformation. Such localized deformation zones can become susceptible sites for crack nucleation or even accelerated corrosion [6–9]. This chapter focuses on the development of a strain-gradient, also known as non-local, crystal plasticity finite element (CPFE) model to study the distribution of localized stress or dislocation hotspots that drives accelerated degradation mechanisms while replicating the macroscopic deformation behaviour of HCP polycrystals.

Various numerical approaches have been used to investigate the micromechanics of plastic deformation. For example, dislocation dynamics (DD) simulations were used to identify the coefficients of latent hardening in pure magnesium [10]. Such modeling scheme helps understand how the interactions among dislocations of different slip systems affect the macroscopic hardening observed in magnesium alloys [11]. Further, Tummala et al. used DD modeling to study the stress fields around hydrides in zirconium [12]. It is important to understand how the localized stress fields around zirconium hydrides evolve since hydrogen embrittlement significantly affects the facture toughness of the zirconium alloys used in nuclear industry. Although DDD models take the interaction between individual dislocations into account, they are numerically costly and do not represent the "real" time scale over which a given phenomenon occurs. As a meso-scale modeling scheme, crystal plasticity is used to study heterogeneous deformation of individual or clusters of grains in "real time" by taking into account the effects of plastic slip that occurs on active slip systems [13–15]. Crystal plasticity has been implemented in different frameworks, e.g., self-consistent [16], fast Fourier transform (FFT) [17,18], and

finite element (FE) [19,20]. In the self-consistent framework, each grain interacts with a homogenous medium that represents the average properties of the aggregate except for the grain that is investigated. Although it is naturally fast, it is not possible to study the "true" interaction among neighbouring grains in the self-consistent framework. In the FFT or FE frameworks, however, such interactions can be investigated and recently, there has been promising advances in the field [21–24].

It has been shown that the interaction among the neighboring grains can have significant effects on the evolution of stress within individual grains of HCP polycrystals [25]. Such interactions can lead to the development of localized stress or dislocation fields that control the nucleation of cracks in materials [26]. Depending on the crystal orientation, slip or twinning are generally active in such localized stress fields. For slip to occur, dislocations should overcome both short-range and long-range obstacles. The primary short-range obstacles are generally assumed to be the other dislocations that intersect the slip plane and can potentially impede the movement of dislocations on the same plane. The long-range obstacles, on the other hand, may include the elastic stress fields due to grain boundaries or far field dislocations and defects. While the short-range obstacles can mainly be overcome by thermal activation, the long-range obstacles are generally independent from temperature and can be overcome by increasing the resolved shear stress (RSS) that acts on the slip system [27]. Many studies have attempted to incorporate the effects of both short- and long-range obstacles in material hardening models. For example, Lu et al. (2019) assumed that the dislocation movement is a function of the resistance induced by both short- and long-range obstacles. It was assumed that the threshold for activating dislocation glide depends on the long-range obstacles which in turn depends on the evolving dislocation density. The resistance due to short-range obstacles was assumed to originate from Peierls barrier, solid solution atoms, or other point defects in the material. Evers et al. assumed that the resistance induced by the long-

range obstacles is a function of the spatial gradient of geometrically necessary dislocations (GND) densities, while that of short-range obstacles was assumed to be dependent on both total GND and statistically stored dislocation (SSD) densities [23]. Therefore, it was assumed that SSDs do not have any long-range effects, while the evolution of both SSDs and GNDs during crystallographic slip equally increase the short-range interactions [28,29]. In the conventional form of crystal plasticity, no differentiation is made between the two types of obstacles. That is, the critical resolved shear stress (CRSS) required for dislocation movement solely depends on the state of deformation in the current calculation point. However, in the non-local crystal plasticity framework, dislocation densities are calculated based on the gradients of the plastic strain; such gradients depend on the deformation of the neighbouring regions and hence, both short- and long-range effects can be introduced [30–35].

There are two forms of strain gradient plasticity theories, i.e., the lower-order and higher-order theories [36]. In the lower-order form [37–39], the effects of strain gradients are only included in the materials hardening laws, with no subsequent adjustment made to the force-equilibrium equations or boundary conditions. For example, in the crystal plasticity framework, this is mainly done by introducing GND densities to materials hardening equations and correlating GNDs with the gradient of the plastic strain. While it is the simpler form between the two, the drawback of this approach is that it may result in unrealistic higher strain gradients and formation of unusual localized deformation fields [36]. In the higher-order form [40–43], both materials hardening law as well as force-equilibrium equations are modified by adding an extra term that represents localized micro-scale stresses. The consideration of micro-scale stresses results in the modification of virtual work equations which in return results in an extra term proportional to the second order gradient of the plastic strain. In order to solve these differential equations, additional boundary conditions are generally required.

Diffraction based experimental techniques are mainly used for measuring internal or localized stress fields as well as the density of dislocations. While the measurement of SSDs is not straightforward, various diffraction techniques are used for measuring GNDs. For example, micro X-ray diffraction is used for measuring the density of dislocation in the vicinity of slip bands or for determining slip activity in HCP polycrystals [44,45]. This method provides a three-dimensional view of the GNDs as well as stress fields, but for a few grains. With high angular resolution electron back scatter diffraction (HR-EBSD) technique it is, however, possible to measure stresses and GND densities in many grains, yet close to the sample surface. In this technique, the Kikuchi diffraction patterns measured within a grain are cross correlated with respect to a pattern collected at a reference point within the same grain. The reference point is normally chosen to be "far" from grain boundaries where the variation of stress and orientation is assumed to be minimum. The displacement gradient can subsequently be calculated and used to extract the "relative" elastic strain and lattice rotation, and by assuming that the stress normal to surface is zero, it is possible to calculate the "relative" stress tensor [46–48]. Since the "relative" elastic lattice rotations are known, it is possible to calculate GND densities using Nye tensor [49]. This method has been successfully used for measuring stresses and GND densities at the vicinity of slip bands and twins in HCP polycrystals [50–52]. For measuring internal strains, as oppose to surface strains, neutron or X-ray diffraction can be used [53–55]. Lattice strains are the elastic strains in the direction of the scattering vector and in the family of grains that can diffract the incident X-ray or neutron beam. The deflections observed in lattice strains correspond to activation of various slip or twinning modes of deformation. This unique property of lattice strains can be used to study deformation mechanism of polycrystals.

In this chapter, a non-local CPFE model is developed to study deformation mechanisms of HCP polycrystals. Results from a calibrated conventional CPFE model are used to

firstly calibrate the single crystal properties of the non-local model. The non-local model is subsequently validated in two steps; in the first step, the development of internal lattice strains in Zircaloy-2 is simulated and compared to those measured using the neutron diffraction technique. In the second step, the distribution of localized elastic lattice rotation, dislocation density, and stress for individual zirconium crystals from the model are compared to those measured using HR-EBSD. Attention is given to deformation fields measured and simulated in the vicinity of twins. In addition, results from the non-local model are compared to those from the conventional method. The aim of this chapter is to understand the benefits of using non-local models over conventional CPFE models and highlight their differences.

3.2   Experiments

The numerical results are compared to the previously published data measured by the authors using neutron diffraction and HR-EBSD methods. Details of each experiment are provided in [56] and [57], here just a brief description is provided. For the neutron diffraction experiment, samples were cut from a hot rolled Zircaloy-2 plate with the texture shown in Fig. 3.1a. Since most of the crystals c-axis are oriented towards the normal direction (ND), tension along rolling direction (RD) or compression along ND will have minimum effects on the activation of tensile twinning and will cause plastic deformation mainly by slip on prism and basal systems. In this experiment, samples were deformed in-situ along the ND and RD with lattice strains measured along all three principal directions, i.e. ND, RD, and transverse direction (TD). The first step of model validation was done by ignoring the effects of deformation twinning and comparing the calculated lattice strains for compression along ND and tension along RD to those measured experimentally. Although the average texture and lattice strains were measured

in the neutron diffraction experiment, it was not possible to determine grain morphologies and locations with the set-up used.
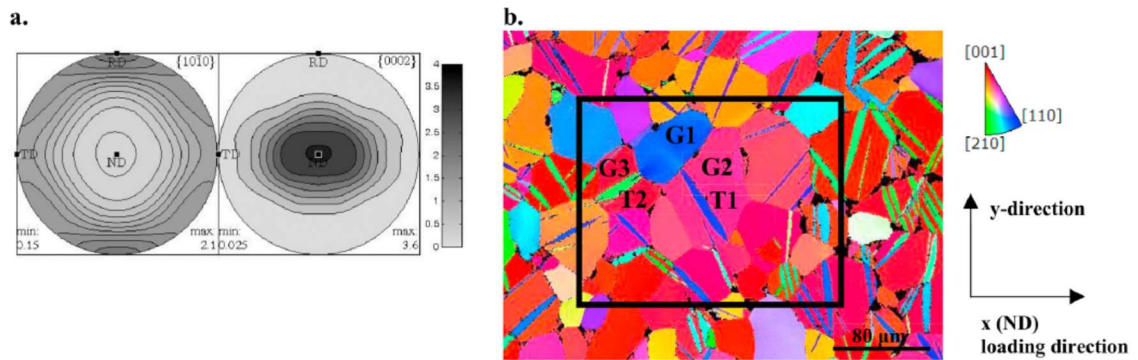
Figure 3.1 (a) The initial texture of the Zircaloy-2 specimen used in the neutron diffraction experiment. The three principle directions are the normal direction (ND), rolling direction (RD) and transverse direction (TD). (b) The measured EBSD map is color coded with respect to the inverse pole figure- ND.

Understanding the effects of the grain-grain interactions on the formation of localized deformation fields is the main benefit of using a non-local model. Such localized deformation fields may form in the vicinity of the twins, particularly close to their tips, which may trigger nucleation of a crack. Formation of stress hotspots in the vicinity of twins in HCP and face-centered cubic (FCC) materials has been studied by [58–60]. Therefore, in the second step of the current study, the "real" grain shapes measured for a deformed Zircoaloy-2 sample was imported into the CPFE model to simulate the formation of localized deformation fields. In contrast to the neutron diffraction experiment where only the "average" strain from many diffracting grains are measured, in this step, the "localized" values within individual grains are measured. The experiment was done by applying a uniaxial tensile load along the ND and measuring the "relative" elastic strain, lattice rotation, and stress fields using HR-EBSD technique. In addition, the

distribution of GNDs were measured and compared with the modeling results. Since the c-axis of most of the grains is oriented towards the loading direction, deformation twinning is activated. For Zircaloy-2, $\{10\bar{1}2\}\langle10\bar{1}1\rangle$ tensile twinning is the dominant twin system at room temperature. The measured EBSD map for the deformed sample is shown in Fig. 3.1b. The HR-EBSD measurement is conducted in the region shown with a black rectangle.

In both experiments, samples were deformed using strain rate of $\dot{\varepsilon} = 5 \times 10^{-5} s^{-1}$. For neutron diffraction experiments, samples were deformed up to 12% applied strain whereas for the HR-EBSD experiment, the sample was deformed to 2.7% tensile strain, after which it was unloaded for ex-situ measurement. Both samples were initially annealed at 650 °C and cooled down to room temperature to conduct the experiments. To investigate the localized stress and dislocation fields induced by twinning, two of the twins located in the middle of the EBSD map, T1 and T2 as shown in Fig. 3.1b, are modeled and studied in detail.

3.3   Modeling

The constitutive equations used for both conventional and non-local crystal plasticity models in the finite element framework are described in this section. These equations are implemented into a user material (UMAT) subroutine originally developed by Abdolvand and Wilkinson [57]. The equations that govern deformation by slip are firstly described which are followed by the assumptions made to simulate deformation twinning.

3.3.1   Crystal plasticity constitutive equations

In the absence of twinning, the total deformation gradient ($\boldsymbol{F}$) can be decomposed to the elastic ($\boldsymbol{F^e}$) and plastic ($\boldsymbol{F^p}$) parts following:

$$F = F^e F^p \qquad\qquad (3\text{-}1)$$

The total velocity gradient tensor (L) in the current configuration can be divided into elastic (L^e) and plastic (L^p) parts as:

$$L = \dot{F} F^{-1} = \dot{F}^e F^{e-1} + F^e \dot{F}^p F^{p-1} F^{e-1} = L^e + L^p \qquad\qquad (3\text{-}2)$$

The total velocity gradient tensor can be divided into symmetric part, i.e. deformation rate tensors (D^e, D^p), and asymmetric part, i.e. spin tensors (Ω^e, Ω^p). The time integration of deformation rate tensor and spin tensor, respectively provides the increments of the strain and rotation tensors. During crystallographic slip, dislocations move on a particular plane in a particular direction. The plastic part of the velocity gradient can be calculated from the summation of crystallographic slips over all active slip systems [61]:

$$L^p = D^p + \Omega^p = \sum_{\alpha=1}^{N} \dot{\gamma}^\alpha \vec{m}^\alpha \otimes \vec{n}^\alpha \qquad\qquad (3\text{-}3)$$

where $\vec{m}^\alpha$, $\vec{n}^\alpha$ and $\dot{\gamma}^\alpha$ represent the slip direction, the slip plane normal and the shear rate on the αth slip system for the N number of slip systems, respectively. $\vec{m}^\alpha \otimes \vec{n}^\alpha$ is the dyadic product of the slip plane direction and the slip plane normal, known as the Schmid tensor of the slip system α. The plastic parts of the deformation rate and spin tensors can be calculated using the following equations:

$$D^p = \sum_{\alpha=1}^{N} P^\alpha \dot{\gamma}^\alpha$$

$$\Omega^p = \sum_{\alpha=1}^{N} W^\alpha \dot{\gamma}^\alpha$$

(3-4)

where P^α and W^α are the symmetric and asymmetric parts of the Schmid tensor. A rate dependent equation is used to calculate the shear strain rate on the slip system α, based on the resolved shear stress (τ^α) that acts on the same slip system [61]:

$$\dot{\gamma}^\alpha = \dot{\gamma}_0^\alpha \, \text{sign}(\frac{\tau^\alpha}{g^\alpha}) \left|\frac{\tau^\alpha}{g^\alpha}\right|^n$$

(3-5)

where $\dot{\gamma}_0$ is a reference shear strain rate, n represents the sensitivity of the material to a strain-rate and g^α is the CRSS of the slip system α. The difference between conventional and strain-gradient CPFE models is mainly based on the descriptions used for the evolution of g^α [30,62]. The resolved shear stress acting on the slip system α is proportional to Kirchhoff stress (ψ) through the following equation [63]:

$$\tau^\alpha = P^\alpha : \psi$$

(3-6)

The Jaumann rate of the Kirchhoff stress ($\breve{\psi}$) is related to the elastic part of the deformation rate tensor (D^e) as:

$$\breve{\psi} = \mathbb{C} : D^e$$

(3-7)

where $\mathbb{C}$ is the elastic stiffness tensor of the HCP crystal after rotation to the deformed configuration. The elastic modulus of zirconium used in this study is the one determined

by Fisher and Renken [64]: C_{11}=143.5 GPa, C_{33}=164.9 GPa, C_{12}=72.5 GPa, C_{13}=65.4 GPa, and C_{44}=32.1 GPa. The objective rate of Kirchhoff stress, in Eq. (3-7), is defined with respect to an observer attached to the crystal lattice:

$$\breve{\psi} = \dot{\psi} - \Omega^e \psi + \psi \Omega^e \qquad (3\text{-}8)$$

3.3.2   Modeling twins

The developed non-local model is used to study the formation of localized stress and dislocation fields in the vicinity of twin tips. Following the procedure suggested in Kumar et al. [65], individual twins are modeled by manual reorientation of the identified twin domain and applying the characteristic twin shear (γ^{tw}) to the reoriented zone. The twin domains are identified from the measured EBSD map as shown in Fig. 3.1b. It is assumed that formation of twins can be modeled in two independent steps; in the first step, the measured orientation of the twin is assigned to the elements of the twinned zone. In the second step, the twin transformation strain was applied to the same domain over the time interval of T_{TTS} following Eq. (3-9):

$$\dot{\gamma}^{tw} = \frac{0.169}{T_{TTS}}$$

$$(3\text{-}9)$$

$$\boldsymbol{D}^{tw} = \boldsymbol{P}^{tw} \, \dot{\gamma}^{tw}$$

where $\boldsymbol{P}^{tw}$ is the twin Schmid tensor. It was assumed that the transformation strain was applied at the same strain rate as the uniaxial tensile strain rate, hence T_{TTS} in Eq. (3-9) is 3060 seconds. Although this does not capture the real dynamic process of twinning, it helps overcome the possible numerical instabilities resulting from the significant shear applied to the twinned zones. The effects of T_{TTS} on the numerical results are discussed in

section 3.5.2. The calculated $\boldsymbol{D}^{tw}$ is an inelastic deformation rate, which can be added to the elastic and plastic deformation rates to constitute the total deformation rate tensor as:

$$\boldsymbol{D} = \boldsymbol{D}^e + \boldsymbol{D}^p + \boldsymbol{D}^{tw} \tag{3-10}$$

Eqs. (1)-(10) are used in both conventional and non-local CPFE models, however, in this chapter, the difference between the two approaches is in the evolution of CRSS.

3.3.3   The evolution of CRSS: Conventional plasticity

The current strength of each slip system is assumed to follow an extended Voce hardening [62]:

$$g^\alpha = g_0^\alpha + (g_1^\alpha + \theta_1^\alpha\,\Gamma)\left(1 - \exp\left(-\frac{\theta_0^\alpha\,\Gamma}{g_1^\alpha}\right)\right) \tag{3-11}$$

where g^α is the updated CRSS, g_0^α is the initial CRSS and θ_0^α is initial hardening rate. g_1^α and θ_1^α are asymptotic characteristics of hardening and Γ is accumulated shear strain on all slip systems. This equation is proven effective in modeling deformation of zirconium polycrystals [16,56]. Differentiation of Eq. (3-11) with respect to time provides:

$$\frac{dg^\alpha}{dt} = q^{\alpha\beta}\frac{dg^\alpha}{d\Gamma}\frac{d\Gamma}{d\gamma^\beta}\frac{d\gamma^\beta}{dt} \tag{3-12}$$

with summation convention over β. A hardening matrix $q^{\alpha\beta}$ is introduced to consider the effects of self and latent hardening.

The value of g_0^α in Eq. (3-11) depends on grain size through the Hall-Petch equation:

$$g_0^\alpha = g_{*,0}^\alpha + \frac{H^\alpha}{\sqrt{D}} \tag{3-13}$$

Where $g^\alpha_{*,0}$ and H^α are material parameters for slip system α and D is the equivalent grain diameter.

3.3.4　The evolution of CRSS: Strain-gradient plasticity

The evolution of CRSS for each slip system is generally related to the accumulation of dislocations and the interaction among them. The interaction among dislocations of the same and different slip systems lead to self and latent hardening, respectively. Depending on the material and the mechanisms of dislocation interactions, different formulations are suggested for the evolution of CRSS. For example, Zhang et al. assumed that the total dislocation density accumulated on all slip systems determines the development of CRSS [66]. Here, it is assumed that CRSS correlates with the density of GNDs and SSDs following [28,67]:

$$g^\alpha = g^\alpha_0 + \zeta G b^\alpha \sqrt{\sum_{\beta=1}^{N} q^{\alpha\beta} \left(\rho^\beta_{GND} + \rho^\beta_{SSD} \right)}$$

(3-14)

where G is the shear modulus, b^α is the size of the Burgers vector, ζ is a material constant, ρ^α_{GND} is the GND density, ρ^α_{SSD} is the SSD density for the slip system α, and $q^{\alpha\beta}$ is the hardening matrix that represents both self and latent hardening.

The distribution of GNDs is related to the lattice curvature through Nye analysis [68]. ρ^α_{GND} for each slip system can be decomposed into three components, one for screw type dislocation $\rho^\alpha_{GND,s}$ with the dislocation line vector along the slip direction, m^α, and two edge type dislocations, $\rho^\alpha_{GND,en}$ and $\rho^\alpha_{GND,et}$ with dislocation line vectors along the slip normal and $t^\alpha = m^\alpha \times n^\alpha$, respectively. Different approaches are suggested to correlate

the Nye tensor to dislocation density [39,69,70]. Following [34,39], the total GND density on all slip systems is related to $curl(\boldsymbol{F}^{p^T})$ as:

$$\left(curl\left(\boldsymbol{F}^{p^T}\right)\right)^T = \sum_{\alpha=1}^{N} \left(\rho_{GND,s}^{\alpha}\ \vec{b}^{\alpha}\otimes\vec{m}^{\alpha} + \rho_{GND,et}^{\alpha}\ \vec{b}^{\alpha}\otimes\vec{t}^{\alpha} \right.$$
$$\left. + \ \rho_{GND,en}^{\alpha}\ \vec{b}^{\alpha}\otimes\vec{n}^{\alpha}\right)$$

(3-15)

For N number of slip systems, this second order tensorial equation has 9 components with 3×N unknowns. Therefore, for materials with more than three slip systems, Eq. (3-15) will be an under-determined system of linear equations with infinite solutions. One solution can be obtained by minimizing the sum of the squares of GND densities [39]:

$$\{\rho_{GND}^{\alpha}\} = \boldsymbol{A}^T(\boldsymbol{A}\boldsymbol{A}^T)^{-1}\boldsymbol{B}$$

(3-16)

where $\{\rho_{GND}^{\alpha}\}$ is 3N×1 column vector containing edge and screw components of GND for slip system α, $\boldsymbol{B}$ is a 9×1 vector, containing the components of the tensor in the left hand side of Eq. (3-15), and $\boldsymbol{A}$ is a 9×3N matrix containing the basis tensors of right hand side of Eq. (3-15).

The evolution of SSDs are not as much characterized as GNDs; this is due to the lack of experimental data and complexity in determining the density of SSDs. Various formulations are suggested in literature, for example, Zhang et al. assumed that the density of SSDs simply depends on the effective plastic strain [66]. Kocks and Mecking suggested that the evolution of the dislocation density on a given slip system follows a storage step and a subsequent dynamic recovery step [71]. Evers et al. [28] and Cheong et al. [72] assumed that the generation and annihilation rates of SSDs are the same for all

slip systems. Here, it is assumed that the evolution of SSDs for each slip system depends on the density of dislocations for the same slip system:

$$\dot{\rho}_{SSD}^{\alpha} = \frac{|\dot{\gamma}^{\alpha}|}{b^{\alpha}} \left(K^{\alpha}\sqrt{\rho_{SSD}^{\alpha} + \rho_{GND}^{\alpha}} - 2y_{c}^{\alpha}\,\rho_{SSD}^{\alpha} \right) \tag{3-17}$$

where K^{α} is a material constant representing the rate of accumulation of SSDs, and y_{c}^{α} is the critical annihilation length of the dislocations with opposite Burgers vector.

3.3.5   Numerical implementation

The UMAT developed in [57] is updated to include the non-local effects using Eqs. (3-14)-(3-17). As shown in Eq. (3-15) and (3-16), for implementing the non-local effects, it is necessary to calculate the *curl* of $\mathbf{F}^{p}$:

$$(curl\ \mathbf{F}^{p})_{ij} = \epsilon_{irq}\frac{\partial \mathbf{F}_{jq}^{p}}{\partial x_{r}} \tag{3-18}$$

where ϵ_{irq} is the permutation tensor. Following the method described in [20,73,74], the gradient of $\mathbf{F}^{p}$ can be calculated using the element shape function:

$$\frac{\partial \mathbf{F}_{jq}^{p}}{\partial x_{i}} = \sum_{k=1}^{a} \frac{\partial N^{k}}{\partial x_{i}}\,\mathbf{F}_{jq}^{p} \tag{3-19}$$

where N^{k} represents the shape function of the element with "a" nodes and x_{i} represents the global coordinate. Since $\mathbf{F}^{p}$ is calculated at each integration point (IP) within the UMAT, an internal element is introduced inside the original element where the nodes of the internal element coincide with the IPs of the original one [20,73]. Therefore, the shape function N^{k} and nodal coordinates x_{i}^{k} in Eq. (3-19) are for the internal element. The spatial derivative of the shape function can be calculated using the chain rule as:

$$\frac{\partial N^k}{\partial x_i} = \frac{\partial N^k}{\partial \xi_j} \frac{\partial \xi_j}{\partial x_i} \tag{3-20}$$

where ξ_j represents the local element coordinate system. In Eq. (3-20), $\frac{\partial \xi_j}{\partial x_i}$ is the inverse of the *element* Jacobean matrix, which can be calculated using:

$$\frac{\partial x_i}{\partial \xi_j} = \frac{\partial}{\partial \xi_j} \sum_{k=1}^{no.ip} N^k x_i^k = \sum_{k=1}^{no.ip} \frac{\partial N^k}{\partial \xi_j} x_i^k \tag{3-21}$$

For calculating the element Jacobean matrix in Eq. (3-21) and the gradients of $\boldsymbol{F}_{jq}^p$ in Eq. (3-19), it is necessary to use the updated x_i and $\boldsymbol{F}^p$ values for all of the IPs within the same element. Therefore, at the end of each increment, $\boldsymbol{F}^p$ of each IP is stored in a common block variable and is used in the next time increment. Since the calculated GND density in each time increment is based on the $\boldsymbol{F}^p$ of the previous time increment, it is necessary to ensure that the selected time increments are small enough to guarantee convergence for the calculated GND densities. In addition, it can be seen that the lower-order strain gradient theory is used in the current formulation. This is to avoid modifying the force-equilibrium equations and to avoid using second order gradients.

Table 3.1 shows the flowchart of the non-local model. At the beginning of each time increment, Abaqus FE solver provides the total strain increment, rotation increment, deformation gradient, solution dependent state variables (SDVs), and updated coordinate of each IP. $\boldsymbol{F}^p$ of the last time increment is restored from the common block variables and used to evaluate $curl\left(\boldsymbol{F}^{p^T}\right)$ and GND densities using Eq. (3-15)-(3-21). The Newton-Raphson method is used to calculate the increments of shear strain for each slip system ($\Delta\gamma^\alpha$), and update CRSS, the density of SSDs, stress, orientation, and the material

Jacobean matrix. Finally, $\boldsymbol{F}^p$ is updated and stored in a common block variable for the next time increment.

Table 3.1 Flow chart of the Non-local CPFE model

(1) Abaqus FE solver provides total strain increment, rotation increment, and deformation gradient for the time increment *i,* as well as stress ($\boldsymbol{\sigma}^{i-1}$) and state variables ($SDVs^{i-1}$) for time increment i-1.
(2) If manual twining is activated and if the element is in the identified twin domain, reorient and apply twin shear using Eq. (3-9)-(3-10).
(3) Calculate $curl(\boldsymbol{F}^{p,i-1})$ using Eq. (3-18)-(3-21)
(4) Calculate ρ_{GND} using Eq. (3-15)- (3-16)
(5) Using Eqs. (3-3)–(3-8) calculate plastic and elastic strain increments ($\Delta t \boldsymbol{D}^e$, $\Delta t \boldsymbol{D}^p$) using the Newton-Raphson method until convergence of the shear strain increments ($\Delta \gamma^\alpha$)
(6) Update the $SDVs^i$ (τ^α, g^α, γ^α, n^α, m^α), ρ_{SSD}^i, stress ($\boldsymbol{\sigma}^i$) and material Jacobean matrix
(7) Evaluate $\boldsymbol{F}^{p,i}$ from Eqs. (3-1)-(3-2) and store them in a common bock variable for the next time increment

3.4 Results

3.4.1 Determination of the single crystal parameters

Since the performance of the non-local model will be compared against that of the conventional model, the non-local model is calibrated such that it reproduces identical stress-strain curves to those from the conventional model for zirconium single crystals. The single crystal parameters for the conventional model were previously calibrated using a comprehensive data set for lattice strains measured during an in-situ neutron diffraction experiment conducted on Zircaloy-2 [56]. In section 3.4.2, the data from the same experiments are used to validate the non-local model. In the absence of twinning, plastic deformation in zirconium is generally controlled by 18 slip systems, i.e. three prism, three basal and twelve pyramidal <c+a> slip systems. As shown in Table-2, the same strain rate, self, and latent hardening parameters are used in both models. The parameters for the Hall-Petch effects, H^α and $g_{*,0}^\alpha$, are extracted from the CRSS values reported for two independent experiments conducted on the same material but with grain sizes of 20 μm and 50 μm [56,75]. For the non-local model, only the parameters for the

evolution of SSDs are calibrated, i.e., K^α and y_c^α, which are provided in Table 3.3. Further, the shear modulus, G in Eq. (3-14), is assumed to be the average of the C_{44}, C_{55} and C_{66} [76]. The material constant ζ is assumed to be 0.5.

Table 3.2 Strain rate parameters and hardening matrix of Zircaloy-2 single crystals

	n	$\dot{\gamma}_0^\alpha \ (S^{-1})$	q^{ss} (self)	q^{st} (t=prism)	q^{st} (t=basal)	q^{st} (t=pyramidal)
Prism	20	3.5e-4	1	1	1	0
Basal	20	3.5e-4	1	1	1	0
Pyramidal	20	1.0e-4	1	0	0	1

In Fig. 3.2, the results from the non-local model are compared against those from the conventional model. Results are for single crystals Zircaloy-2 with different c-axis misorientations with respect to the loading direction. The grain size of 20 μm was used in all cases to be consistent with the grain size measured for the material used for the neutron diffraction experiment. Single crystals are deformed up to 5% with the strain rate of $5 \times 10^{-5} \ s^{-1}$. The applied boundary conditions are shown in Fig. 3.2a. Uniaxial tensile deformation is applied onto the surface DCGH along the X-direction. The displacement on the ABFE, EFGH, and AEHD surfaces are fixed along X, Y, and Z directions, respectively. The single crystal is discretized to 1000 quadratic brick C3D20R elements, with 10 elements in each direction. The maximum time increment allowed is 5 seconds. This time increment is obtained from a convergence study, ensuring that the calculated GND densities are independent from the size of the time increment.

a.

b.

c.
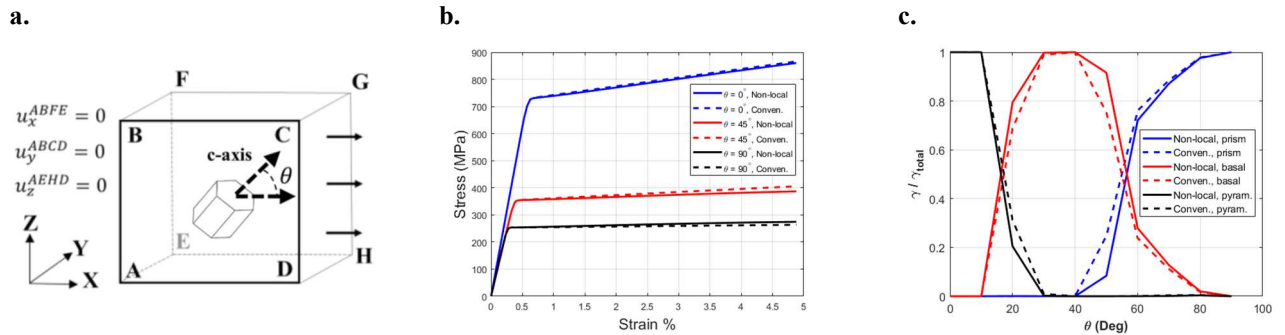
Figure 3.2 Results of the conventional and non-local CPFE models for zirconium single crystals. (a) Applied boundary conditions, (b) average stress-strain curve at three different misorientation angles (θ) of 0º, 45º and 90º and (c) relative activity of basal, prism and pyramidal slip systems. θ is the misorientation between the c-axis of the HCP crystal and the loading direction

In Fig. 3.2b, the stress-strain curves calculated with the non-local model for different crystal orientations are shown and compared against those from the conventional model. The c-axis of the crystal is rotated from 0° to 90° using a 10° increment. To avoid busy figures, only three curves are shown, but the calculated relative activities of each slip system from both models are provided in Fig. 3.2c. Relative activities are calculated by dividing the resolved shear strain (γ^{α}) calculated for each slip set to the total shear strain calculated for all slip systems at the applied strain of 5%. It can be seen that with the fitted single crystal parameters, identical stress-strain curves as well as slip activity are achieved for crystals with different orientations.

Table 3.3 The single crystal parameters used in the conventional and non-local models

	Burgers vector (nm)	Hall-Petch parameters used in both models		Conventional hardening			Non-local hardening	
		H^α ($MPa\ \sqrt{m}$)	$g^\alpha_{*,0}$ (MPa)	g^α_1 (MPa)	θ^α_0 (MPa)	θ^α_1 (MPa)	K^α	y^α_c (nm)
Prism	0.323	0.109	95	1650	50	0	0.05	5
Basal	0.323	0.146	135	1100	250	0	0.05	5
Pyramidal	0.608	0.292	266	270	620	280	0.30	10

3.4.2   Development of internal strains

The performance of both conventional and non-local models for simulating the development of internal elastic lattice strains is investigated in this section. The lattice strains were measured in a set of in-situ neutron diffraction experiments conducted on Zircaloy-2 samples. The initial texture of the samples is shown in Fig. 3.1a and is discretized to 1872 orientations which are used to generate the input FE model shown in Fig. 3.3a. Since in these experiments the positions and shapes of the grains were not measured, grains are assumed to have cubic shapes scattered randomly in the simulated volume. The side length of the cubic model is 200 μm, which leads to an average grain size of 20 μm, in agreement with the one measured prior to the experiment. The model is meshed with 13,824 quadratic brick C3D20R elements. The boundary conditions used are similar to the ones presented in Fig. 3.2a, yet the tensile and compressive loads are along the RD and ND planes, respectively (see Fig. 3.3a). That is, the displacement along ND, TD, and RD are fixed on the ABFE, AEHD, and EFGH surfaces, respectively, while tensile or compressive loads are applied on the ABCD and DCGH surfaces as shown in Fig. 3.3a. In addition, periodic boundary conditions, similar to the ones described in [56],

were also applied the results of which showed minor changes compared to those presented here.

Since the specimens were initially heat treated at 650 °C, this step was included in the CPFE modeling, before applying the mechanical load. The coefficients of thermal expansion for HCP zirconium crystals are $10.1 \times 10^{-6} K^{-1}$ and $5.3 \times 10^{-6} K^{-1}$ along and perpendicular to the crystal c-axis, respectively [77]. The thermal residual strains resulting from this anisotropy affects the elastic lattice strains, but such effects on the crystal orientations are negligible. In Fig. 3.3b and 3.3c, the average stress-strain curves from the non-local and conventional CPFE models are compared to the measured ones for compression along ND and tension along RD. The macroscopic stress-strain curves are measured by a strain gauge attached to the specimens and a remote load cell. The activity of deformation twinning is substantially low in these two directions, but the effects of twinning will be studied in the next section. The agreement between the non-local model and experiment is much better, compared to the conventional model for compression ND. This is in terms of both actual stress-strain curve and the hardening rate. However, for tension along RD, while the average stress from the conventional model deviates from the experiment after 4% applied strain, the prediction of the non-local model improves. More importantly, the average hardening rate or the slope of the stress-strain curve in the plastic zone is better predicted by the non-local model. The average hardening rates from both models are shown by the dashed lines in Fig. 3.3c where a line is fitted using the stress-strain data above 1% strain.
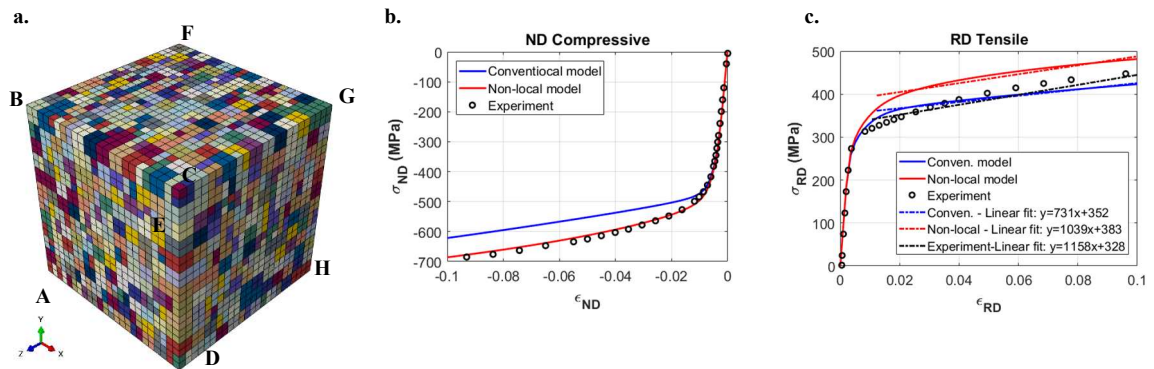
Figure 3.3 a) The CPFE input model used for simulating the neutron diffraction experiment. Random colors are assigned to elements to distinguish grains. Comparison between the calculated stress-strain curves by the conventional CPFE model, the non-local CPFE model, the non-local CPFE model, and the measured ones for (b) compression along ND and (c) tension along RD.

The results of both models for simulating lattice strains are compared against the measured values and are shown in Fig. 3.4. In Fig. 3.4a results for tension along RD and lattice strain measurement along RD, TD, and ND are provided, respectively from top to bottom. For the lattice strains measured along RD, a positive linear slope is observed in both models for all lattice strains. This is expected since the applied load is tensile and all lattice planes will undergo a tensile strain in the loading direction. In the TD and RD directions, however, lattice strains are initially developed with a negative slope until the yield point, where each lattice plane deviates differently from linearity. The first observed deviation is a result of slip activity on the prism planes which is well captured in both models at the applied stress of 150 MPa. For both ND and TD measurements, the (0002) lattice strains deviate from linearity towards more negative strains with two distinct inflections observed at macroscopic stress of 300 MPa and 380 MPa. The former is due to activation of basal while the latter is due to activation of pyramidal slip systems. These inflections are also observed in $(20\bar{2}1)$ and $(11\bar{2}0)$ lattice strains in both ND and TD

measurement directions. It can be seen that both non-local and conventional models replicate the measured trends in lattice strains with some minor differences.

The evolution of lattice strains for compression along ND and measurement along ND, TD, and RD are shown in Fig. 3.4b. It is shown that both $(11\bar{2}0)$ and $(20\bar{2}1)$ lattice strains hardly deviate from linearity in the RD and TD measurements. These trends are well captured by both conventional and non-local models. A distinct deviation form linearity is observed in (0002) lattice strain for the measurement along TD where both models confirm that this is due to activation of slip on prism planes. For the measurement along ND, however, (0002) lattice strain remains linear in agreement with both models. Two inflections are observed in $(11\bar{2}2)$ lattice strains measured along ND, where the first one is related to activation of basal and the second one is related to activation of pyramidal slip systems. The comparison between the simulated and measured lattice strains indicates that both non-local and conventional model are capable of capturing the trends observed with some minor differences between the two models.
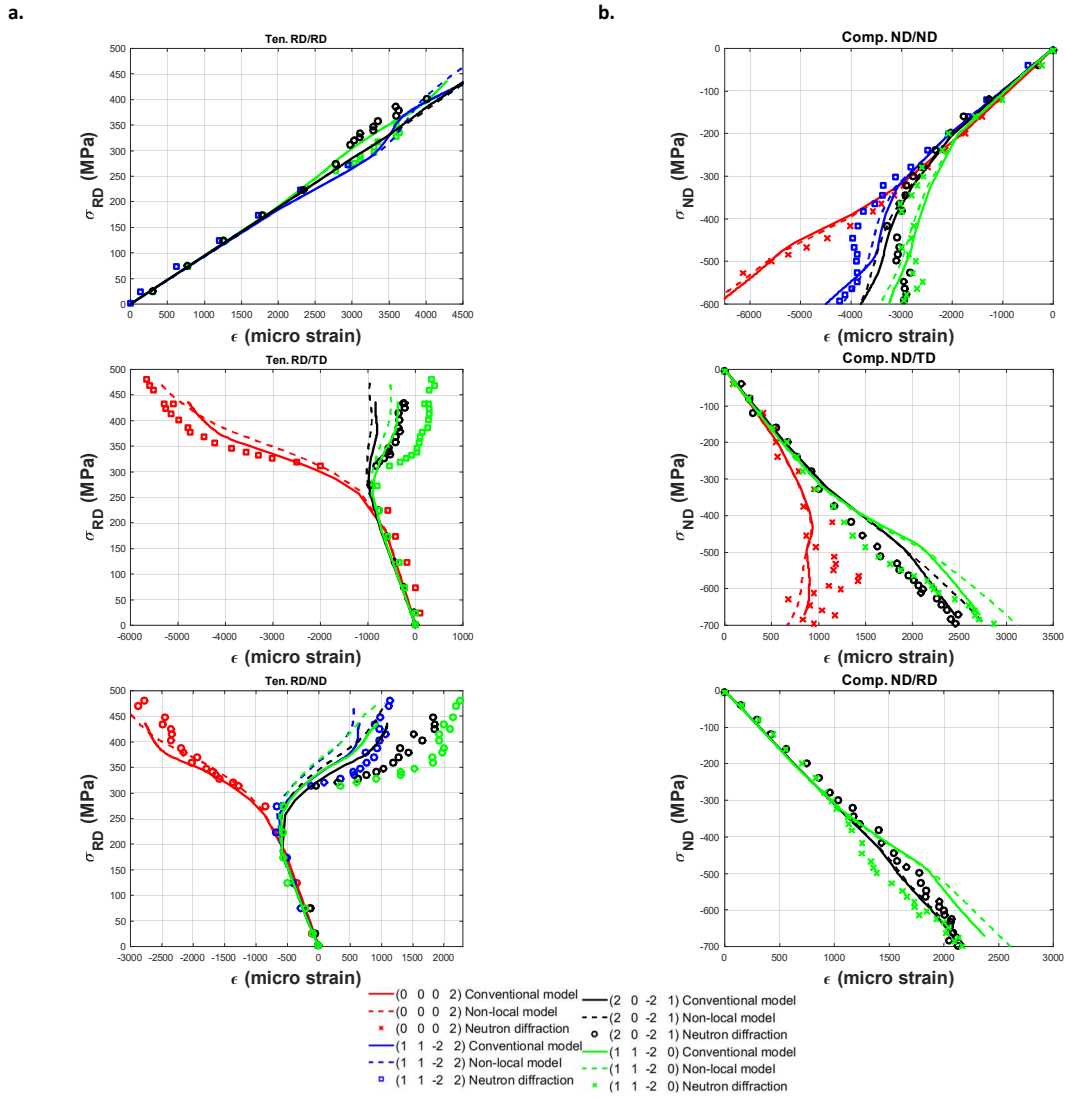
Figure 3.4 The evolution of internal elastic lattice strains: comparison between the results from the conventional model, the non-local model, and neutron diffraction measurements. (a) Tension along RD and measurement along RD (RD/RD), TD(RD/TD), and ND (RD/ND) (b) Compression along ND and measurement along ND (ND/ND), TD(ND/TD), and RD (ND/RD).

3.4.3   CPFE vs HR-EBSD

The imported microstructure to the FE solver is shown in Fig. 3.5a. The model thickness was chosen to be 50 μm which is the measured average grain size of the specimen. The EBSD measured orientations were assigned to the grains of the CPFE model. The boundary conditions used is similar to the other two models presented in the previous sections, that is, $u_x = 0$, $u_y = 0$, and $u_z = 0$ on the ABCD, ADHE, and ABFE surfaces, respectively. Two twins, T1 and T2, located in the middle of the EBSD map with their parent and neighbouring grains, G1, G2, and G3, are studied in detail. These grains are selected because they are far from the edges where it is assumed that the effects of the applied boundary conditions are minimized. The model is discretized using a fine mesh for the studied grains, G1, G2 and G3, and a course mesh for the rest of the grains as shown in Fig. 3.5b. 22,800 quadratic brick C3D20R elements are used with three elements along the thickness. A mesh sensitivity study is performed to ensure that the selected element size in the refined mesh region is converged. As shown in Fig. 3.5c, another input model with a uniform element size for all grains is generated using 50,175 C3D20R elements. The model with uniform mesh is used to investigate the distribution of dislocation densities in all grains, whereas the former model is used to study stress and rotation fields in the vicinity of twins T1 and T2.
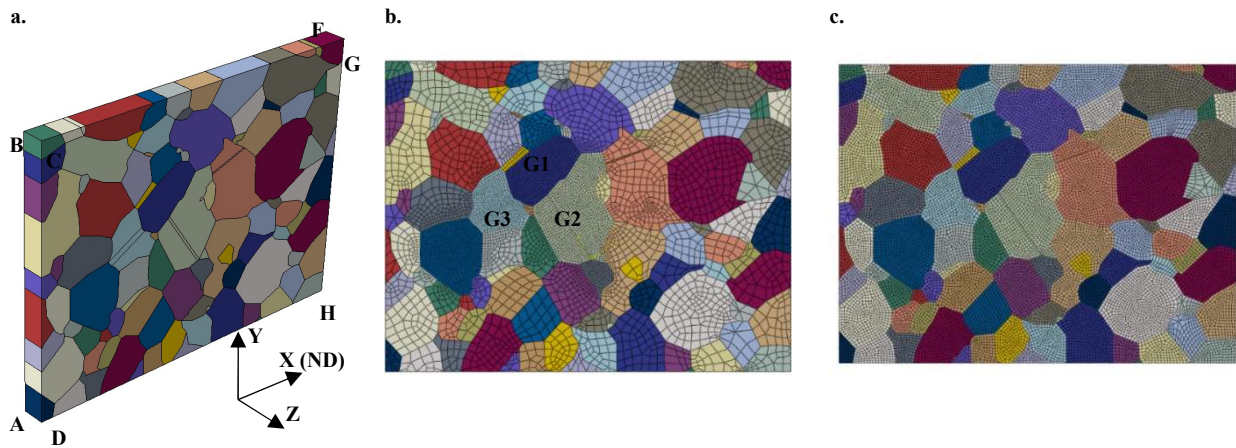
Figure 3.5 (a) The imported microstructure for FE analysis. (b) The model used for studying twins T1 and T2 with refined mesh assigned to grains G1, G2 and G3. (c) The input model used to study dislocation densities in all grains

Following Kumar et al. [65], the formation of twins in the EBSD model is simulated using five distinct steps. In the first step, the model was cooled down from 650 °C to room temperature to account for thermal residual stresses that develop during the heat treatment process [78]. In the second step, the model was strained uniaxially at the strain rate of 5×10^{-5} s^{-1} by applying a velocity onto the EFGH plane (Fig. 3.5a). Once the model was strained to 2.7%, the velocity was set to zero to reorient the twin in step-3 and apply the twin transformation strain in step-4. The reorientation was set to happen over 1 second by assigning the measured orientation from EBSD to the twin domain, while the twin shear transfer was set to happen over 3060 seconds. Since the HR-EBSD measurement was conducted on the sample after unloading, in the last step, step-5, the model was unloaded and allowed to relax.

The results of the non-local model for the distribution of GNDs and SSDs at the end of Step-2 are shown in Fig. 3.6. The initial density of SSDs on each slip system was assumed to be $10^{10} \ m^{-2}$. In contrast to the SSD map, the GND map reveals the

formation of localized deformation zone that resembles formation of slip bands. This is the advantage of using non-local formulation. For example, in grains G6, G7, and G8, as marked in Fig. 3.6a, a distinct band is formed that spans from one side of the grain to another. These bands are associated with plastic shear on the prism planes. Similarly, in grains G3, G9, and G10, the observed bands are related to the activity of basal slip systems. Interestingly, in some of the hard grains where a twin is observed in the EBSD map, e.g. G3, G9 and G10, a high GND density in the vicinity of their grain boundaries is also observed in the numerical results at the end of Step-2. This means that there might be a relationship between GNDs and nucleation of twins.
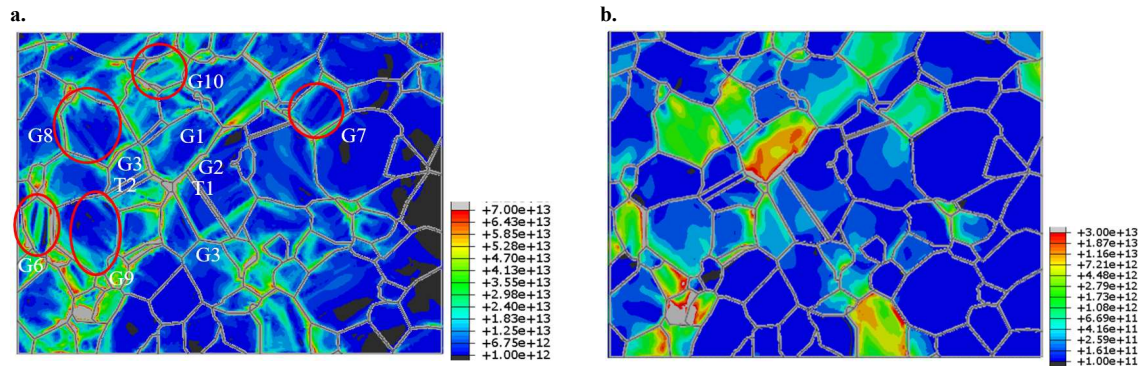
Figure 3.6 Distribution of total (a) GNDs and (b) SSDs at the end of step-2 obtained from the non-local model. The legend is in linear scale with the unit of m^{-2}.

The distribution of the elastic lattice rotations, dislocation densities and stresses for the two twinned grains, G2, G3 and the soft neighbouring grain G1, at different loading steps are provided in the next sections. The results from both non-local and conventional CPFE models are compared against HR-EBSD results.

3.4.3.1   Elastic lattice rotation

The results from the non-local and conventional CPFE models for the grains G1, G2, and G3 are provided in Fig. 3.7 and are compared to those from the HR-EBSD measurement.

Since measurements were done at the surface, only the in-plane component of the lattice rotation (ω_{12}^e) is shown. It can be seen that the difference between the predictions from the two models at Step-2 is negligible. The elastic lattice rotation fields are significantly changed as a result of twin formation (Step-4), especially in the vicinity of the twin tips in the grain G1 (Fig. 3.7a). For example, ω_{12}^e at the vicinity of twin T1 is increased, while it is decreased in front of T2. Although the same trend is observed for both models in Step-5, the non-local model predicts a more positive ω_{12}^e (0.015 radians) at the vicinity of twin T1, compared to the conventional model (0.005 radians). This can be seen in the magnified figures of the elastic rotation field in front of twin T1 in Fig. 3.7a, where the red-colored region extends further into G1 for the non-local model. It should be noted that the limits of the legends are changed for the magnified figures to better demonstrate the differences. In HR-EBSD measurements, a reference point is selected within each grain to measure stresses and elastic lattice rotations with respect to this point. The reference point is normally selected away from grain boundaries where it is assumed that stress and orientation variations are minimum. These reference points are shown with red dots in the Fig. 3.7. Since lattice rotations from HR-EBSD are relative, the calculated lattice rotations at all IPs assigned to a grain are reduced from that calculated at the IP that coincides with the reference point. This is to provide a like-to-like comparison between CPFE results and the HR-EBSD measurement. Generally, both numerical and experimental results indicate that ω_{12}^e is close to zero away from the twin tips. Further, the localized positive ω_{12}^e at the front of the twin T1 is captured by both models, which is in agreement with the HR-EBSD results, however, CPFE underestimate the lattice rotations measured close to twin T2. It can be seen in Fig. 3.7a that the shape and the magnitude of relative ω_{12}^e in the vicinity of T1 from non-local CPFE is in much better agreement with HR-EBSD measurement, compared to conventional CPFE.
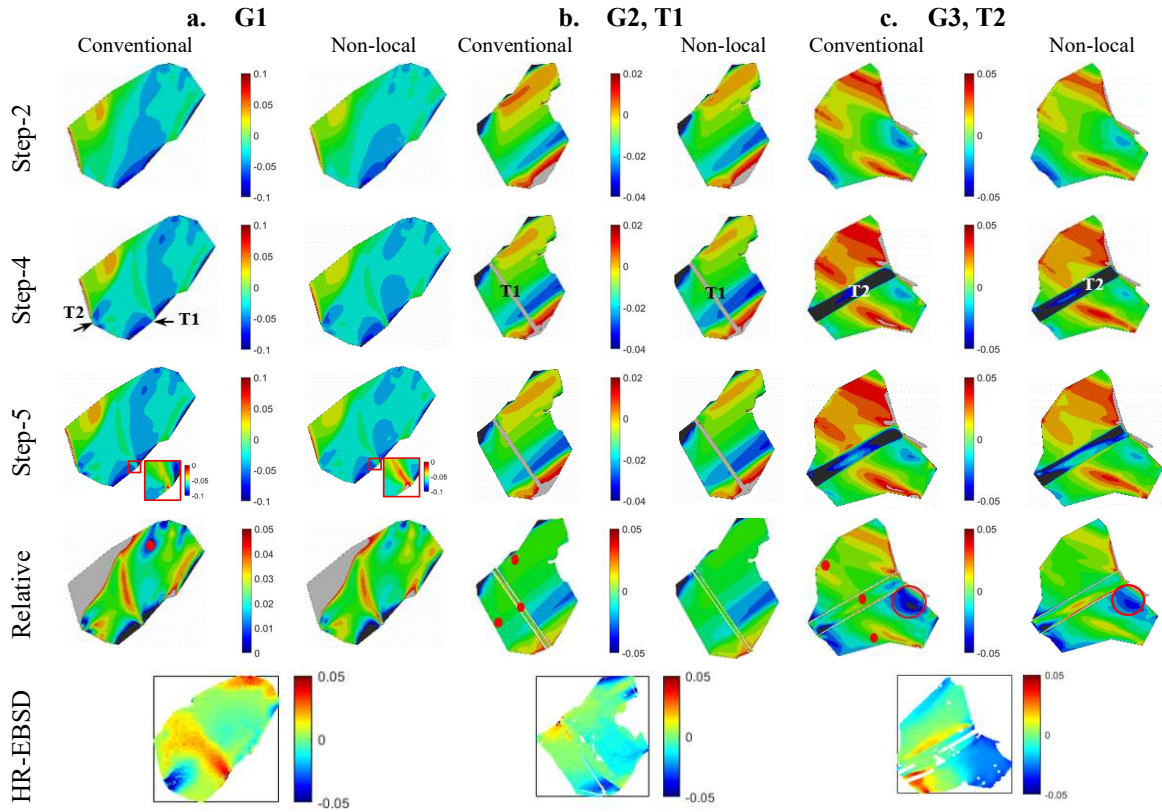
Figure 3.7 The evolution of elastic lattice rotation ω_{12}^e for the grains G1, G2 and G3: comparison between the results from the conventional model, the non-local model, and HR-EBSD measurement. Lattice rotations are given in radians. The numerical results are for Step-2 (after loading), Step-4 (after twin formation) and Step-5 (after unloading).

The in-plane elastic lattice rotations for the grains G2 and G3 are shown in Fig. 3.7b and Fig. 3.7c, respectively. Both conventional and non-local CPFE models show similar distribution for ω_{12}^e. In grain G2, ω_{12}^e within the twinned region is affected by the twin shear transfer step. Similarly, for the grain G3, there is a significant drop in ω_{12}^e due to

twin shear transfer. In agreement with HR-EBSD results, both models predict negative ω^e_{12} close to the right tip of twin T2 inside the parent grain G2. This region is shown with a red circle. However, the positive elastic rotations at the lower left side of the grain is not captured by either of the models.

3.4.3.2   Dislocation density

The distribution of the densities of GNDs and SSDs for the grains G1, G2 and G3 are shown in Fig. 3.8. GNDs are mainly concentrated at the grain boundaries, while SSDs are uniformly distributed within the grains. The densities of both GNDs and SSDs are significantly affected by the twin shear transfer step. In Fig. 3.8a, it is shown that both GND and SSD densities in the vicinity of twin tips increase by the end of Step-4. HR-EBSD results also show localized GND fields at the vicinity of twin tips in the grain G1. In addition, lower GND density is observed within this grain, far from the twin tips and grain boundaries. This region is shown with a red circle in the HR-EBSD and CPFE results.
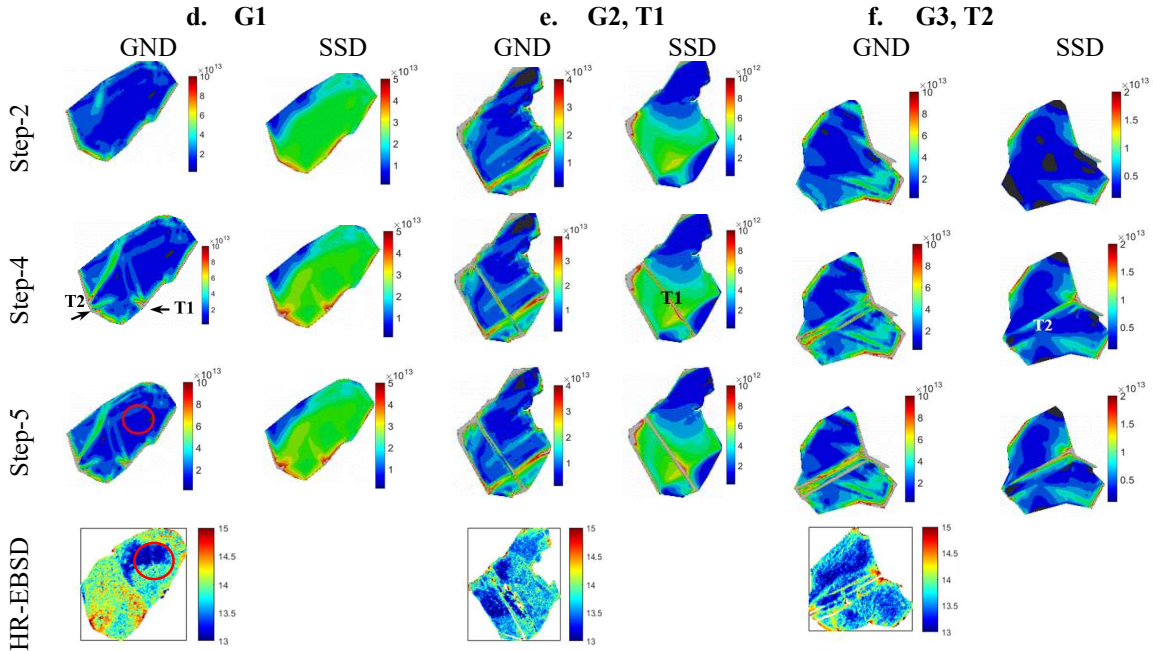
Figure 3.8 The evolution of GNDs and SSDs for the grains G1, G2 and G3: comparison between the results from the non-local model and HR-EBSD measurement. The HR-EBSD results are in logarithmic scale. The numerical results are for Step-2 (after loading), Step-4 (after twin formation) and Step-5 (after unloading).

Fig. 3.8b shows the evolution of the dislocation densities for the grain G2. Similar to G1, GNDs are more localized at the grain boundaries, but several parallel bands are observed in the model. The densities of both GNDs and SSDs increase during the twin shear transfer step. The calculated density of GNDs from CPFE agrees with that from the HR-EBSD measurement. For example, HR-EBSD results indicate a higher GND density at the grain boundaries. In addition, a higher GND density is measured at the interface of twin T1 with the grain G2, which is captured in the non-local model. The evolution of the

densities of GNDs and SSDs within the grain G3 is shown in Fig 8c. A much higher concentration of GNDs in the vicinity of the twin T2 is measured with HR-EBSD, which is captured in the numerical results. Further, both numerical and experimental results indicate a lower density for GNDs in the upper part of the grain G3.

3.4.3.3   Stress

Fig. 3.9 shows the stress along the loading direction for grains G1, G2, and G3. The general trends for the distribution of stress are the same for both non-local and conventional models. However, the non-local model predicts higher and more localized σ_{11} after the loading step. After the twin formation and with unloading the sample, a compressive σ_{11} is observed within grain G1 at its shared boundaries with the twins T1 and T2. In comparison with the conventional model, the magnitude of this compressive stress is higher for the non-local model. Results from HR-EBSD measurement also show negative σ_{11} in front of the twins similar to the model predictions. However, the calculated magnitudes from the non-local model are closer to the measured ones, i.e. about -400 MPa.
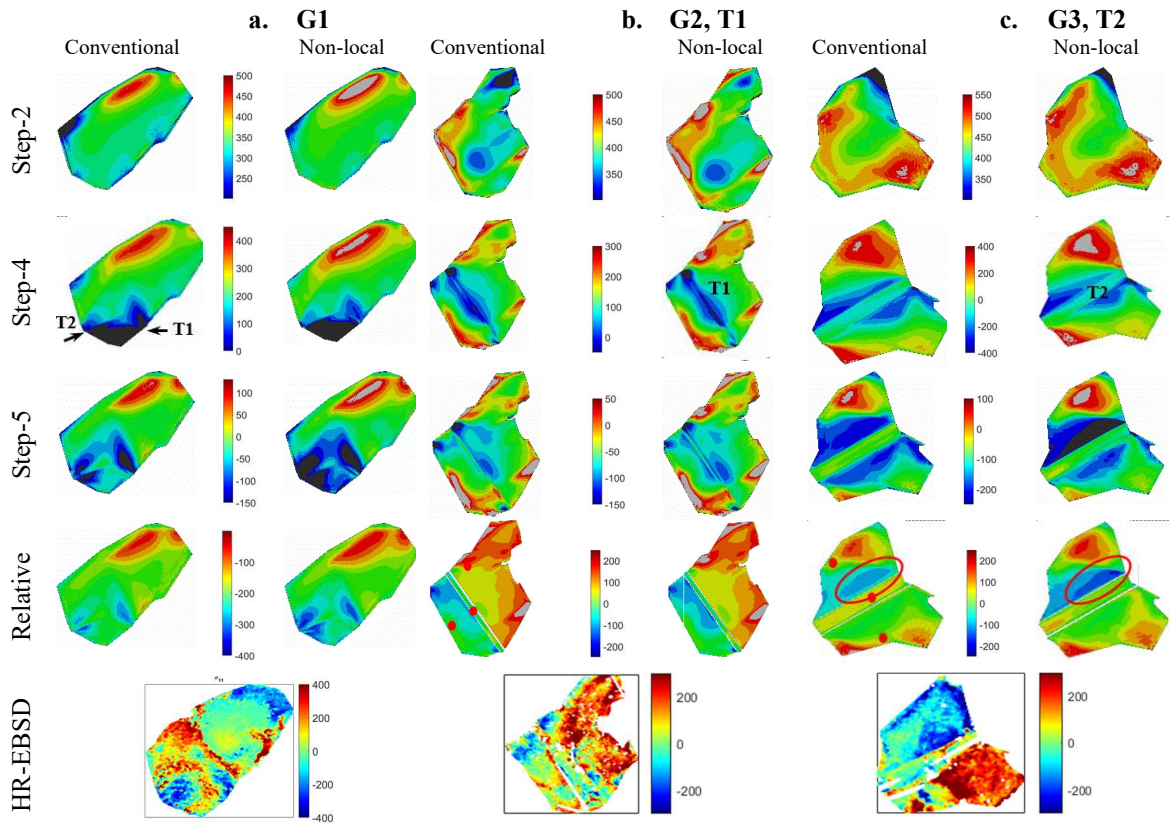
Figure 3.9 The evolution of σ₁₁ for the grains G1, G2 and G3: comparison between the results from the conventional model, the non-local model, and HR-EBSD measurement. Stresses are in MPa and the reference points are shown with the red dots. The numerical results are for Step-2 (after loading), Step-4 (after twin formation) and Step-5 (after unloading)

The distribution of σ_{11} for the grains G2 and G3 are respectively shown in Fig. 3.9b and 3.9c. Both models predict a relative tensile σ_{11} in the right-hand side of the grain G2 which is in agreement with those measured with HR-EBSD. The left-hand side of grain G2 is mainly stress free except for the upper part, which has compressive stress as observed in both numerical and experimental results. The value of the stresses measured

by the non-local model is closer to the experimental ones. The difference between the predictions from the two models is more distinct for the grain G3 (Fig. 3.9c). In the nonlocal model, the compressive σ_{11} observed in the upper part of the grain G3 is more localized at its interface with the twin T2, which is in better agreement with HR-EBSD measurement. This region is shown with a red circle in Fig. 3.8c

3.5 Discussion

In previous sections, it was shown that the calculated distribution of stress and elastic lattice rotation fields were similar from the conventional and non-local models. However, the predicted values from the two models are different such that the non-local model predicts higher localized values. The development of such localized deformation fields can significantly be affected by the size of the grain or by the sharpness of the plastic strain gradients. Such sharp gradients should be accompanied by high GND densities and hence by the development of high localized stress fields which may not be captured in conventional CPFE models due to ignoring the effects of strain gradients. Due to their lenticular geometry, sharp strain gradients can develop in twins. Therefore, in this section, numerical results for the twinned zone are compared to the experimental ones. This is followed by a discussion on the assumptions made in the CPFE model used for simulating twins. Further, a numerical study is conducted to understand when the geometrical effects of grain size become important in zirconium polycrystals.

3.5.1   Stresses and GNDs within twins

Fig. 3.10 shows the predictions of the non-local model for the density of GNDs within the twins T1 and T2, as well as within the neighbouring grain G1 at the vicinity of the twin tips. The path plots within twins are shown as "path 1" starting from point A and ending at point B, while the path plots within grain G1 are shown as "path 2" starting at

point B and ending at point C. Point B in both path plots coincide with twin tips in the vicinity of the grain G1. The numerical results are those from Step-5 so that a like-to-like comparison with HR-EBSD results can be done. The predicted densities of GNDs within the twins are in good agreement with HR-EBSD results both for trends and magnitudes. Both model and experiment show that the densities of GNDs are the highest in the vicinity of the twin tips within the twins ($\sim 10^{14.5}$ m^{-2}), while they decrease by one order of magnitude towards the twins interior ($\sim 10^{13}$ m^{-2}). Similarly, the densities of GNDs within the soft neighbouring grain G1 are the highest in the vicinity of the twin yet decrease much faster with distancing from the twin tip in the CPFE model. This is shown in the GND path 2. Grain G1, in contrast to T1 and T2, is a "big" and "equiaxed" grain where the effects of strain gradients diminish quickly with distancing from the grain boundary. In most of the studies conducted so far the calculated GNDs are an order magnitude lower than the measured one from HR-EBSD [79,80]; here we show that due to development of sharp strain gradients within the twinned zones, a better prediction of GNDs is achieved with the non-local model.
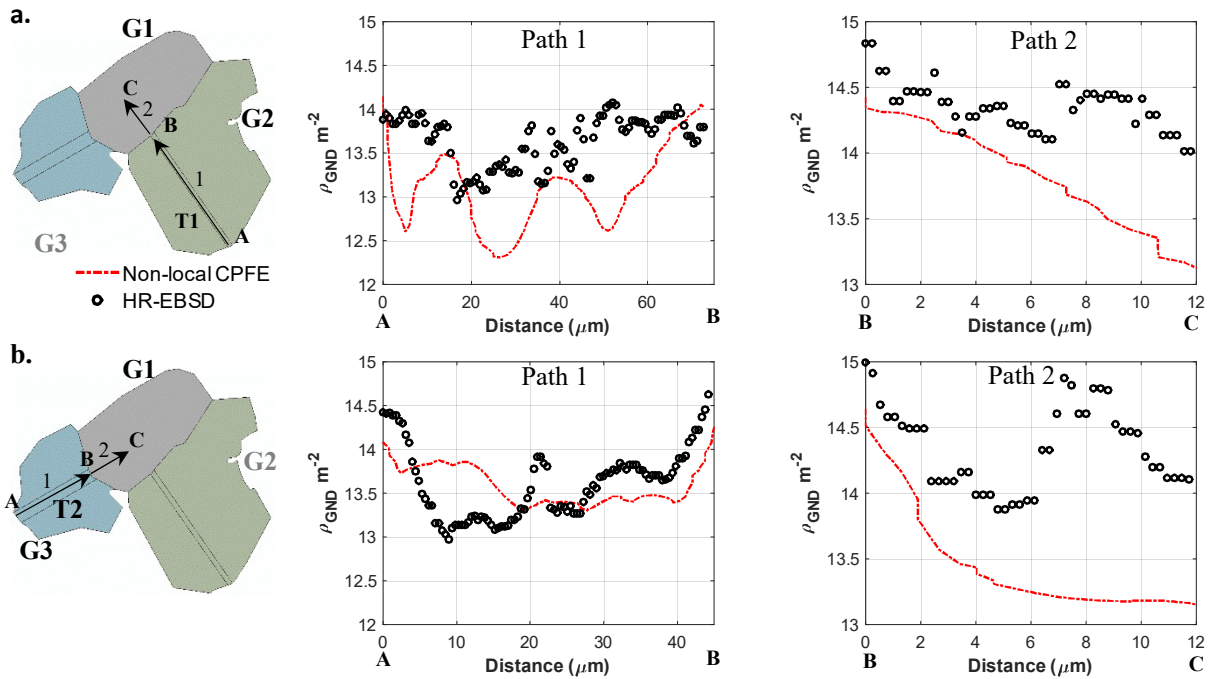
Figure 3.10 The variation of GND densities within twins (path 1) and in the vicinity of the twin tips in the neighbouring grain (path 2): comparison between the results of the non-local model and HR-EBSD for (a) T1 and (b) T2.

In Fig. 3.11, the variations of "relative" σ_{11} and σ_{22} inside the twins T1 and T2 are shown. Results are for both conventional and non-local models at Step-5 which are compared with those from the HR-EBSD measurement. While the two models show the same trend for the development of stress within the twinned zone, the difference in calculated stress from the two models is more noticeable for the twin T2 (Fig. 3.11b). For example, in a 5 μm distance from point A, the non-local model predicts a σ_{11} variation of 100 MPa, whereas the conventional model predicts a σ_{11} variation of only 50 MPa. This 50 MPa difference in σ_{11} is also observed at the other side of the twin at point B. The same trend is observed for σ_{22} where the non-local model predicts higher stresses in the vicinity of twin tips at points A and B. These variations are the areas where strain

gradients are the highest and the difference between the two models becomes more distinct. In addition, the experimental data shows a high concentration of both σ_{11} and σ_{22} in the vicinity of twin tips A and B of twin T2, while the stress within the twin relaxes towards the twin interior. Another observation that can be made is that both HR-EBSD and non-local CPFE results show a significant stress heterogeneity within twin T2.
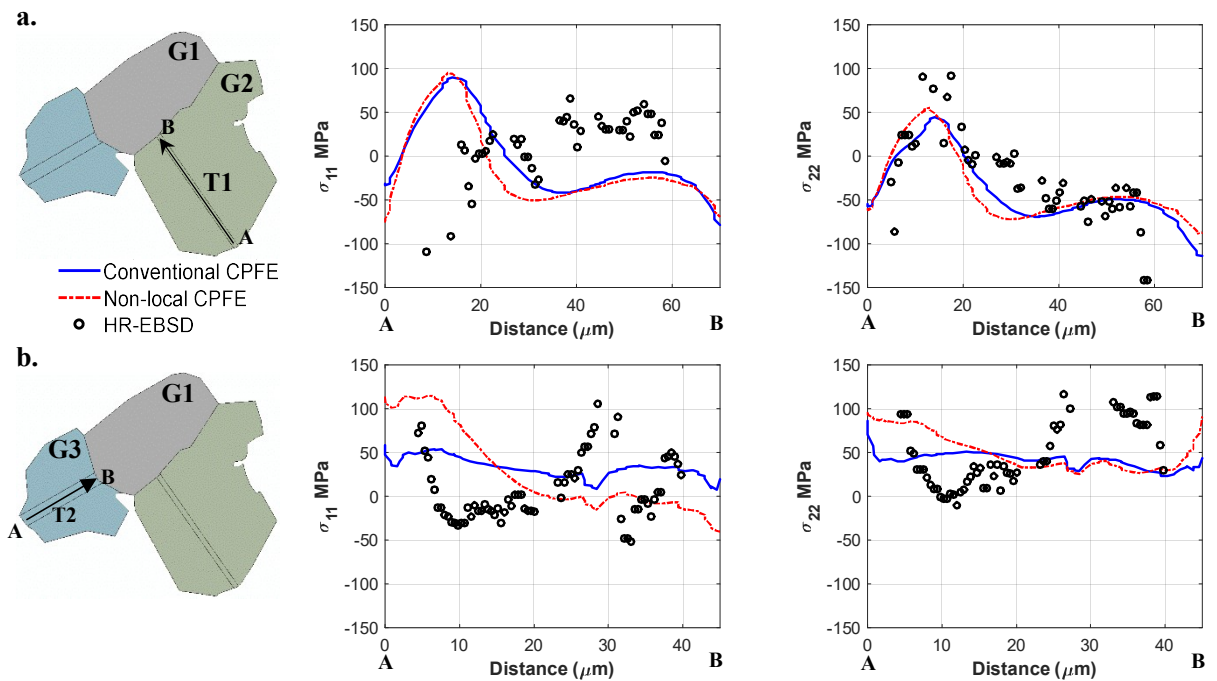
Figure 3.11 The variation of σ₁₁ and σ₂₂ calculated with the conventional and non-local models and measured with HR-EBSD within the twin (a) T1 and (b) T2. The path plots are shown in the left hand side of the figure and are from one twin tip to the other.

3.5.2   CPFE vs HR-EBSD

Many assumptions are made in simulating formation of twins with the non-local CPFE model. First, all grains measured by EBSD were extruded along the z-axis as shown in Fig. 3.5a. Many studies have shown that the sub-surface microstructure may affect the

spatial distribution of stress fields at the surface [81–85]. Since in an EBSD measurement the information regarding subsurface grains is missing, some studies have used samples with significantly large grains. This is to ensure that only one grain spans over the sample thickness. For example [82–84] studied polycrystals with average grain size of 1mm, which was as big as the sample thickness. In the current study, the average grain size is 50 μm which is much smaller than the sample thickness of 1 mm. The extent to which the calculated stress or rotation fields will vary due to sub-surface grains is unknown in the current study. Although, it was shown by Zhang et al. that changing the sub-surface microstructure for an HCP polycrystal mostly affects the magnitudes of the GND densities, elastic rotations, and strain fields, but not necessarily the observed trends at the free surface [79]. In addition, since the strains induced by twin formation are very localized, deformation fields at the vicinity of the twins are likely less affected by the arrangement of the sub-surface grains.

The modeling strategy used in this chapter is not to simulate nucleation of twins, rather to study stress field around them after the propagation and thickening stages. The twin domain is selected based on the observation made in the EBSD measurement and that the twins should be far from the edges of the EBSD map. The choice of reorienting twin domain after 2.7% is to be consistent with the applied strain in the experiment. Our study shows that as long as the twin is created at strains higher than 1%, the trends observed in the vicinity of twins in the simulated map do not significantly depend on the value of applied strain before the reorientation step. This is because zirconium does not undergo significant hardening during plastic deformation- see Fig. 3.2a. Although, the stress fields around the twin after nucleation change significantly with resuming the applied strain. In addition, the dynamic effects of twin formation are ignored in the current study as twin transformation strain was applied over 3060 seconds. To consider such effects, explicit finite element procedures should be used. Nevertheless, in another simulation, the twin

transformation strain was applied over only 1 second to study its possible effects. CPFE results for this simulation are shown in Fig. 3.12 and are compared to those for T_{TTS}= 3060. The same limits for the legends are used in each sub-figure to highlight the differences. It is shown that while the magnitude of the σ_{11} at the end of Step-4 is significantly affected, minimum variation is observed after unload. That is, stress, rotation, and GND densities at the unload are not significantly affected by the rate at which the twin transformation strain is applied. Interestingly, the same conclusion is obtained even if the external load is applied in two steps, where the twin domain reorientation and shear transformation steps are applied in between the loading steps.
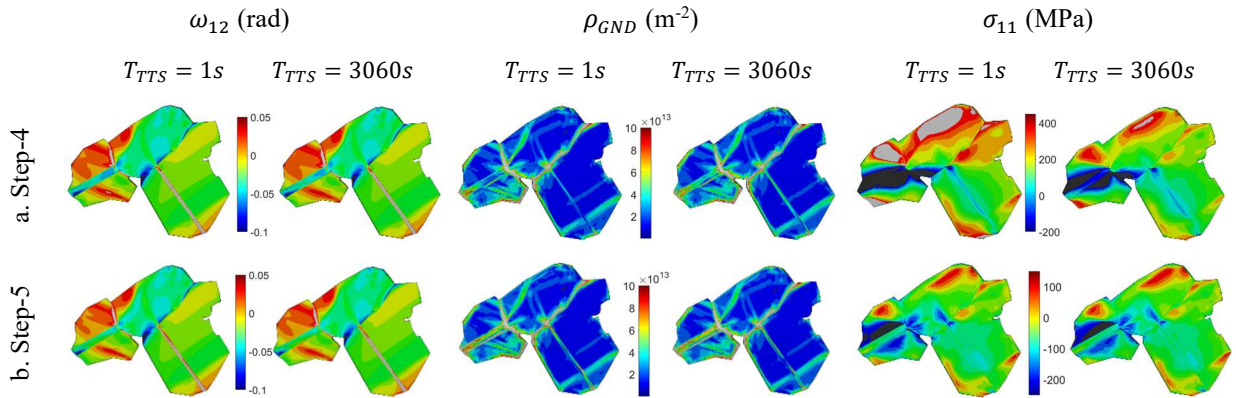
Figure 3.12 The elastic lattice rotation, total GND density and normal stress component for grains G1, G2 and G3: (a) right after applying twin transformation strain and (b) after unload.

Some discrepancies are observed between the CPFE modeling results and HR-EBSD measurements. One source of such differences is the missing subsurface microstructure. However, it should be noted that HR-EBSD is a surface-based technique where Kikuchi patterns are cross correlated to measure rotation and stress fields. In this process it is possible that density of dislocations beneath the surface becomes locally high and induce large lattice rotations. Extracting stress or elastic strain in such cases is not straight

forward as the effects of elastic strains on the movement of patterns will be overshadowed by large lattice rotations. Lastly, lower order strain gradient theory is used in this study due its simplicity in incorporating the extracted constitutive equations into the UMAT subroutine. It is suggested that the use of higher order theory helps avoid formation of unrealistic plastic strain or stress fields. In this study, the results from the developed non-local model is compared to those from a HR-EBSD map as well as those from a conventional CPFE model. This comparison does not reveal formation of such unusual fields in the simulated map. Such effects might become clearer at much higher applied strain than the one used here.

3.5.3   Effect of grain size

In all results presented so far, the evolution of stress within a grain was affected by its local neighbourhood. In this section, single crystals are used to compare the results at different grain sizes. Only the results from the non-local model is presented in this section. To be consistent with the rest of the models presented, the single crystal model shown in Fig.3. 2a is used with no alteration made to the applied boundary conditions. A uniaxial load with the same strain rate is used. In Fig. 3.13, the calculated average stress at 1%, 2%, and 4% applied strain for the examined single crystals are shown. The orientation of the HCP crystal c-axis with respect to the loading direction is changed every 10° while the size of the single crystals is varied from 2^0 μm to 2^8 (256) μm. In these simulations, the Hall-Petch effects are switched off to only study the geometrical effects of grain size on the hardening of the single crystals. As shown, at the early stages of plasticity, hardly any size effects are observed, however, by increasing the applied strain, the crystal starts to become harder at small grain sizes. It can be seen that the calculated stresses are affected when the grain size is less than 8 μm. The average grain

size of the modeled EBSD map is much higher and hence the results obtained from the two models are not very different except for the zones where strain gradients are high.

Since the Hall-Petch effects are turned off in these simulations, the trends shown in Fig. 3.13 are a combination of both materials properties and structural properties. That is, the results shown may be affected with changing the applied boundary conditions. Indeed, in a real polycrystal, the development of strain and strain gradients depends significantly on the state of the neighbouring grains and the interaction among them.
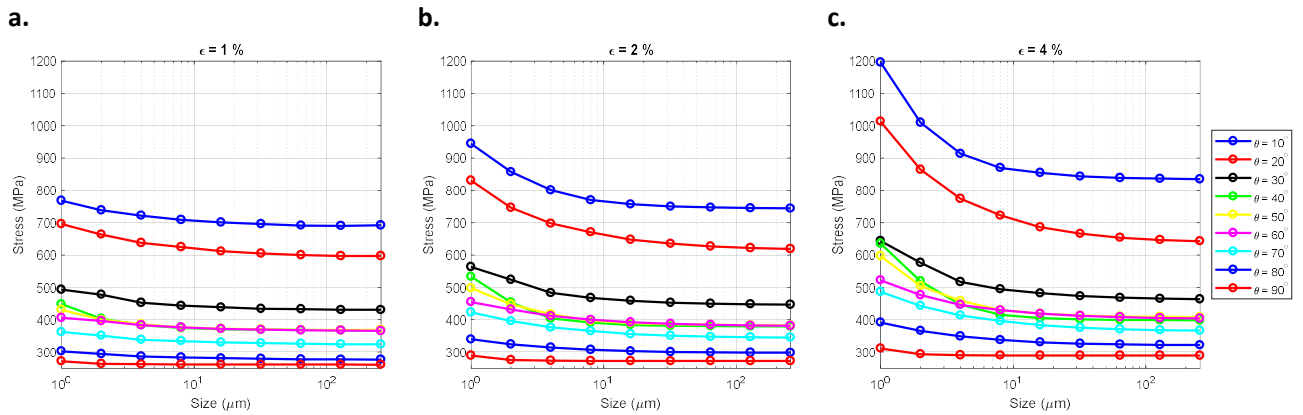
Figure 3.13 Average stress calculated for single crystals with different sizes and c-axis misorientation with respect to the loading direction. The non-local model results are presented at three different applied strains of (a) 1%, (b) 2% and (c) 4% with Hall-Petch effects switched off.

3.6 Conclusions

A non-local crystal plasticity finite element model is developed, and its performance is critically examined. The results from the non-local model is compared against those from a conventional CPFE model as well as those from two types of diffraction experiments. It is shown that:

1. the evolution of internal lattice strains measured using neutron diffraction is well captured by both non-local and conventional CPFE models. The recorded macroscopic stress-strain curves under two different loading conditions are also replicated by both models.

2. a minor difference exists between the predicted elastic lattice rotation fields from the non-local model and the conventional model.

3. the distribution of stress within individual grain from both non-local and conventional CPFE models are quite similar, since the average grain size of the studied EBSD map is relatively high. However, the non-local model predicts localized stresses with higher magnitudes which are in better agreement with those from HR-EBSD measurement. The difference between the two models becomes clearer in the areas where the gradients of plastic shear strain are sharp.

4. in agreement with the HR-EBSD measurement, the calculated densities of GNDs as well as stresses predicted by the non-local model are much higher in the vicinity of twin tips. Both GND densities and stresses are shown to decrease with distancing from the studied twin tips.

5. while the distribution of SSDs is somewhat uniform, GNDs localize in the form of slip bands where higher slip activity is calculated. Further, in agreement with the HR-EBSD measurement, higher GND density is calculated in the vicinity of grain boundaries.

References

[1]   S.R. Agnew, A. Singh, C.A. Calhoun, R.P. Mulay, J.J. Bhattacharyya, H. Somekawa, T. Mukai, B. Clausen, P.D. Wu, In-situ neutron diffraction of a quasicrystal-containing Mg alloy interpreted using a new polycrystal plasticity model of hardening due to tensile twinning, Int. J. Plast. 100 (2018) 34–51. https://doi.org/10.1016/j.ijplas.2017.09.005.

[2]   S.R. Agnew, Plastic anisotropy and the role of non-basal slip in magnesium alloy AZ31B, Int. J. Plast. 21 (2005) 1161–1193. https://doi.org/10.1016/j.ijplas.2004.05.018.

[3]   W. Wen, L. Capolungo, C.N. Tomé, Mechanism-based modeling of solute strengthening : Application to thermal creep in Zr alloy, Int. J. Plast. 106 (2018) 88–106. https://doi.org/10.1016/j.ijplas.2018.03.003.

[4]   W. Wan, F.P.E. Dunne, Microstructure-interacting short crack growth in blocky alpha, Int. J. Plast. 130 (2020) 102711. https://doi.org/10.1016/j.ijplas.2020.102711.

[5]   H. Abdolvand, K. Louca, C. Mareau, M. Majkut, J. Wright, On the nucleation of deformation twins at the early stages of plasticity, Acta Mater. 196 (2020) 733–746. https://doi.org/10.1016/j.actamat.2020.07.010.

[6]   Z. Wang, C. Cochrane, T. Skippon, Q. Dong, M.R. Daymond, Acta Materialia Dislocation evolution at a crack-tip in a hexagonal close packed metal under plane-stress conditions, Acta Mater. 164 (2019) 25–38. https://doi.org/10.1016/j.actamat.2018.10.022.

[7]   P. Platt, P. Frankel, M. Gass, M. Preuss, Critical assessment of finite element analysis applied to metal – oxide interface roughness in oxidising zirconium alloys, J. Nucl. Mater. 464 (2015) 313–319. https://doi.org/10.1016/j.jnucmat.2015.05.002.

[8]   P. Platt, D. Lunt, E. Polatidis, M.R. Wenman, M. Preuss, In-situ digital image correlation for fracture analysis of oxides formed on zirconium alloys, Corros. Sci. 111 (2016) 344–351. https://doi.org/10.1016/j.corsci.2016.05.026.

[9]   Z. Wang, Q. Dong, N. Guo, M.R. Daymond, Crack propagation path selection and plastic deformation at a crack tip in zirconium, Mater. Sci. Eng. A. 779 (2020)

139143. https://doi.org/10.1016/j.msea.2020.139143.

[10] L. Capolungo, Dislocation junction formation and strength in magnesium, Acta Mater. 59 (2011) 2909–2917. https://doi.org/10.1016/j.actamat.2011.01.026.

[11] N. Bertin, C.N. Tomé, I.J. Beyerlein, M.R. Barnett, L. Capolungo, On the strength of dislocation interactions and their effect on latent hardening in pure Magnesium, Int. J. Plast. 62 (2014) 72–92. https://doi.org/10.1016/j.ijplas.2014.06.010.

[12] H. Tummala, L. Capolungo, C.N. Tom, Quantifying the stress state in the vicinity of a d -hydride in a -zirconium, J. Nucl. Mater. 511 (2018) 406–416. https://doi.org/10.1016/j.jnucmat.2018.08.050.

[13] X. Lu, X. Zhang, M. Shi, F. Roters, G. Kang, Dislocation mechanism based size-dependent crystal plasticity modeling and simulation of gradient nano-grained copper,   Int.   J.   Plast.   113   (2019)   52–73. https://doi.org/10.1016/j.ijplas.2018.09.007.

[14] F. Han, F. Roters, D. Raabe, Microstructure-based multiscale modeling of large strain plastic deformation by coupling a full-field crystal plasticity-spectral solver with an implicit finite element solver, Int. J. Plast. 125 (2020) 97–117. https://doi.org/10.1016/j.ijplas.2019.09.004.

[15] M. Kasemer, P. Dawson, A finite element methodology to incorporate kinematic activation of discrete deformation twins in a crystal plasticity framework, Comput. Methods   Appl.   Mech.   Eng.   358   (2020)   112653. https://doi.org/10.1016/j.cma.2019.112653.

[16] C. Mareau, M.R. Daymond, Study of internal strain evolution in Zircaloy-2 using polycrystalline models : Comparison between a rate-dependent and a rate-independent   formulation,   Acta   Mater.   58   (2010)   3313–3325. https://doi.org/10.1016/j.actamat.2010.02.005.

[17] R.A. Lebensohn, A. Needleman, Numerical implementation of non-local polycrystal plasticity using fast Fourier transforms, J. Mech. Phys. Solids. 97 (2016) 333–351. https://doi.org/10.1016/j.jmps.2016.03.023.

[18] H. Wang, P.D. Wu, J. Wang, C.N. Tomé, A crystal plasticity model for hexagonal close packed (HCP) crystals including twinning and de-twinning mechanisms, Int. J. Plast. 49 (2013) 36–52. https://doi.org/10.1016/j.ijplas.2013.02.016.

[19] A. Patra, D.L. Mcdowell, Acta Materialia Crystal plasticity investigation of the microstructural factors in fl uencing dislocation channeling in a model irradiated bcc material, Acta Mater. 110 (2016) 364–376. https://doi.org/10.1016/j.actamat.2016.03.041.

[20] H. Abdolvand, Progressive modelling and experimentation of hydrogen diffusion and precipitation in anisotropic polycrystals, Int. J. Plast. 116 (2019) 39–61. https://doi.org/10.1016/j.ijplas.2018.12.005.

[21] P.W. Liu, Z. Wang, Y.H. Xiao, R.A. Lebensohn, Y.C. Liu, M.F. Horstemeyer, X.Y. Cui, L. Chen, Integration of phase-field model and crystal plasticity for the prediction of process-structure-property relation of additively manufactured metallic materials, Int. J. Plast. 128 (2020) 102670. https://doi.org/10.1016/j.ijplas.2020.102670.

[22] S. Berbenni, V. Taupin, R.A. Lebensohn, A fast Fourier transform-based mesoscale field dislocation mechanics study of grain size effects and reversible plasticity in polycrystals R, J. Mech. Phys. Solids. 135 (2020) 1–23. https://doi.org/10.1016/j.jmps.2019.103808.

[23] A. Eghtesad, K. Germaschewski, R.A. Lebensohn, M. Knezevic, A multi-GPU implementation of a full-field crystal plasticity solver for efficient modeling of high-resolution microstructures, Comput. Phys. Commun. 254 (2020) 107231. https://doi.org/10.1016/j.cpc.2020.107231.

[24] C. Mareau, M.R. Daymond, Micromechanical modelling of twinning in polycrystalline materials : Application to magnesium, Int. J. Plast. 85 (2016) 156–171. https://doi.org/10.1016/j.ijplas.2016.07.007.

[25] H. Abdolvand, J. Wright, A. Wilkinson, Strong grain neighbour effects in polycrystals, Nat. Commun. 9, 171 (2018). https://doi.org/10.1038/s41467-017-02213-9.

[26] N.G. Prastiti, Y. Xu, D.S. Balint, F.P.E. Dunne, Discrete dislocation , crystal plasticity and experimental studies of fatigue crack nucleation in single-crystal nickel, Int. J. Plast. 126 (2020) 102615. https://doi.org/10.1016/j.ijplas.2019.10.003.

[27] S. Nemat-nasser, L. Ni, T. Okinaka, A constitutive model for fcc crystals with application to polycrystalline OFHC copper, Mech. Mater. 30 (1998) 325–341.

[28] L.P. Evers, W.A.M. Brekelmans, M.G.D. Geers, Non-local crystal plasticity model with intrinsic SSD and GND effects, J. Mech. Phys. Solids. 52 (2004) 2379–2401. https://doi.org/10.1016/j.jmps.2004.03.007.

[29] U.F. Kocks, A.S. Argon, M.F. Ashby, Thermodynamics and kinetics of slip, Pergamon Press, 1975.

[30] M.F. Ashby, The deformation of plastically non-homogeneous materials, Philos. Mag. Philos. Mag. 21 (1970) 399–424.

[31] G.I. Taylor, The Mechanism of Plastic Deformation of Crystals. Part1. Theoretical, Proceeding R. Soc. 538 (1934) 362–387.

[32] A. Arsenlis, D.M. Parks, Modeling the evolution of crystallographic dislocation density in crystal plasticity, J. Mech. Phys. Solids. 50 (2002) 1979–2009.

[33] A. Arsenlis, D.M. Parks, R. Becker, V. V Bulatov, On the evolution of crystallographic dislocation density in non-homogeneously deforming crystals, J. Mech. Phys. Solids. 52 (2004) 1213–1246. https://doi.org/10.1016/j.jmps.2003.12.007.

[34] A. Arsenlis, Modeling Dislocation Density Evolution in Continuum Crystal Plasticity, PhD thesis, Massachusetts Institute of Technology, 2001.

[35] M.E. Gurtin, A gradient theory of single-crystal viscoplasticity that accounts for geometrically necessary dislocations, J. Mech. Phys. Solids. 50 (2002) 5–32.

[36] C.F. Niordson, J.W. Hutchinson, On lower order strain gradient plasticity theories, Eur. J. Mech. A/Solids. 22 (2003) 771–778. https://doi.org/10.1016/S0997-7538(03)00069.

[37] J.L. Bassani, Incompatibility and a simple gradient theory of plasticity, J. Mech. Phys. Solids. 49 (2001) 1983–1996. https://doi.org/10.1016/S0022-5096(01)00037-0.

[38] E.P. Busso, F.T. Meissonnier, N.P.O. Dowd, Gradient-dependent deformation of two-phase single crystals, J. Mech. Phys. Solids. 48 (2000) 2333–2361.

[39] A. Arsenlis, D.M. parks, Crystallographic aspects of geometrically nesesary and statistically stored dislocation density, Acta Mater. 47 (1999) 1597–1611.

[40] R. De Borst, H. -B Mühlhaus, Gradient-dependent plasticity: Formulation and algorithmic aspects, Int. J. Numer. Methods Eng. 35 (1992) 521–539. https://doi.org/10.1002/nme.1620350307.

[41] H. Gao, Y. Huang, W.D. Nix, J.W. Hutchinson, Mechanism-based strain gradient plasticity - I. Theory, J. Mech. Phys. Solids. 47 (1999) 1239–1263. https://doi.org/10.1016/S0022-5096(98)00103-3.

[42] G. Yun, K.C. Hwang, Y. Huang, P.D. Wu, A reformulation of mechanism-based strain gradient plasticity, Philos. Mag. 85 (2005) 4011–4029. https://doi.org/10.1080/14786430500363338.

[43] M.E. Gurtin, On the plasticity of single crystals: Free energy, microforces, plastic-strain gradients, J. Mech. Phys. Solids. 48 (2000) 989–1036. https://doi.org/10.1016/S0022-5096(99)00059-9.

[44] T. Ungar, M. Drakopoulos, J.L. Be, T. Chauveau, O. Castelnau, G. Riba, A. Snigirev, I. Snigireva, C. Schroer, B. Bacroix, Grain to grain slip activity in plastically deformed Zr determined by X-ray micro-diffraction line profile analysis, Acta Mater. 55 (2007) 1117–1127. https://doi.org/10.1016/j.actamat.2006.09.031.

[45] Y. Guo, D.M. Collins, E. Tarleton, F. Hofmann, A.J. Wilkinson, T. Ben Britton, Dislocation density distribution at slip band-grain boundary intersections, Acta Mater. 182 (2020) 172–183. https://doi.org/10.1016/j.actamat.2019.10.031.

[46] A.J. Wilkinson, G. Meaden, D.J. Dingley, High-resolution elastic strain measurement from electron backscatter diffraction patterns: New levels of sensitivity, Ultramicroscopy. 106 (2006) 307–313. https://doi.org/10.1016/j.ultramic.2005.10.001.

[47] A.J. Wilkinson, Measurement of elastic strains and small lattice rotations using electron back scatter diffraction, Ultramicroscopy. 62 (1996) 237–247.

[48] K. Troost, P. van der Sluis, D. Gravesteijn, Microscale elastic-strain determination by backscatter Kikuchi diffraction in the scanning electron microscope, Appl. Phys. Lett. 62 (1993) 1110–1112.

[49] T.B. Britton, a. J. Wilkinson, High resolution electron backscatter diffraction measurements of elastic strain variations in the presence of larger lattice rotations, Ultramicroscopy. 114 (2012) 82–95.

https://doi.org/10.1016/j.ultramic.2012.01.004.

[50] Y. Guo, H. Abdolvand, T.B. Britton, A.J. Wilkinson, Growth of { 1122 } twins in titanium : A combined experimental and modelling investigation of the local state of deformation, Acta Mater. 126 (2017) 221–235. https://doi.org/10.1016/j.actamat.2016.12.066.

[51] M.T. Andani, A. Lakshman, M. Karamooz-ravari, A quantitative study of stress fields ahead of a slip band blocked by a grain boundary in unalloyed magnesium, Sci. Reports 10. 3084 (2020). https://doi.org/10.1038/s41598-020-59684-y.

[52] Y. Guo, T.B. Britton, A.J. Wilkinson, Slip band – grain boundary interactions in commercial-purity titanium, Acta Mater. 76 (2014) 1–12. https://doi.org/10.1016/j.actamat.2014.05.015.

[53] R. Pokharel, A. Patra, D.W. Brown, B. Clausen, S.C. Vogel, G.T. Gray, An analysis of phase stresses in additively manufactured 304L stainless steel using neutron diffraction measurements and crystal plasticity finite element simulations, Int. J. Plast. 121 (2019) 201–217. https://doi.org/10.1016/j.ijplas.2019.06.005.

[54] H. Zhang, A. Jérusalem, E. Salvati, C. Papadaki, K. Soon, X. Song, A.M. Korsunsky, Multi-scale mechanisms of twinning-detwinning in magnesium alloy AZ31B simulated by crystal plasticity modeling and validated via in situ synchrotron XRD and in situ SEM-EBSD, Int. J. Plast. 119 (2019) 43–56. https://doi.org/10.1016/j.ijplas.2019.02.018.

[55] F. Long, L. Balogh, D.W. Brown, P. Mosbrucker, T. Skippon, C.D. Judge, M.R. Daymond, Effect of neutron irradiation on deformation mechanisms operating during tensile testing of Zr-2.5Nb, Acta Mater. 102 (2016) 352–363. https://doi.org/10.1016/j.actamat.2015.09.032.

[56] H. Abdolvand, M.R. Daymond, C. Mareau, Incorporation of twinning into a crystal plasticity finite element model: Evolution of lattice strains and texture in Zircaloy-2, Int. J. Plast. 27 (2011) 1721–1738. https://doi.org/10.1016/j.ijplas.2011.04.005.

[57] H. Abdolvand, A.J. Wilkinson, On the effects of reorientation and shear transfer during twin formation: Comparison between high resolution electron backscatter diffraction experiments and a crystal plasticity finite element model, Int. J. Plast. 84 (2016) 160–182. https://doi.org/10.1016/j.ijplas.2016.05.006.

[58] P. Müllner, C. Solenthaler, P.J. Uggowitzer, M.O. Speidel, Brittle fracture in austenitic steel, Acta Metall. Mater. 42 (1994) 2211–2217. https://doi.org/10.1016/0956-7151(94)90300-X.

[59] M. Koyama, E. Akiyama, K. Tsuzaki, D. Raabe, Hydrogen-assisted failure in a twinning-induced plasticity steel studied under in situ hydrogen charging by electron channeling contrast imaging, Acta Mater. 61 (2013) 4607–4618. https://doi.org/10.1016/j.actamat.2013.04.030.

[60] A. Stoll, A.J. Wilkinson, Simulation of deformation twins and their interactions with cracks, Comput. Mater. Sci. 89 (2014) 224–232. https://doi.org/10.1016/j.commatsci.2014.03.041.

[61] R.J. Asaro, A. Needleman, Overview No. 42 Texture developement and strain hardening in rate dependant polycrystals, Acta Metall. 33 (1985) 923–953.

[62] C. Tome, G.R. Canova, U.F. Kocks, N. Christodoulou, J.J. Jonas, The relation between macroscopic and microscopic strain hardening in FCC polycrystals, Acta Metall. 32 (1984) 1637–1653.

[63] R.J. Asaro, Crystal Plasticity, J. Appl. Mech. 50 (1983) 921–934.

[64] E.S. Fisher, C.J. Renken, Single-Crystal Elastic Moduli and the hcp ~ bcc Transformation in Ti, Zr, and Hf, Phys. Rev. 135 (1964) A482–A494.

[65] A. Kumar, A.K. Kanjarla, S.R. Niezgoda, R.A. Lebensohn, C.N. Tome, Numerical study of the stress state of a deformation twin in magnesium, Acta Mater. 84 (2015) 349–358. https://doi.org/10.1016/j.actamat.2014.10.048.

[66] Z. Zhang, M.A. Cuddihy, F.P.E. Dunne, On rate-dependent polycrystal deformation : the temperature sensitivity of cold dwell fatigue, Proc.R.Soc.A. 471:201502 (2015). https://doi.org/http://dx.doi.org/10.1098/rspa.2015.0214.

[67] A. Ma, F. Roters, D. Raabe, A dislocation density based constitutive model for crystal plasticity FEM including geometrically necessary dislocations, Acta Mater. 54 (2006) 2169–2179. https://doi.org/10.1016/j.actamat.2006.01.005.

[68] J.F. Nye, Some geometrical relations in dislocated crystals, Acta Metall. 1 (1953) 153–162.

[69] A. Acharya, J.L. Bassani, Lattice incompatibility and a gradient theory of crystal

plasticity, J. Mech. Phys. Solids. 48 (2000) 1565–1595.

[70] P. Cermelli, M.E. Gurtin, On the characterization of geometrically necessary dislocations in finite plasticity, J. Mech. Phys. Solids. 49 (2001) 1539–1568.

[71] U.F. Kocks, H. Mecking, Physics and phenomenology of strain hardening : the FCC case, Prog. Mater. Sci. 48 (2003) 171–273.

[72] K.S. Cheong, E.P. Busso, A. Arsenlis, A study of microstructural length scale effects on the behaviour of FCC polycrystals using strain gradient concepts, Int. J. Plast. 21 (2005) 1797–1814. https://doi.org/10.1016/j.ijplas.2004.11.001.

[73] F.P.E. Dunne, D. Rugg, A. Walker, Lengthscale-dependent, elastically anisotropic, physically-based hcp crystal plasticity: Application to cold-dwell fatigue in Ti alloys, Int. J. Plast. 23 (2007) 1061–1083. https://doi.org/10.1016/j.ijplas.2006.10.013.

[74] J. Cheng, S. Ghosh, A crystal plasticity FE model for deformation with twin nucleation in magnesium alloys, Int. J. Plast. 67 (2015) 148–170. https://doi.org/10.1016/j.ijplas.2014.10.005.

[75] H. Abdolvand, M.R. Daymond, Multi-scale modeling and experimental study of twin inception and propagation in hexagonal close-packed materials using a crystal plasticity finite element approach; Part II: Local behavior, J. Mech. Phys. Solids. 61 (2013) 803–818. https://doi.org/10.1016/j.jmps.2012.10.017.

[76] I.J. Beyerlein, C.N. Tome, A dislocation-based constitutive law for pure Zr including temperature effects, 24 (2008) 867–895. https://doi.org/10.1016/j.ijplas.2007.07.017.

[77] F. Xu, R.A. Holt, M.R. Daymond, Modeling lattice strain evolution during uniaxial deformation of textured Zircaloy-2, Acta Mater. 56 (2008) 3672–3687. https://doi.org/10.1016/j.actamat.2008.04.019.

[78] A. Alawadi, H. Abdolvand, Measurement and modeling of micro residual stresses in zirconium crystals in three dimension, J. Mech. Phys. Solids. 135 (2020) 103799. https://doi.org/10.1016/j.jmps.2019.103799.

[79] Z. Zhang, D. Lunt, H. Abdolvand, A.J. Wilkinson, M. Preuss, F.P.E. Dunne, Quantitative investigation of micro slip and localization in polycrystalline materials under uniaxial tension, Int. J. Plast. 108 (2018) 88–106.

https://doi.org/10.1016/j.ijplas.2018.04.014.

[80] H. Liang, F.P.E. Dunne, GND accumulation in bi-crystal deformation: Crystal plasticity analysis and comparison with experiments, Int. J. Mech. Sci. 51 (2009) 326–333. https://doi.org/10.1016/j.ijmecsci.2009.03.005.

[81] A. Zeghadi, S. Forest, A.F. Gourgues, O. Bouaziz, Ensemble averaging stress-strain fields in polycrystalline aggregates with a constrained surface microstructure-part 2: Crystal plasticity, Philos. Mag. 87 (2007) 1425–1446. https://doi.org/10.1080/14786430601009517.

[82] Z. Zhao, M. Ramesh, D. Raabe, A.M. Cuitiño, R. Radovitzky, Investigation of three-dimensional aspects of grain-scale plastic surface deformation of an aluminum oligocrystal, Int. J. Plast. 24 (2008) 2278–2297. https://doi.org/10.1016/j.ijplas.2008.01.002.

[83] H. Lim, J.D. Carroll, C.C. Battaile, T.E. Buchheit, B.L. Boyce, C.R. Weinberger, Grain-scale experimental validation of crystal plasticity finite element simulations of tantalum oligocrystals, Int. J. Plast. 60 (2014) 1–18. https://doi.org/10.1016/j.ijplas.2014.05.004.

[84] P. Baudoin, T. Hama, H. Takuda, Influence of critical resolved shear stress ratios on the response of a commercially pure titanium oligocrystal: Crystal plasticity simulations and experiment, Int. J. Plast. 115 (2019) 111–131. https://doi.org/10.1016/j.ijplas.2018.11.013.

[85] L. St-Pierre, E. Héripré, M. Dexet, J. Crépin, G. Bertolino, N. Bilger, 3D simulations of microstructure and comparison with experimental microstructure coming from O.I.M analysis, Int. J. Plast. 24 (2008) 1516–1532. https://doi.org/10.1016/j.ijplas.2007.10.004.

Chapter 4

4 Strain gradient crystal plasticity finite element modeling of slip band formation in α-zirconium

Two methods for the determination of geometrically necessary dislocation (GND) densities are implemented in a lower-order strain-gradient crystal plasticity finite element model. The equations are implemented in user material (UMAT) subroutines. Method I has a direct and unique solution for the density of GNDs, while Method II has unlimited solutions, where an optimization technique is used to determine GND densities. The performance of each method for capturing the formation of slip bands based on the calculated GND maps is critically analyzed. First, the model parameters are identified using single crystal simulations. Afterwards, the as-measured microstructure for α-zirconium polycrystal is imported into the finite element solver to compare the numerical results obtained from the models to those measured experimentally using the high resolution electron backscatter diffraction method. It is shown that both methods are capable of modeling the formation of slip bands that are parallel to those observed experimentally. Formation of such bands are observed in both GND maps and plastic shear strain maps without pre-determining the slip band domain. Further, there is a negligible difference between the calculated grain-scale stresses and elastic lattice rotations from the two methods, where the modeling results are close to the measured ones. However, the magnitudes and distributions of calculated GND densities from the two methods are very different.

4.1 Introduction

Crystal plasticity is a class of constitutive equations that can be used to describe deformation mechanisms of polycrystalline materials at the grain-scale [1–3]. It has been used in many studies to understand the evolution of heterogeneous deformation fields within individual grains in "real" time-scale [4–7]. A significant number of crystal plasticity studies have focused on modeling deformation by slip, which is controlled by the movement of dislocations on a particular plane known as the slip plane, and in a particular direction known as the slip direction. The strength of the obstacles interacting with dislocations determines the resistance of a slip system to the movement of the dislocations and the consequent material hardening. These obstacles can be categorized into short-range barriers and the long-range barriers [8]. The intersecting dislocations are usually assumed as the primary short-range barriers. The long-range obstacles may include the elastic stress field induced by far field dislocations. The long-range obstacles are affected by the density of the geometrically necessary dislocations (GNDs), while the development of both statistically stored dislocations (SSDs) and GNDs can increase the short-range effects [9,10]. When conventional crystal plasticity models are used, the difference between these two obstacles is generally ignored and the critical resolved shear stress (CRSS) for the movement of the dislocations does not depend on the deformation state in the neighboring points. However, the plastic response of a polycrystal depends on both the local state of deformation and the gradients of the plastic strain. Incorporation of the plastic strain gradient in crystal plasticity constitutive equations makes the model response dependent on the neighboring elements- this is generally investigated in the non-local approach of crystal plasticity [11–15]. The strain-gradient plasticity theories can be formulated in the lower-order and higher-order approaches [16]. In the lower-order approach [17–19], the plastic strain gradient terms are only incorporated in the hardening laws. However, in the higher-order approach, the equilibrium equations are

also adjusted [20–23]. This chapter focuses on examining the methods available in the literature for calculating GND densities in the lower-order crystal plasticity framework by providing a direct comparison between the results of each method to those measured experimentally.

GND densities are inherently linked to the lattice curvature and can be determined using the gradients of plastic strain [24]. The derivation of the dislocation densities from the "curl" of the deformation gradient in the Nye equation has been accompanied with inconsistencies in the literature, some of which have been reported by Das et al. [25]. Generally, two methods are used in the literature for extracting GNDs using Nye equations. In the first method, the contribution of each slip system, e.g. α, to GND density is assumed to be proportional to the plastic shear accommodated on the same slip system α. Hence, the number of linear equations that should be solved is equal to the number of unknowns, i.e., GNDs on each slip system α. This is called the direct method where the density of GNDs on each slip system is determined unambiguously. The direct method was initially proposed by Dai [26] and was subsequently implemented in the crystal plasticity finite element (CPFE) models [10,18,27–29]. In the second method, the cumulative contribution of plastic shears on all slip systems to the total GND densities is assumed to be proportional to the Nye tensor. This usually results in a set of equations where the number of unknowns is more than the number of equations. Two main approaches are suggested for determining the unknowns. In the first approach, known as L^1, a solution is found by minimizing the dislocation line energy. In the second approach, known as L^2, a solution is found by minimizing the dislocation densities squares summation [30]. Das et al. showed that the use of L^2 method leads to a solution where dislocation densities are evenly distributed on all slip systems, while the use of L^1 method leads to capturing some variations of GNDs between the slip systems [25]. Negligible difference was found between the magnitudes of the total dislocation densities obtained

from the two minimization approaches. The L^2 minimization approach has been widely used in the CPFE models [31–34]. In contrast to the direct method which provides a unique solution for the GND density on each slip system, both minimization approaches lead to non-unique solutions. Therefore, an investigation is required to compare the magnitudes and distributions of the obtained GND densities from these two methods.

The measurement of internal stress and dislocation densities helps validate dislocation-based crystal plasticity models. Diffraction methods can be used for measurement of the elastic lattice strains [35–38], stress distributions [38,39] as well as the dislocation densities [40]. For example, the dislocation densities y of slip bands were measured using micro X-ray diffraction [41].Although a three-dimensional view of the dislocation densities are provided, only a few grains can be studied in this technique. High angular resolution electron back scatter diffraction (HR-EBSD) technique can be used to measure "relative" elastic strains and rotations, and "absolute" GND densities for many grains, yet close to the sample surface. Diffraction patterns are collected and then cross correlated using a reference pattern. The deformation gradient tensor is then calculated, and used to determine the relative elastic strain tensor [42–45] and GND densities using Nye tensor [46]. Many studies have used HR-EBSD to compare the numerically obtained GND densities from CPFE models to the measured ones [47–50].

The objectives of this chapter are to compare the GND densities calculated using the direct method to those obtained from the minimization-based method and investigate the capability of the GND-based CPFE models in capturing the formation of slip bands in an α-zirconium polycrystal. Hence, the direct and the minimization-based methods for calculating GND densities are formulated and implemented in a lower-order strain-gradient CPFE model. After calibrating single crystal parameters, the evolution of GND and SSD densities predicted by each method is studied in detail using single crystal FE

models. The capability of the developed non-local models in capturing the experimentally observed slip bands of a deformed polycrystalline α-zirconium is subsequently investigated. This is followed by comparing the results of the models for GND densities, stresses, and elastic rotations to those measured by HR-EBSD.

4.2   Sample preparation and experimental set-up

Blocks of α-zirconium material were firstly annealed at 700 °C and then air cooled to relieve residual stresses as much as possible. A dog-bone sample was subsequently made with gauge length of 20 mm. The sample was mechanical polishing down to 4000 grit, followed by polishing in a 50 nm colloidal silica suspension, and electropolishing in a -30 °C solution of 90% methanol and 10% perchloric acid for 60 s at 25 V. The cross section of the sample after polishing was measured to be 0.5×0.5 mm^2.

The sample was uniaxially deformed at room temperature under strain control to a tensile strain of 1.2% using strain rate of 2.6×10^{-5} s^{-1}. The EBSD measurement was performed in a Zeiss MERLIN field emission gun scanning electron microscope (FEG-SEM) with 20 keV beam energy, 15 nA probe current, and at the working distance of 18 mm. Diffraction patterns were collected every 0.5 μm using a Bruker high resolution EBSD detector. Following the method developed by Wilkinson et al. [42], elastic strain and lattice rotations were calculated by cross correlating the collected 800×800 pixels Kikuchi patterns [51]. An EBSD map of the deformed sample with the coordinate system used is shown in Fig. 4.1a. As shown, the x-axis coincides with the loading direction, z-axis is along the electron beam direction and sample thickness, and y-axis is defined by the cross product of the other two axes. In addition, as shown in Fig. 4.1b, the c-axis of the HCP crystals is oriented towards the z-axis with a little spread towards the x-axis. Since the specimen was only deformed to 1.2% and the c-axis of most of the crystals are perpendicular to the loading direction, deformation twinning was not active in this

experiment. No twin was observed in the EBSD and the ARGUS images taken from sample after deformation (see Fig. 4.5c and 4.5d). As such the effects of twinning are ignored in all mathematical formulation and CPFE modeling.
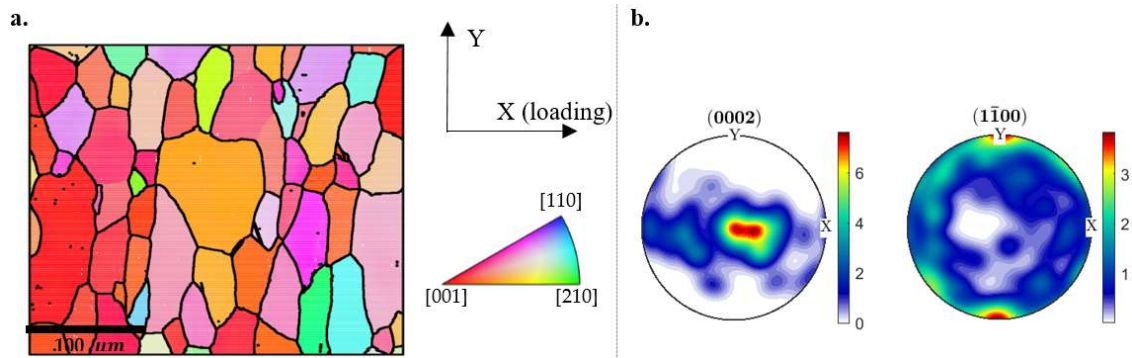
Figure 4.1 (a) An inverse pole figure-Z of the sample with the corresponding pole figure shown in (b).

4.3 Crystal plasticity formulation and input model

In this section the constitutive equations implemented for calculating GND densities using both the direct and minimization-based methods are described. Here, the direct and minimization-based methods are called "Method I" and "Method II", respectively. These equations are implemented in a User MATerial (UMAT) subroutine originally developed by Abdolvand et al. [52] and recently updated by Sedaghat and Abdolvand [47]. After describing the implemented constitutive equations, the steps followed to prepare the FE input model are presented.

4.3.1 Crystal plasticity constitutive equations

The total deformation gradient (F) can be decomposed to the elastic (F^e) and plastic (F^p) parts:

$$F = F^e F^p \tag{4-1}$$

The total velocity gradient tensor (L) in the current configuration can be divided into the elastic (L^e) and plastic (L^p) parts as:

$$L = \dot{F}F^{-1} = \dot{F}^e F^{e-1} + F^e \dot{F}^p F^{p-1} F^{e-1} = L^e + L^p \tag{4-2}$$

The total velocity gradient tensor can be divided into its symmetric part, i.e. deformation rate tensors (D^e, D^p), and asymmetric part, i.e. spin tensors (Ω^e, Ω^p). The time integration of deformation rate tensor and spin tensor, respectively provides the increments of the strain and rotation tensors. The plastic part of the velocity gradient tensor is calculated using the following equation [53]:

$$L^p = D^p + \Omega^p = \sum_{\alpha=1}^{N} \dot{\gamma}^\alpha \vec{m}^\alpha \otimes \vec{n}^\alpha \tag{4-3}$$

where $\vec{m}^\alpha$, $\vec{n}^\alpha$ and $\dot{\gamma}^\alpha$ respectively represent the slip direction, the slip plane normal, and the shear rate on the αth slip system for the N number of active slip systems. $\vec{m}^\alpha \otimes \vec{n}^\alpha$ is known as the Schmid tensor of the slip system α. The shear rate on the slip system α is calculated based on the resolved shear stress (τ^α) acting on the same slip system [53]:

$$\dot{\gamma}^\alpha = \dot{\gamma}_0^\alpha \ \text{sign}(\frac{\tau^\alpha}{g^\alpha}) \ \left|\frac{\tau^\alpha}{g^\alpha}\right|^n \tag{4-4}$$

where $\dot{\gamma}_0$ is a reference shear strain rate, n represents the sensitivity of the material to a strain rate and g^α is the CRSS of the slip system α. The resolved shear stress acting on the slip system α is proportional to Kirchhoff stress (ψ) through the following equation [54]:

$$\tau^\alpha = \boldsymbol{P}^\alpha : \boldsymbol{\psi} \tag{4-5}$$

where $\boldsymbol{P}^\alpha$ is the symmetric part of the Schmid tensor. The Jaumann rate of the Kirchhoff stress tensor ($\breve{\boldsymbol{\psi}}$) is related to the elastic part of the deformation rate tensor ($\boldsymbol{D}^e$) and the elastic stiffness tensor ($\mathbb{C}$) of the HCP crystal after rotation to the deformed configuration as:

$$\breve{\boldsymbol{\psi}} = \mathbb{C} : \boldsymbol{D}^e \tag{4-6}$$

The elastic modulus of zirconium HCP crystals used in this study is the one determined by Fisher and Renken [55]: C_{11}=143.5 GPa, C_{33}=164.9 GPa, C_{12}=72.5 GPa, C_{13}=65.4 GPa, and C_{44}=32.1 GPa. The objective rate of Kirchhoff stress, in Eq. (4-6), is defined as:

$$\breve{\boldsymbol{\psi}} = \dot{\boldsymbol{\psi}} - \boldsymbol{\Omega}^e \boldsymbol{\psi} + \boldsymbol{\psi} \boldsymbol{\Omega}^e \tag{4-7}$$

The strength of each slip system (g^α) in Eq. (4-4) follows a dislocation-based hardening law [10–12,27]:

$$\tag{4-8}$$
$$g^\alpha = g_{*,0}^\alpha + \frac{H^\alpha}{\sqrt{D}} + \xi G b^\alpha \sqrt{\sum_{\beta=1}^{N} q^{\alpha\beta} \left(\rho_{GND}^\beta + \rho_{SSD}^\beta \right)}$$
$$= g_{*,0}^\alpha + \frac{H^\alpha}{\sqrt{D}} + \xi G b^\alpha \sqrt{\rho_T}$$

where g^α is the updated CRSS, $g_{*,0}^\alpha$ is the initial CRSS, D is the equivalent grain diameter, H^α is Hall-Petch parameter for slip system α, ξ is a material constant, G is the shear modulus, b^α is the size of the Burgers vector for the slip system α, ρ_{GND}^β and ρ_{SSD}^β are the GND and SSD densities on the slip system β. A hardening matrix $q^{\alpha\beta}$ is

introduced to consider the effects of self and latent-hardening. For the sake of simplicity in deriving a solution, the term under the radical is called ρ_T. It is assumed that the GND and SSD densities have the same hardening matrix $q^{\alpha\beta}$. The shear modulus, G in Eq. (4-8), is assumed to be the average value of C_{44}, C_{55}, and C_{66} [56]. The material constant ξ is assumed to be 0.5.

It is assumed that the evolution of SSD densities follows the equation below [10,57]:

$$\dot{\rho}_{SSD}^{\alpha} = \frac{|\dot{\gamma}^{\alpha}|}{b^{\alpha}} \left(K^{\alpha}\sqrt{\rho_{SSD}^{\alpha} + \rho_{GND}^{\alpha}} - 2y_c^{\alpha}\,\rho_{SSD}^{\alpha} \right) \tag{4-9}$$

where K^{α} is the dislocation accumulation constant and y_c^{α} is the dislocation annihilation length. The first term in the right-hand side of the Eq. (4-9) is the dominant term at the early stages of plasticity while with further loading, the effects of the second term will be non-negligible. In the following sub-sections, the two methods used for calculating GND densities are presented.

4.3.1.1   Method I

In the first method, the GND density of the slip system α is uniquely correlated with the resolved shear strain accumulated on the same system [26]:

$$\dot{\rho}_{GND}^{\alpha} = \frac{\dot{\gamma}^{\alpha}}{b^{\alpha}} \left| Curl[\vec{n}_j^{\alpha}\,F_{ji}^{p}] \right| = \frac{\dot{\gamma}^{\alpha}}{b^{\alpha}} \left| \epsilon_{ikq} \frac{\partial(\vec{n}_j^{\alpha}\,F_{jq}^{p})}{\partial x_k} \right| \tag{4-10}$$

where ϵ_{ikq} is the permutation tensor. Hence, ρ_{GND}^{α} has a unique solution. For implementing Eqs. 8-10 into the UMAT, the time derivative of Eq. (4-8) is firstly calculated and coupled with Eqs. (9) and (10) to solve for the increments of shear strains using the Newton-Raphson iterative algorithm. The evolution of CRSS can be reformulated by taking the time derivative of Eq. (4-8):

$$\dot{g}^\alpha = \xi G b^\alpha \frac{\dot{\rho}_T}{2\sqrt{\rho_T}}, \quad \text{where } \dot{\rho}_T = \sum_{\beta=1}^{N} q^{\alpha\beta} \left(\dot{\rho}_{GND}^\beta + \dot{\rho}_{SSD}^\beta \right) \tag{4-11}$$

By substituting Eqs. (4-9) and (4-10) into Eq. (4-11) we have:

$$\dot{g}^\alpha = \sum_{\beta=1}^{N} \left[q^{\alpha\beta} \frac{\xi G b^\alpha}{2 b^\beta \sqrt{\rho_T}} \left(\left| \epsilon_{ikq} \frac{\partial \left(\vec{n}_j^\alpha \, F_{jq}^p \right)}{\partial x_k} \right| + K^\beta \sqrt{\rho_{SSD}^\beta + \rho_{GND}^\beta} \right. \right.$$
$$\left. \left. - 2 y_c^\beta \, \rho_{SSD}^\beta \right) \right] \dot{\gamma}^\beta \tag{4-12}$$

The complexity of implementation of this method in the UMAT subroutine is calculation of the gradient term, which was originally developed by Abdolvand [58].

4.3.1.2 Method II

In the second method, the density of GNDs on the slip system α is defined as [30]:

$$\left(curl \left(F^{p^T} \right) \right)^T = \sum_{\alpha=1}^{N} \left(\rho_{GND,s}^\alpha \, \vec{b}^\alpha \otimes \vec{m}^\alpha + \rho_{GND,et}^\alpha \, \vec{b}^\alpha \otimes \vec{t}^\alpha \right.$$
$$\left. + \, \rho_{GND,en}^\alpha \, \vec{b}^\alpha \otimes \vec{n}^\alpha \right) \tag{4-13}$$

ρ_{GND}^α for each slip system can be decomposed into three components, one for screw type dislocation $\rho_{GND,s}^\alpha$, and two edge types dislocations, $\rho_{GND,en}^\alpha$ and $\rho_{GND,et}^\alpha$ with $t^\alpha = m^\alpha \times n^\alpha$, respectively. In contrast to method I, method II has infinite solutions where a minimization scheme is usually used to find a solution. Eq. (4-13) can be solved by minimizing the sum of the squares of GND densities [19]:

$$\{\rho_{GND}^{\alpha}\} = A^T (AA^T)^{-1} B \tag{4-14}$$

where $\{\rho_{GND}^{\alpha}\}$ is 3N×1 column vector including the components of GND for slip system α, B is a 9×1 vector, containing the curl function components in Eq. (4-13), and A is a 9×3N matrix with the basis tensors of Eq. (4-13). The time derivative of Eq. (4-13) is determined as:

$$\left(curl(\dot{F}^{p^T})\right)^T = \sum_{\alpha=1}^{N} \left(\dot{\rho}_{GND,s}^{\alpha} \, \vec{b}^{\alpha} \otimes \vec{m}^{\alpha} + \dot{\rho}_{GND,et}^{\alpha} \, \vec{b}^{\alpha} \otimes \vec{t}^{\alpha} \right. \tag{4-15}$$
$$\left. + \, \dot{\rho}_{GND,en}^{\alpha} \, \vec{b}^{\alpha} \otimes \vec{n}^{\alpha} \right)$$

By substituting Eq. (4-15) and (4-9) into Eq. (4-11), we have:

$$\dot{g}^{\alpha} = \sum_{\beta=1}^{N} \frac{q^{\alpha\beta} \xi G b^{\alpha} (K^{\beta} \sqrt{\rho_{SSD}^{\beta} + \rho_{GND}^{\beta}} - 2y_c^{\beta} \, \rho_{SSD}^{\beta})}{2b^{\beta} \sqrt{\rho_T}} \cdot |\dot{\gamma}^{\beta}| \tag{4-16}$$
$$+ \sum_{\beta=1}^{N} \frac{q^{\alpha\beta} \xi G b^{\alpha} (\dot{\rho}_{GND}^{\beta})}{2b^{\beta} \sqrt{\rho_T}}$$

Similar to method I, the first term in the right-hand side of Eq. (4-16) shows an explicit correlation between the shear strain rate $\dot{\gamma}^{\beta}$ and $\dot{g}^{\alpha}$, but the second term represents the effects of GND evolution rate on $\dot{g}^{\alpha}$. Therefore, both GND density and the rate of GND density evolution should be determined in Method II. Further, a minimization approach must be followed to determine the two tensors. Accordingly, the implementation of Method II is relatively more complicated and computationally costly compared to Method I. Here, the method originally developed by Abdolvand [58] was adopted to

calculate the curl of $\boldsymbol{F^p}$ which was subsequently implemented in the UMAT as described in [47].

The single crystal parameters used for HCP zirconium for each method are provided in Table 4.1. The single crystal parameters for method II model were calibrated using a comprehensive data set measured in a series of in-situ neutron diffraction experiments conducted on HCP zirconium polycrystals [59]. Measured macroscopic stress-strain curves, lattice strains, and texture development were used to calibrate the model parameters as explained in [47]. The model parameters for method I are calibrated such that they reproduce identical stress-strain curves to those from the model with method II. The initial SSD density is set at 10^{10} m^{-2} for both methods. The effects of twinning is ignored in the simulations since no twin was observed in the experiment. Here, only the single crystal parameters for the method I requires calibration. The process of calibration is discussed in section 4.4.1.

Table 4.1 Single crystal parameters used in the hardening law for HCP zirconium from Sedaghat and Abdolvand [47]

		Prism	Basal	Pyramidal
n		20	20	20
$\dot{\gamma}_0^\alpha\ (\boldsymbol{S^{-1}})$		3.5e-4	3.5e-4	1.0e-4
q^{ss} (self)		1	1	1
q^{st} (t=prism)		1	1	0
q^{st} (t=basal)		1	1	0
q^{st} (t=pyramidal)		0	0	1
Burgers vector (nm)		0.323	0.323	0.608
$H^\alpha\ (\boldsymbol{MPa\ \sqrt{m}})$		0.109	0.146	0.292
$g_{*,0}^\alpha\ (\boldsymbol{MPa})$		95	135	266
MI	K^α	0.07	0.07	0.30
	$y_c^\alpha\ (\boldsymbol{nm})$	5	5	10
MII	K^α	0.05	0.05	0.30
	$y_c^\alpha\ (\boldsymbol{nm})$	5	5	10

4.3.2 Input models

4.3.2.1 Single crystal

The evolution of GND and SSD densities as well as the CRSS of each slip system is studied using the single crystal model. This is to provide a comparison between the two methods used. A cube-shaped single crystal with the side length of 20 μm is used for the FE input model. The cube is deformed uniaxially to 5% applied strain at the strain rate of 10^{-5} s^{-1}. Uniaxial tensile strain is applied on the surface DCGH along the X-direction (Figure. 2a). Fixed displacement boundary conditions are applied on the ABFE, AEHD, and EFGH surfaces along X, Y, and Z directions, respectively. The model is discretized with 1000 quadratic brick elements with reduced integration points (C3D20R), with 10 elements in each direction. The c-axis of the HCP crystal was rotated with respect to the loading direction from 0° to 90° at the step size of 22.5°. As shown in Fig. 4.2a, the misorientation between the loading direction and crystal c-axis is presented by θ.

4.3.2.2 Polycrystal

The measured EBSD map shown in Fig. 4.1a is imported into the ABAQUS FE solver. The imported polycrystal model is shown in Fig. 4.2. The as measured strain and strain rates are applied to the FE model. The boundary conditions used are $u_x = 0$ and $u_y = 0$ on the ABCD and CGHD surfaces, respectively, and $u_z = 0$ on the AD and DH edges. The model is extruded in the z direction to the thickness of 50 μm to be consistent with the measured average grain size of the specimen. After conducting mesh sensitivity study to ensure that FE results are converged, the model was discretized to 65,157 C3D20R brick elements. Three elements along the model thickness are used. The EBSD measured grain orientations are assigned to each modeled grain. The model was deformed in two steps; in Step-1, 1.2% uniaxial strain was applied to the model in the global x-direction and in Step-2, the model is unloaded and allowed to relax. In all simulations presented,

the maximum time increment allowed is 5 seconds to ensure that the calculated GND densities are independent from the size of the selected time increment and are converged.
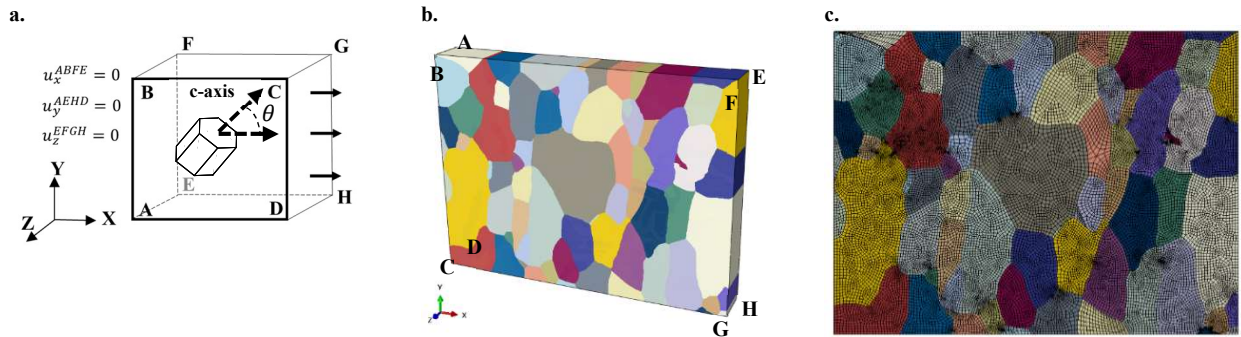
Figure 4.2 (a) Applied boundary conditions for the single crystal model. (b) The EBSD-measured microstructure imported into the finite element solver with the meshed map shown in (c).

4.4   Results

A single crystal model is firstly used to calibrate the single crystal parameters for the Method I of the CPFE model. This is followed by comparing the results of the CPFE models to those measured by HR-EBSD for stress, lattice rotations, and GND densities within the polycrystal. The capability of each method in determining slip activity and capturing slip bands is also discussed.

4.4.1   Single crystal

The single crystal model shown in Fig 2a is used to calibrate the single crystal parameters for the Method I of the CPFE model. The calculated stress of this method is compared to the one from Method II of the CPFE model. In addition, the calculated slip activities and GND densities are compared between the two methods. This is to understand the differences between each method at the single crystal level and to establish a foundation for the differences observed in the polycrystalline simulations.

In Fig. 4.3a, the stress-strain curves calculated with the CPFE model using both Methods I and II at five different crystal orientations are shown. In addition, the calculated relative activities of each slip system from both methods are provided in Fig. 4.3b. Relative activities are the resolved shear strain (γ^α) for each slip set divided by the total shear strain at the applied strain of 5%. It is shown that identical stress-strain curves and slip activities are obtained for different crystals orientations.

Fig. 4.3c compares the calculated relative GND density of each slip system from both methods of CPFE model. Relative GND densities are determined by dividing the total GND density calculated for each slip set to the total GND density calculated for all slip systems. The calculated relative GND densities from Method I follows the same trends captured for the slip activities. However, the relative GND densities of Method II follows a nearly horizontal line, which is independent from the misorientation angle θ and the calculated slip system activity. Moreover, the relative GND density of the pyramidal slip system is almost four times higher than those from prism and basal slip systems. The relative GND densities calculated for prism and basal slip systems from Method II are identical. These two curves are overlapped in Fig. 4.3c. The relative GND densities calculated using Method II for each slip set is proportional to the number of variants for each slip set. That is, GND densities are evenly distributed on all variants of a slip system when method II is used.
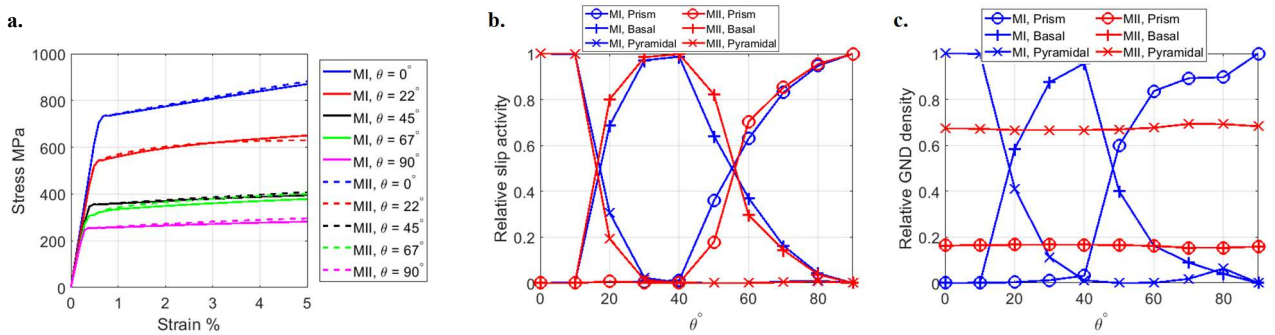
Figure 4.3 (a) The average stress-strain curve, (b) relative slip activity and (c) relative GND density calculated for a single crystal with different c-axis misorientation with the loading direction (θ). Comparisons are made for the Method I (M I) as well as Method II (M II) of the CPFE model.

The evolution of the average GND and SSD densities of each slip set from the two methods implemented in the CPFE framework is compared in Fig. 4.4. For each slip set, the total calculated dislocation density, either GND or SSD, is divided by the by the number of variants in the same slip set, i.e. M in $\frac{\sum_{\alpha=1}^{M} \rho_{GND}^{\alpha}}{M}$ is 3, 3, and 12 for prism, basal, and pyramidal slip systems, respectively. Results are for three different misorientation angles (θ). In addition, the calculated total dislocation densities, GNDs plus SSDs, from the two methods are compared. Although both methods predict identical average stress-strain curves (Fig. 4.3a), a significant difference in the predicted GND densities is observed. The SSD and GND densities from Method II have the same order of magnitude. However, in Method I, SSD densities are at least two orders of magnitude higher than GND densities. This means that the hardening of slip systems from Method I is mainly driven by SSD densities as the contribution of GND densities is almost negligible. The cumulative dislocation densities calculated from both SSDs and GNDs are almost equal to those calculated from Method II. This results in calculating the same evolution for CRSS using both methods.
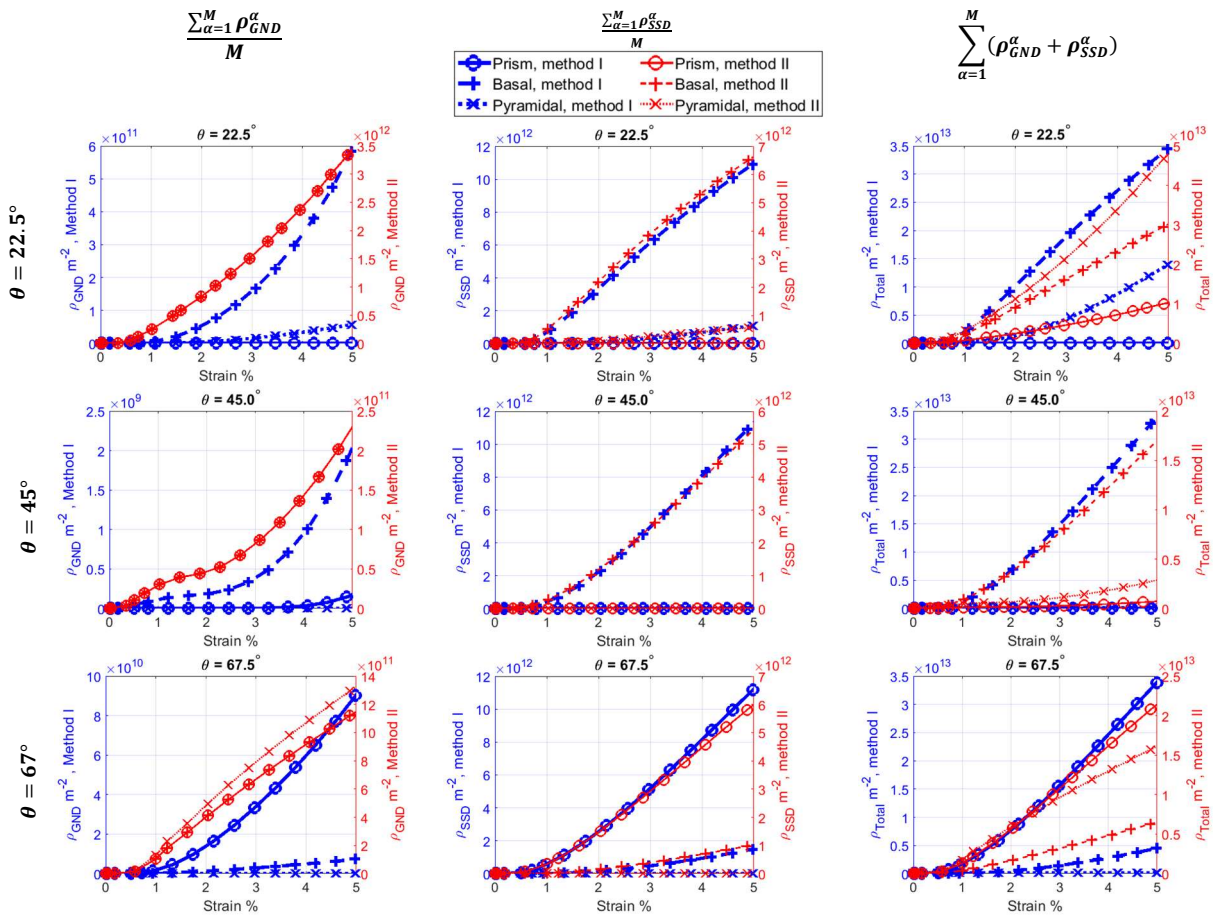
Figure 4.4 The evolution of the average GND density, average SSD density, and total dislocation density of prism, basal and pyramidal slip systems at different crystal c-axis misorientations with the loading direction (θ). Results are for CPFE model using Methods I and II. M is 3, 3, and 12 for prism, basal and pyramidal slip systems.

4.4.2　Polycrystal

Results presented in this section are from the CPFE model using both Methods I and II. The CPFE results for GND densities are presented and compared to those measured by

HR-EBSD. In addition, the capability of both methods in simulating formation of slip bands is evaluated by comparing the numerical results to those from SEM images of the deformed specimen. Finally, the distribution of calculated stresses and elastic lattice rotations are compared to those measured by HR-EBSD.

4.4.2.1 GND density and slip activity

The distributions of total GND densities after the unload step for Methods I and II are shown in Fig. 4.5a and 4.5b, respectively. The total GND density from Method I is about an order of magnitude smaller than that calculated using Method II. For example, in grains G2, G3, and G5, marked in Fig. 4.5a, a significant portion of the grains have GND densities lower than 10^9 m^{-2} when Method I is used. Moreover, the maximum GND density from Method I is about 4×10^{12} m^{-2}, but it is $\sim 7 \times 10^{14}$ m^{-2} when Method II is used. Although, there is a noticeable difference in the magnitudes of calculated GNDs, the predicted trends are quite similar between the two methods. For example, most of the grain boundaries have high GND densities. In addition, both methods predict highly localized GND concentration sites at the top-right sections of grains G1 and G2, upper side of grain G3, and right side of grain G6. These areas are shown by the white circles in Fig. 4.5a. HR-EBSD measurement also shows high GND density at these regions, as shown in Fig. 4.5c. However, the magnitudes of GND densities from HR-EBSD are higher than those from both CPFE methods, but much closer to those from Method II. In comparison to Method-I, the magnitude of GND densities from Method II is closer to those measured with HR-EBSD. This is not surprising because in the calculation of GND densities from HR-EBSD measurements, Method II is used along with L^1 optimization scheme. As a result, it is expected to have a better agreement between HR-EBSD measurements for GNDs and those from Method II of the CPFE model. The effects of using L^1 and L^2 optimization schemes in determining GND densities from HR-EBSD are

discussed elsewhere [60,61]. In addition, Method I cannot be used for HR-EBSD measurement as the plastic resolved shear strain on each slip system (γ^{α}) cannot be directly extracted with this technique (see Eq. 4-10).

Fig. 4.5d shows an ARGUS image of the deformed polycrystal, in which slip bands can be observed in most of the grains. For better visualization, the orientations of slip bands are shown with the black dotted lines. Interestingly, CPFE results from both Methods I and II also show GND density localization in the form of slip bands. For example, in grains G1, G2, G3, and G4, a distinct slip band is formed that spans from one side of the grain to another, as shown with the white dotted lines in Fig. 4.5b. The orientations of these bands are in agreement with those observed in the SEM image in Fig. 4.5d. In addition, both CPFE methods have captured the crossing of the two separate slip bands observed in grain G7. The two slip bands can also be observed in the ARGUS image. The CPFE results reveal that these slip bands are associated with the localization of plastic shear on the prism planes. This is also consistent with the measured grain orientations as shown in Fig. 4.5d. For example, in grains G2, G3, and G4, the observed slip bands of the ARGUS image are parallel to ones of the variants of the prism planes of the illustrated HCP crystals. Therefore, both Methods I and II are equally effective when predicting the direction of slip bands.
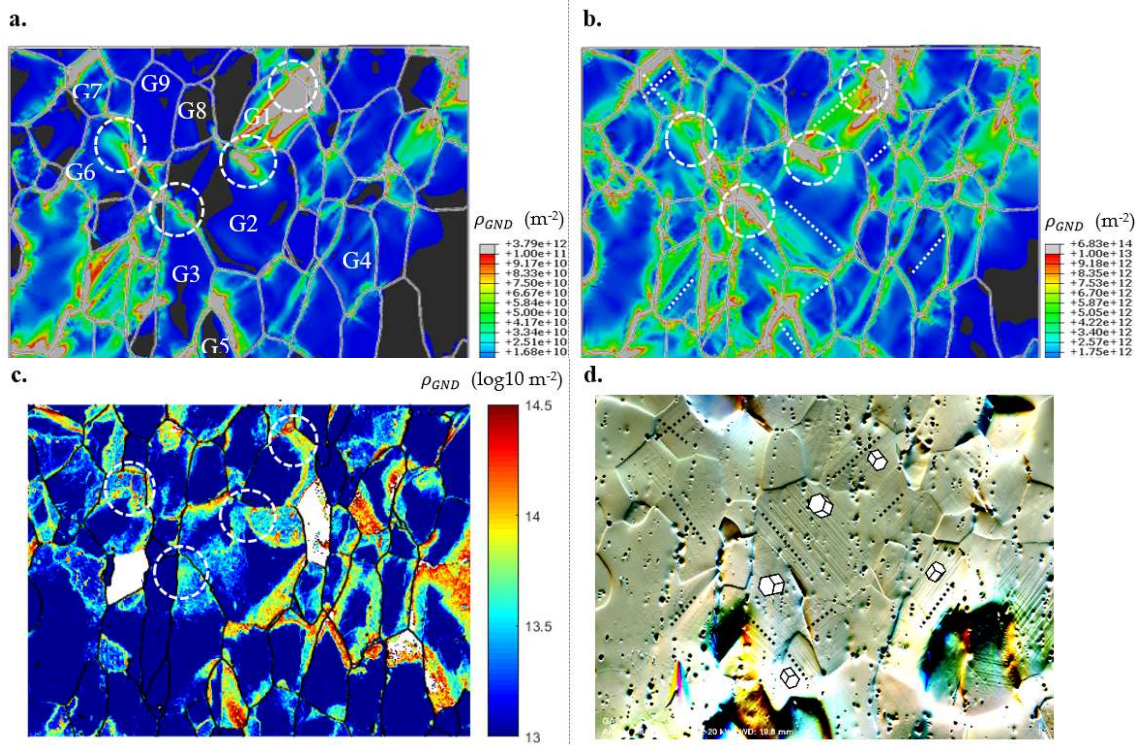
Figure 4.5 The distribution of total GND density from (a) CPFE model using Method I, (b) CPFE model using Method II and (c) HR-EBSD. (d) SEM-ARGUS image of the deformed sample. In (d) slip bands are shown with the black dashed lines and crystal orientations are shown using HCP crystals.

In order to determine the relationship between the observed slip bands and active slip systems, the average resolved shear strain and GND density of each slip set are extracted from the CPFE results and are shown in Table 4.2. These values are calculated by taking the volume average of the resolved shear strains, or GNDs, calculated at all integration points assigned to each grain. The calculated average value for each slip set is the summation over all variants, i.e. 3 variants for basal or prism, and 12 variants for pyramidal <c+a>. Table 4.2 summarizes the amount of slip and GND density

accumulated on the prism, basal, and pyramidal slip systems of grains G1 to G5. The predominant slip system with the highest value is presented in bold. Both methods confirm that the predominant slip system for all five selected grains is slip on the prism planes. For example, for grain G4 almost all plastic deformation is accommodated by prism slip systems whereas for grain G3 both basal and prism slip systems are active with prism being the most active one. Although these trends are also observed for the GND densities obtained from Method I, the pyramidal slip system accommodates most of the GNDs calculated in Method II. In fact, the GND density from method II is almost evenly distributed on all eighteen variants, but since the pyramidal slip system has 12 variants, it always has the highest GND density once the summation is done over all 12 variants. These results are consistent with the trends observed for the single crystal model. The heterogeneous distribution of the GND densities on the different slip variants in Method I is more reasonable compared to Method II where the GND densities on individual slip variants are always equal, regardless of the applied loading conditions.

Table 4.2 Average resolved shear strains and GND densities from the CPFE models. Results are for grains G1 to G5 of the polycrystalline model at 1.2 % applied strain. The predominant slip system is shown in bold.

Grain ID	GND Method	Cumulative resolved shear strain			GND density m^{-2}			
		Prism	Basal	Pyr	Prism	Basal	Pyr	Total
1	I	4.8×10^{-2}	3.6×10^{-3}	$<10^{-4}$	1.6×10^{11}	1.5×10^{9}	1.3×10^{6}	1.6×10^{11}
	II	4.4×10^{-2}	2.4×10^{-3}	$<10^{-4}$	3.8×10^{11}	3.8×10^{11}	2.1×10^{12}	2.9×10^{12}
2	I	2.4×10^{-2}	1.2×10^{-3}	$<10^{-4}$	3.7×10^{9}	1.4×10^{8}	4.1×10^{5}	3.9×10^{9}
	II	2.3×10^{-2}	1.1×10^{-3}	$<10^{-4}$	1.8×10^{11}	1.8×10^{11}	9.1×10^{11}	9.5×10^{11}
3	I	7.0×10^{-2}	3.2×10^{-2}	$<10^{-4}$	1.2×10^{10}	1.4×10^{10}	4.5×10^{6}	2.6×10^{10}
	II	6.9×10^{-2}	3.0×10^{-2}	$<10^{-4}$	1.9×10^{12}	1.9×10^{12}	8.8×10^{12}	1.3×10^{13}
4	I	1.1×10^{-1}	5.5×10^{-3}	$<10^{-4}$	7.7×10^{10}	5.1×10^{9}	9.2×10^{7}	8.2×10^{10}
	II	1.2×10^{-1}	5.3×10^{-3}	$<10^{-4}$	2.1×10^{12}	2.1×10^{12}	1.2×10^{13}	1.6×10^{13}
5	I	2.4×10^{-2}	1.2×10^{-3}	1.2×10^{-4}	2.6×10^{9}	1.2×10^{9}	4.5×10^{8}	4.3×10^{9}
	II	2.3×10^{-2}	0.9×10^{-3}	1.1×10^{-4}	4.2×10^{11}	4.2×10^{11}	2.5×10^{12}	3.3×10^{12}

Fig. 4.6 shows the distribution of resolved shear strains on the first and second most active slip variants. Results are for grains G2, G3, and G4. All variants are related to the slip on prism, except for the grain G3 where its second dominant variant belongs to the basal system (see Table 4.2). Shear strain localization in the form of slip bands is observed in all three grains. These slip bands are shown with a red dotted lines in Fig. 4.6. These bands are parallel to the ones observed in the GND maps in Fig. 4.5a and 4.5b as well as those observed in the ARGUS image of Fig. 4.5d.
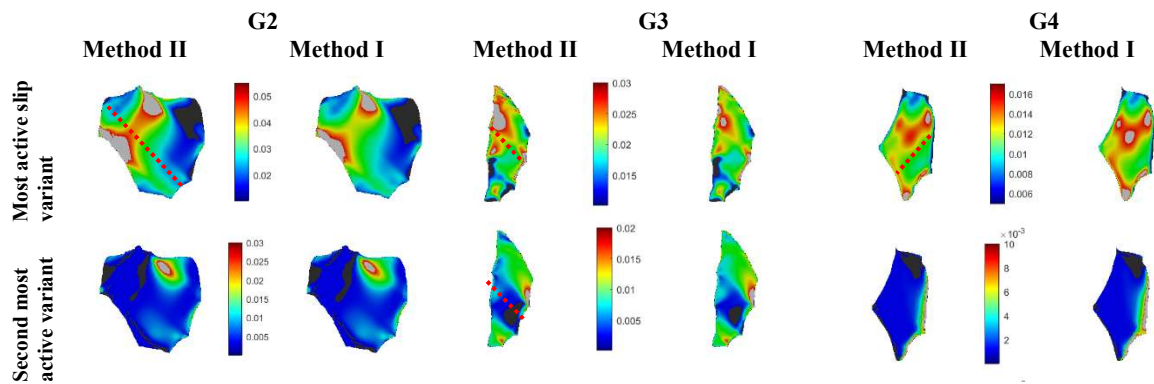
Figure 4.6 The distribution of resolved shear strain on the most active (first row) and the second most active (second row) slip systems. Results are for the CPFE model with Method I shown in the right column and Method II in left column. Grain IDs are shown on the top of each grain.

4.4.2.2 Stress

The normal stress component along the loading direction (σ_{11}) and the in-plane shear stress component (σ_{12}) of grains G3, G4, and G5 are shown in Fig. 4.7 and 4.8, respectively. The distribution of σ_{11} is almost identical between Methods I and II. After unloading, the normal stress drops significantly. The distributions of σ_{11} from HR-EBSD are also shown in the last row of Fig. 4.7. In an HR-EBSD measurement, a reference point is selected within each grain to measure "relative" stresses and elastic lattice

rotations with respect to this point. The reference point is normally selected far from the grain boundaries, where it is assumed that stress and orientation variations are minimum. These reference points are shown with the red dots in the Fig. 4.7. Since stresses from HR-EBSD are relative, the calculated stresses at all integration points assigned to a grain are reduced from those calculated at the integration point that coincides with the HR-EBSD reference point. This is to provide a like-to-like comparison between CPFE results and the HR-EBSD measurement.

For grain G2 of Fig. 4.7, a tensile stress field is predicted in the lower half of the grain where the stress magnitude increases toward the grain boundary. This is in agreement with HR-EBSD measurement. In addition, two compressive stress fields are observed in the upper half of the grain. In comparison to the measurement, the size of these two fields are overestimated in CPFE results, although the trends are the same. Grain G3 can be divided into three regions, i.e. top, bottom and middle regions. Calculated stress σ_{11} is tensile in the top and bottom regions, while it is compressive in the middle region. This is in agreement with the HR-EBSD measurement. For grain G4, the left side of the grain has a compressive stress field, and the bottom side of the grain has a tensile stress field in both model and experiment.
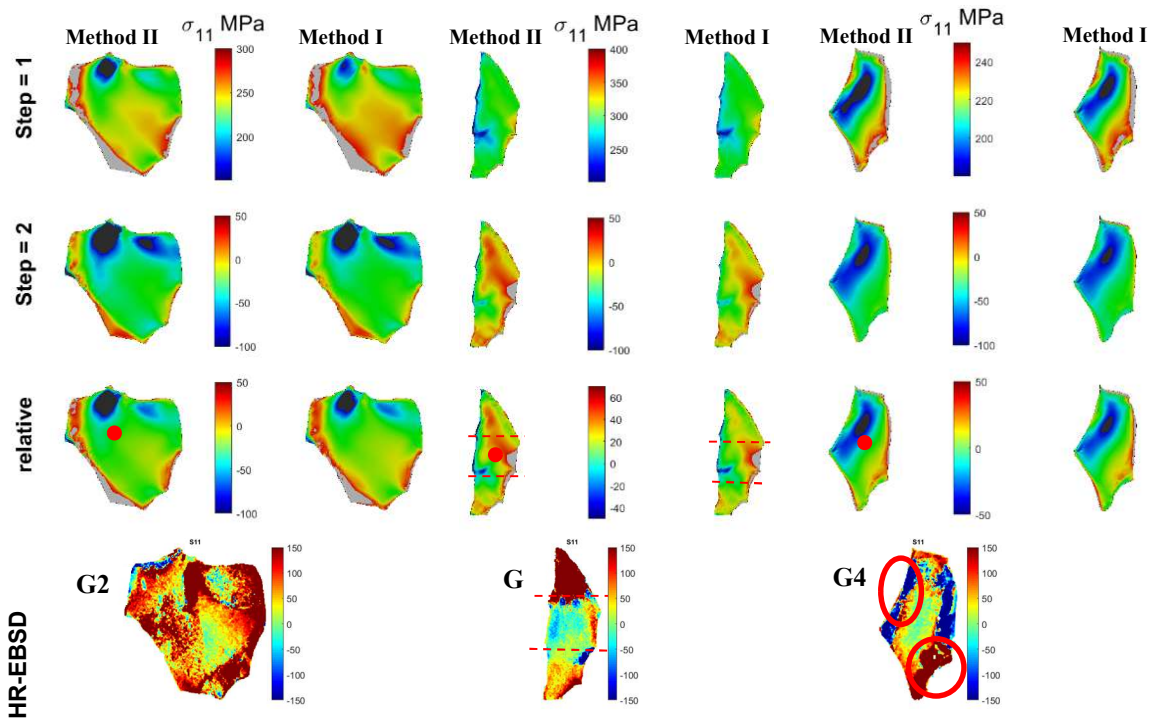
Figure 4.7 The normal stress component along the loading direction for grain G2, G3 and G4. A comparison between Method I (right column) and Method II (left column) of the CPFE model and HR-EBSD (last row).

In Fig. 4.8, it is shown that the distribution of shear stress σ_{12} is nearly identical between method I and II. For grain G2, a negative shear stress band is observed in the CPFE results on the top-left side of the grain. This band is also observed in the HR-EBSD measurement. In addition, a positive σ_{12} region, at the top-right side of the grain is calculated in both CPFE models which is also observed in the HR-EBSD measurement. However, there are regions in grains G3 and G4 where the calculated shear stress σ_{12} do not match with those from HR-EBSD measurement. The magnitude and distribution of calculated normal (Fig. 4.7) and shear stresses (Fig. 4.8) are quite similar between the two Methods I and II.
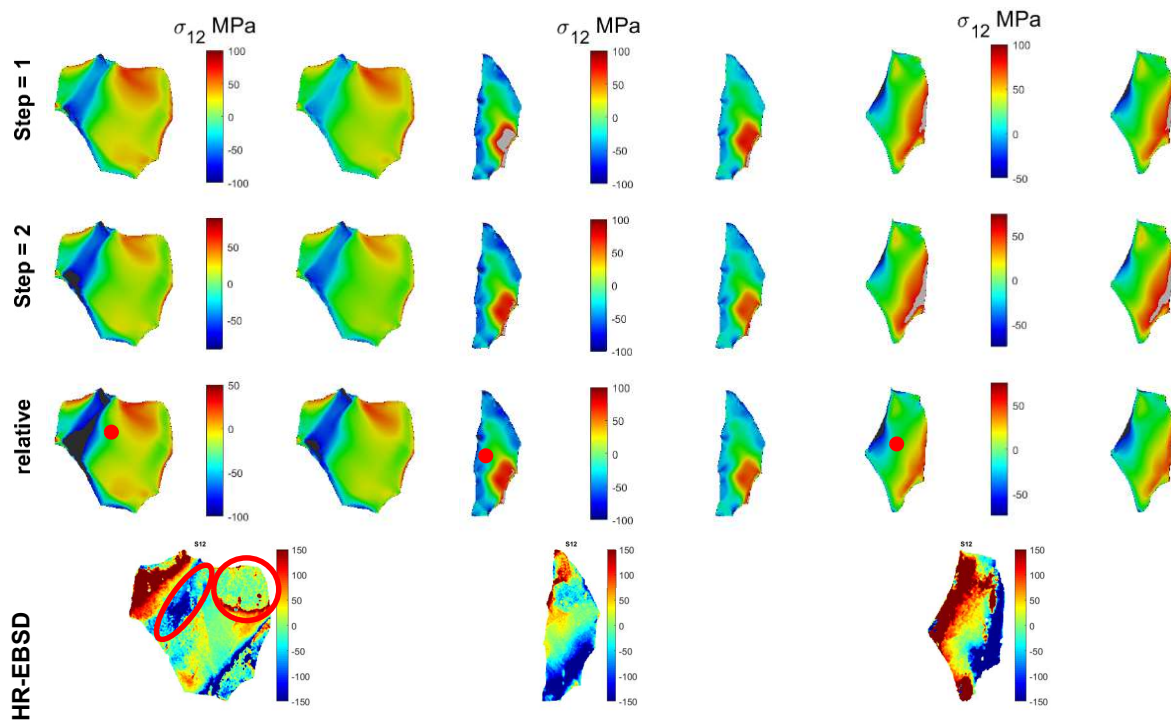
Figure 4.8 The in-plane shear stress component of grain G2, G3 and G4. A comparison between Method I (right column) and Method II (left column) of the CPFE model and HR-EBSD (last row)

4.4.2.3   Lattice rotations

The in-plane elastic rotation component of grains G2, G3, and G4 are shown in Fig. 4.9 and the results of Methods I and II are compared with those from HR-EBSD. Since measurements were done at the surface, only the in-plane component of the lattice rotation (ω_{12}^e) is shown. The relative values with respect to the reference point are presented in the last row of the simulation results. No difference is observed between the two methods in all the three grains after the loading and unloading steps. This means that although different GND densities are calculated in these two methods, the parameters are calibrated well, such that the resulting deformation tensors are almost identical from the

two methods. The relative values with respect to the reference point of the EBSD follow the same trend as the HR-EBSD measurement. For example, both CPFE and HR-EBSD results show positive elastic rotation ω_{12}^e in the left half of the grain G2. In addition, in both model and experiment, the top side of the grain G3 has negative elastic rotation ω_{12}^e. Furthermore, the CPFE results show negative ω_{12}^e on the top right side and positive ω_{12}^e on the lower left side of the grain G4 which agrees with the HR-EBSD measurement.
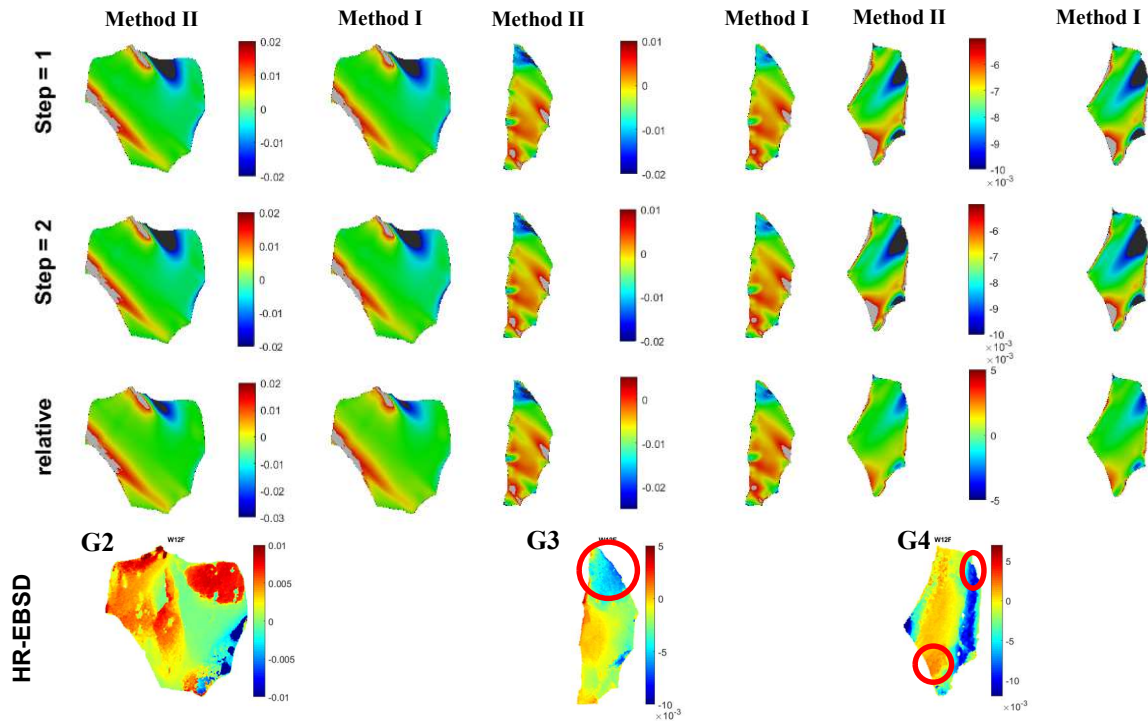
Figure 4.9 The elastic rotation component ω_{12}^e of grain G2, G3 and G4. A comparison between Method II (left column) and Method 1 (right column) of the CPFE model and HR-EBSD (last row). The lattice rotations are in radians.

4.5 Discussion

A lower-order strain-gradient crystal plasticity finite element model was developed in which two different methods were used to describe the evolution of GND densities. In Method I, a definite value was calculated for the magnitude of GNDs on each slip system, whereas in Method II, a minimization approach was used to solve for an under determined system of equations. The performance of CPFE models were examined both for single crystal models and for polycrystalline models. In addition, the as-measured microstructure of a deformed α-zirconium sample was imported to the FE solver to compare the calculated grain-scale stresses, elastic lattice rotations, and GNDs to those measured using HR-EBSD.

Results shown in all previous sections were for single or polycrystalline models with the average grain size more than 20 µm. The results of the strain-gradient CPFE model, however, are length-scale dependent and are highly sensitive to the size of the studied grains [47]. Such a size dependency originates from the accumulated GND density which is a function of plastic strain gradients. Since the magnitudes of GND densities from Methods I and II are very different, it is important to check the effects of grain size on the results obtained. To do so, the single crystal model used in section 4.3.1 is also used here, but the model is scaled so that different grain sizes can be studied. The model is scaled to ten different sizes from 0.125 µm to 64 µm and the calculated stresses, GND, and SSD densities from Methods I and II are compared. The misorientation between the c-axis of grain and the loading direction is set at 22.5º, 45º, and 67.5º. The macroscopic strain applied to the polycrystal is 5%. The Hall-Petch effects are switched off to only study the geometrical effects on the materials hardening.
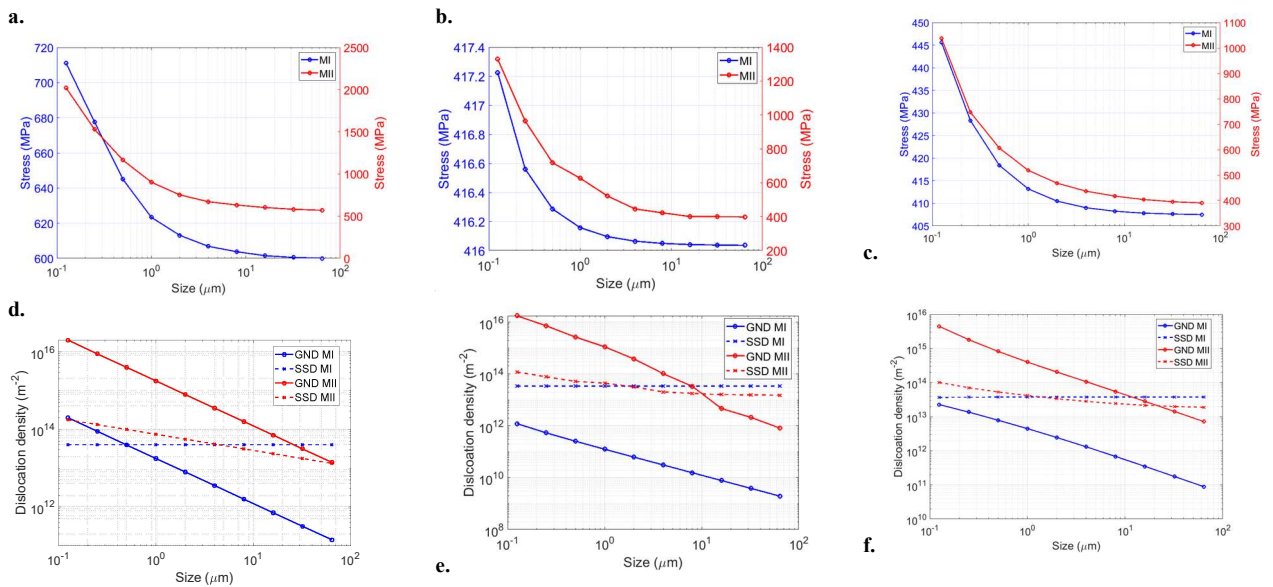
Figure 4.10 A comparison between the results of the CPFE model, using Methods I and II, for the single crystal model in Fig. 4.2a at ten different grain sizes. Stress along the loading direction for the misorientation angles of (a) 22.5º, (b) 45º, and (c) 67.5º. GND and SSD densities for the misorientation angles of (d) 22.5º, (e) 45º, and (f) 67.5º. The values on the x-axis represent the size of the single crystal. Hall-Petch effects are switched off.

Figs 10a, 10b, and 10c show that the average stress for the single crystal with misorientation angle of 22.5º, 45º, 67.5º, respectively. It is shown that the stress magnitude is highly affected by the model size when Method II is used, particularly when the grain size is smaller than 10 μm. Although Method I also shows some dependency on the grain size, the magnitude of the stress is only significantly affected by the grain size for the grains smaller than 1 μm. This is the reason why the stresses obtained from the two methods for the polycrystal, presented in section 4.2.2 with the average grain size of 50 μm, are not that different. Figs 10d, 10e, and 10f show that the average GND and SSD density for the single crystal with misorientation angle of 22.5º, 45º, 67.5º, respectively.

It is shown that the calculated GND density has a linear relation with the grain size in the log-log scale. Interestingly, the slops of these two lines are the same for the two methods used. In contrast to GNDs, SSDs are almost unaffected by the grain size. Therefore, the hardening of bigger grains is SSD driven, while that of smaller grains is GND driven. This means that SSDs are as much important in determining stress development. Hence, when the formulation provided here is used to study fracture of polycrystals at grain scale [31,32], it is very important to fully characterize the contribution of both GNDs and SSDs to material plastic deformation.

A lower-order strain-gradient crystal plasticity model is used here, where the material hardening law is modified by including the strain gradient terms. One of the disadvantages of this approach is the formation of unrealistic localized deformation fields as described in [16]. Further, when lower-order formulation is used, CPFE results are mesh-size dependent; on the other hand, when higher-order formulation is used, CPFE results are almost mesh independent [62].

The simulation results obtained from CPFE models showed several discrepancies with respect to those from HR-EBSD. The observed discrepancies could be due to ignoring the sub-surface grain structures in the CPFE results. As shown in Fig. 4.2, a columnar grain structure was assumed in the CPFE model by extruding the measured EBSD map along the z-axis. This is because the EBSD measurement does provide the information about the sub-surface grains. Although, ignoring the sub-surface grain structures may affect the stress values at the free surface in the CPFE results [63–65], Zhang et al. showed that the calculated trends in the GND densities and strains are not much affected by the sub-surface microstructure [48].

Table 4.3 summarizes the results of the comparisons made between Method I and II. The effectiveness of the two methods can be assessed using two different perspectives:

implementation and performance. From the implementation point of view, Method I is more straightforward and can be used for developing higher-order non-local CPFE models. This method is also computationally efficient since no optimization is required to determine the density of GNDs. In terms of performance, the use of Method II leads to closer numbers to those measured with HR-EBSD for GND density but results in uniform distribution of GNDs on all slip variants. Finally, when larger grain sizes are used, typically more than 10 μm, there is no difference between the two methods.

Table 4.3 A comparison between Method I and II for determining GND densities

Implementation	Lower order non-local CPFE	Both methods can be implemented, but the implementation of Method I is more straightforward than Method II
	Higher order non-local CPFE	Only Method I
Performance	Total GND density	Results from Method II are closer to those measured with HR-EBSD.
	GND density on each slip system	Method I: The calculated values are proportional to the cumulative slip for each slip variant Method II: almost equal for all slip systems

4.6 Conclusions

A user material (UMAT) subroutine is updated to include the strain-gradient effects. Two different methods are used for determining GND densities. The performance of the two methods for simulating the formation of slip bands in a deformed α-zirconium specimen is investigated. Numerical results are compared with those measured with HR-EBSD. It is shown that:

1. The GND maps calculated from the strain-gradient CPFE models using both methods show formation of localized GND lines within the grains of the

polycrystalline model. These GND lines are parallel to the slip bands observed in the deformed specimen using electron microscopy. The slip bands can also be seen in the calculated shear strain maps of the CPFE results.

2. The use of the minimization-based approach for the determination of GND densities (Method II) leads to an even distribution of GNDs on all slip systems, whereas when the direct approach (Method I) is used, the magnitude of the calculated GNDs on each slip system is proportional to the plastic shear strain accumulated on the same slip system.

3. Although the magnitudes of GND densities are different from the two methods, the trends observed for the calculated grain-scale stresses and lattice rotations are the same for the polycrystal. This is because for the studied microstructure, where the average grain size is 50 μm, the calculated total dislocation density, GND plus SSD, from the two methods is almost the same.

4. When a smaller grain size is used, the calculated average stresses from the two methods are different. The critical grain size below which the geometrical effects become significant is higher in Method II, compared to Method I.

5. The dislocation-based hardening law used here is SSD driven for larger grains and GND driven for smaller grains and accurate implementation of both mechanisms is important when different grain sizes exist in the microstructure.

References

[1]   A. Rovinelli, H. Proudhon, R.A. Lebensohn, M.D. Sangid, Assessing the reliability of fast Fourier transform-based crystal plasticity simulations of a polycrystalline material near a crack tip, Int. J. Solids Struct. 184 (2020) 153–166. https://doi.org/10.1016/j.ijsolstr.2019.02.024.

[2]   M.P. Petkov, J. Hu, E. Tarleton, A.C.F. Cocks, Comparison of self-consistent and crystal plasticity FE approaches for modelling the high-temperature deformation of 316H austenitic stainless steel, Int. J. Solids Struct. 171 (2019) 54–80. https://doi.org/10.1016/j.ijsolstr.2019.05.006.

[3]   R. Ma, T.J. Truster, S.B. Puplampu, D. Penumadu, Investigating mechanical degradation due to fire exposure of aluminum alloy 5083 using crystal plasticity finite element method, Int. J. Solids Struct. 134 (2018) 151–160. https://doi.org/10.1016/j.ijsolstr.2017.10.021.

[4]   X. Lu, X. Zhang, M. Shi, F. Roters, G. Kang, Dislocation mechanism based size-dependent crystal plasticity modeling and simulation of gradient nano-grained copper, Int. J. Plast. 113 (2019) 52–73. https://doi.org/10.1016/j.ijplas.2018.09.007.

[5]   F. Han, F. Roters, D. Raabe, Microstructure-based multiscale modeling of large strain plastic deformation by coupling a full-field crystal plasticity-spectral solver with an implicit finite element solver, Int. J. Plast. 125 (2020) 97–117. https://doi.org/https://doi.org/10.1016/j.ijplas.2019.09.004.

[6]   M. Kasemer, P. Dawson, A finite element methodology to incorporate kinematic activation of discrete deformation twins in a crystal plasticity framework, Comput. Methods Appl. Mech. Eng. 358 (2020) 1–29. https://doi.org/10.1016/j.cma.2019.112653.

[7]   J. Wijnen, R.H.J. Peerlings, J.P.M. Hoefnagels, M.G.D. Geers, A discrete slip plane model for simulating heterogeneous plastic deformation in single crystals, Int. J. Solids Struct. 228 (2021) 111094. https://doi.org/10.1016/j.ijsolstr.2021.111094.

[8]   S. Nemat-nasser, L. Ni, T. Okinaka, A constitutive model for fcc crystals with application to polycrystalline OFHC copper, Mech. Mater. 30 (1998) 325–341.

[9] U.F. Kocks, A.S. Argon, M.F. Ashby, Thermodynamics and kinetics of slip, Pergamon Press, 1975.

[10] L.P. Evers, W. a M. Brekelmans, M.G.D. Geers, Non-local crystal plasticity model with intrinsic SSD and GND effects, J. Mech. Phys. Solids. 52 (2004) 2379–2401. https://doi.org/10.1016/j.jmps.2004.03.007.

[11] M.F. Ashby, The deformation of plastically non-homogeneous materials, Philos. Mag. 21 (1970) 399–424. https://doi.org/10.1080/14786437008238426.

[12] G.I. Taylor, The Mechanism of Plastic Deformation of Crystals. Part1. Theoretical, Proceeding R. Soc. 538 (1934) 362–387.

[13] A. Arsenlis, D.M. Parks, Modeling the evolution of crystallographic dislocation density in crystal plasticity, J. Mech. Phys. Solids. 50 (2002) 1979–2009.

[14] A. Arsenlis, D.M. Parks, R. Becker, V. V Bulatov, On the evolution of crystallographic dislocation density in non-homogeneously deforming crystals, J. Mech. Phys. Solids. 52 (2004) 1213–1246. https://doi.org/10.1016/j.jmps.2003.12.007.

[15] M.E. Gurtin, A gradient theory of single-crystal viscoplasticity that accounts for geometrically necessary dislocations, J. Mech. Phys. Solids. 50 (2002) 5–32. https://doi.org/10.1016/S0022-5096(01)00104-1.

[16] C.F. Niordson, J.W. Hutchinson, On lower order strain gradient plasticity theories, Eur. J. Mech. A/Solids. 22 (2003) 771–778. https://doi.org/10.1016/S0997-7538(03)00069-X.

[17] J.L. Bassani, Incompatibility and a simple gradient theory of plasticity, J. Mech. Phys. Solids. 49 (2001) 1983–1996. https://doi.org/10.1016/S0022-5096(01)00037-0.

[18] E.P. Busso, F.T. Meissonnier, N.P.O. Dowd, Gradient-dependent deformation of two-phase single crystals, J. Mech. Phys. Solids. 48 (2000) 2333–2361.

[19] A. Arsenlis, D.M. parks, Crystallographic aspects of geometrically nesesary and statistically stored dislocation density, Acta Mater. 47 (1999) 1597–1611.

[20] R. De Borst, H. -B Mühlhaus, Gradient-dependent plasticity: Formulation and algorithmic aspects, Int. J. Numer. Methods Eng. 35 (1992) 521–539.

https://doi.org/10.1002/nme.1620350307.

[21] H. Gao, Y. Huang, W.D. Nix, J.W. Hutchinson, Mechanism-based strain gradient plasticity - I. Theory, J. Mech. Phys. Solids. 47 (1999) 1239–1263. https://doi.org/10.1016/S0022-5096(98)00103-3.

[22] G. Yun, K.C. Hwang, Y. Huang, P.D. Wu, A reformulation of mechanism-based strain gradient plasticity, Philos. Mag. 85 (2005) 4011–4029. https://doi.org/10.1080/14786430500363338.

[23] M.E. Gurtin, On the plasticity of single crystals: Free energy, microforces, plastic-strain gradients, J. Mech. Phys. Solids. 48 (2000) 989–1036. https://doi.org/10.1016/S0022-5096(99)00059-9.

[24] J.. Nye, Some geometrical relations in dislocated crystals, Acta Metall. 1 (1953) 153–162. https://doi.org/10.1016/0001-6160(53)90054-6.

[25] S. Das, F. Hofmann, E. Tarleton, Consistent determination of geometrically necessary dislocation density from simulations and experiments, Int. J. Plast. 109 (2018) 18–42. https://doi.org/10.1016/j.ijplas.2018.05.001.

[26] H. Dai, Geometrically-necessary dislocation density in continuum plasticity theory, FEM Implement. Appl. (1997).

[27] A. Ma, F. Roters, D. Raabe, A dislocation density based constitutive model for crystal plasticity FEM including geometrically necessary dislocations, Acta Mater. 54 (2006) 2169–2179. https://doi.org/10.1016/j.actamat.2006.01.005.

[28] F.P.E. Dunne, D. Rugg, A. Walker, Lengthscale-dependent, elastically anisotropic, physically-based hcp crystal plasticity: Application to cold-dwell fatigue in Ti alloys, Int. J. Plast. 23 (2007) 1061–1083. https://doi.org/10.1016/j.ijplas.2006.10.013.

[29] S. Waheed, Z. Zheng, D.S. Balint, F.P.E. Dunne, Microstructural effects on strain rate and dwell sensitivity in dual-phase titanium alloys, Acta Mater. 162 (2019) 136–148. https://doi.org/10.1016/j.actamat.2018.09.035.

[30] A. Arsenlis, Modeling dislocation density evolution in continuum crystal plasticity, n.d. http://dspace.mit.edu/handle/1721.1/36679%5Cnhttps://dspace.mit.edu/handle/1721.1/36679.

[31] B. Chen, K. Jansenss, F.P.E. Dunne, Role of geometrically necessary dislocation density in multiaxial and non-proportional fatigue crack nucleation, Int. J. Fatigue. 135 (2020) 105517. https://doi.org/10.1016/j.ijfatigue.2020.105517.

[32] D. Wilson, F.P.E. Dunne, A mechanistic modelling methodology for microstructure-sensitive fatigue crack growth, J. Mech. Phys. Solids. 124 (2019) 827–848. https://doi.org/10.1016/j.jmps.2018.11.023.

[33] F.P.E. Dunne, R. Kiwanuka, A.J. Wilkinson, Crystal plasticity analysis of micro-deformation , lattice rotation and geometrically necessary dislocation density, Proc. R. Soc. A Math. Phys. Eng. Sci. (2012). https://doi.org/10.1098/rspa.2012.0050.

[34] J. Cheng, S. Ghosh, A crystal plasticity FE model for deformation with twin nucleation in magnesium alloys, Int. J. Plast. 67 (2015) 148–170. https://doi.org/10.1016/j.ijplas.2014.10.005.

[35] W. Wu, K. An, L. Huang, S.Y. Lee, P.K. Liaw, Deformation dynamics study of a wrought magnesium alloy by real-time in situ neutron diffraction, Scr. Mater. 69 (2013) 358–361. https://doi.org/10.1016/j.scriptamat.2013.05.008.

[36] F. Xu, R. a. Holt, M.R. Daymond, R.B. Rogge, E.C. Oliver, Development of internal strains in textured Zircaloy-2 during uni-axial deformation, Mater. Sci. Eng. A. 488 (2008) 172–185. https://doi.org/10.1016/j.msea.2007.11.018.

[37] K. Louca, H. Abdolvand, Accurate determination of grain properties using three-dimensional synchrotron X-ray diffraction: A comparison with EBSD, Mater. Charact. (2021) 1–2. https://doi.org/https://doi.org/10.1016/j.matchar.2020.110753.

[38] H. Abdolvand, K. Louca, C. Mareau, M. Majkut, J. Wright, On the nucleation of deformation twins at the early stages of plasticity, Acta Mater. 196 (2020) 733–746. https://doi.org/10.1016/j.actamat.2020.07.010.

[39] H. Abdolvand, J.P. Wright, A.J. Wilkinson, On the state of deformation in a polycrystalline material in three-dimension: Elastic strains, lattice rotations, and deformation mechanisms, Int. J. Plast. 106 (2018) 145–163. https://doi.org/10.1016/j.ijplas.2018.03.006.

[40] D. Wallis, A.J. Parsons, L.N. Hansen, Quantifying geometrically necessary dislocations in quartz using HR-EBSD: Application to chessboard subgrain

boundaries, J. Struct. Geol. 125 (2019) 235–247. https://doi.org/10.1016/j.jsg.2017.12.012.

[41] T. Ungar, M. Drakopoulos, J.L. Be, T. Chauveau, O. Castelnau, G. Riba, A. Snigirev, I. Snigireva, C. Schroer, B. Bacroix, Grain to grain slip activity in plastically deformed Zr determined by X-ray micro-diffraction line profile analysis, Acta Mater. 55 (2007) 1117–1127. https://doi.org/10.1016/j.actamat.2006.09.031.

[42] A.J. Wilkinson, G. Meaden, D.J. Dingley, High-resolution elastic strain measurement from electron backscatter diffraction patterns: New levels of sensitivity, Ultramicroscopy. 106 (2006) 307–313. https://doi.org/10.1016/j.ultramic.2005.10.001.

[43] A.J. Wilkinson, Measurement of elastic strains and small lattice rotations using electron back scatter diffraction, Ultramicroscopy. 62 (1996) 237–247. https://doi.org/10.1016/0304-3991(95)00152-2.

[44] K.Z. Troost, P. Van Der Sluis, D.J. Gravesteijn, Microscale elastic-strain determination by backscatter Kikuchi diffraction in the scanning electron microscope, Appl. Phys. Lett. 62 (1993) 1110–1112. https://doi.org/10.1063/1.108758.

[45] Y. Guo, H. Abdolvand, T.B. Britton, A.J. Wilkinson, Growth of $\{11\bar{2}2\}$ twins in titanium: A combined experimental and modelling investigation of the local state of deformation, Acta Mater. 126 (2017) 221–235. https://doi.org/10.1016/j.actamat.2016.12.066.

[46] T.B. Britton, a. J. Wilkinson, High resolution electron backscatter diffraction measurements of elastic strain variations in the presence of larger lattice rotations, Ultramicroscopy. 114 (2012) 82–95. https://doi.org/10.1016/j.ultramic.2012.01.004.

[47] O. Sedaghat, H. Abdolvand, A non-local crystal plasticity constitutive model for hexagonal close-packed polycrystals, Int. J. Plast. 136 (2021) 102883. https://doi.org/10.1016/j.ijplas.2020.102883.

[48] Z. Zhang, D. Lunt, H. Abdolvand, A.J. Wilkinson, M. Preuss, F.P.E. Dunne, Quantitative investigation of micro slip and localization in polycrystalline materials under uniaxial tension, Int. J. Plast. 108 (2018) 88–106.

https://doi.org/10.1016/j.ijplas.2018.04.014.

[49] F.P.E. Dunne, R. Kiwanuka, A.J. Wilkinson, Crystal plasticity analysis of micro-deformation, lattice rotation and geometrically necessary dislocation density, Proc. R. Soc. A Math. Phys. Eng. Sci. 468 (2012) 2509–2531. https://doi.org/10.1098/rspa.2012.0050.

[50] H. Abdolvand, O. Sedaghat, Y. Guo, Nucleation and growth of twins in titanium: Elastic energy and stress fields at the vicinity of twins, Materialia. 2 (2018) 58–62. https://doi.org/10.1016/j.mtla.2018.06.012.

[51] H. Abdolvand, J. Wright, A.J. Wilkinson, Strong grain neighbour effects in polycrystals, Nat. Commun. 9 (2018) 171. https://doi.org/10.1038/s41467-017-02213-9.

[52] H. Abdolvand, A.J. Wilkinson, On the effects of reorientation and shear transfer during twin formation: Comparison between high resolution electron backscatter diffraction experiments and a crystal plasticity finite element model, Int. J. Plast. 84 (2016) 160–182. https://doi.org/10.1016/j.ijplas.2016.05.006.

[53] R.J. Asaro, A. Needleman, Overview No. 42 Texture developement and strain hardening in rate dependant polycrystals, Acta Metall. 33 (1985) 923–953.

[54] R.J. Asaro, Crystal Plasticity, J. Appl. Mech. 50 (1983) 921–934.

[55] E.S. Fisher, C.J. Renken, Single-crystal elastic moduli and the hcp $\rightarrow$ bcc transformation in Ti, Zr, and Hf, Phys. Rev. 135 (1964). https://doi.org/10.1103/PhysRev.135.A482.

[56] I.J. Beyerlein, C.N. Tomé, A dislocation-based constitutive law for pure Zr including temperature effects, Int. J. Plast. 24 (2008) 867–895. https://doi.org/10.1016/j.ijplas.2007.07.017.

[57] K.S. Cheong, E.P. Busso, A. Arsenlis, A study of microstructural length scale effects on the behaviour of FCC polycrystals using strain gradient concepts, Int. J. Plast. 21 (2005) 1797–1814. https://doi.org/10.1016/j.ijplas.2004.11.001.

[58] H. Abdolvand, Progressive modelling and experimentation of hydrogen diffusion and precipitation in anisotropic polycrystals, Int. J. Plast. 116 (2019) 39–61. https://doi.org/10.1016/j.ijplas.2018.12.005.

[59] H. Abdolvand, M.R. Daymond, C. Mareau, Incorporation of twinning into a crystal plasticity finite element model: Evolution of lattice strains and texture in Zircaloy-2, Int. J. Plast. 27 (2011) 1721–1738. https://doi.org/10.1016/j.ijplas.2011.04.005.

[60] D. Wallis, L.N. Hansen, T.B. Britton, A.J. Wilkinson, High-Angular Resolution Electron Backscatter Diffraction as a New Tool for Mapping Lattice Distortion in Geological Minerals, J. Geophys. Res. Solid Earth. 124 (2019) 6337–6358. https://doi.org/10.1029/2019JB017867.

[61] D. Wallis, L.N. Hansen, T. Ben Britton, A.J. Wilkinson, Geometrically necessary dislocation densities in olivine obtained using high-angular resolution electron backscatter diffraction, Ultramicroscopy. 168 (2016) 34–45. https://doi.org/10.1016/j.ultramic.2016.06.002.

[62] M. Kuroda, V. Tvergaard, Studies of scale dependent crystal viscoplasticity models, J. Mech. Phys. Solids. 54 (2006) 1789–1810. https://doi.org/10.1016/j.jmps.2006.04.002.

[63] P. Baudoin, T. Hama, H. Takuda, Influence of critical resolved shear stress ratios on the response of a commercially pure titanium oligocrystal: Crystal plasticity simulations and experiment, Int. J. Plast. 115 (2019) 111–131. https://doi.org/10.1016/j.ijplas.2018.11.013.

[64] A. Zeghadi, S. Forest, A.F. Gourgues, O. Bouaziz, Ensemble averaging stress-strain fields in polycrystalline aggregates with a constrained surface microstructure-part 2: Crystal plasticity, Philos. Mag. 87 (2007) 1425–1446. https://doi.org/10.1080/14786430601009517.

[65] L. St-Pierre, E. Héripré, M. Dexet, J. Crépin, G. Bertolino, N. Bilger, 3D simulations of microstructure and comparison with experimental microstructure coming from O.I.M analysis, Int. J. Plast. 24 (2008) 1516–1532. https://doi.org/10.1016/j.ijplas.2007.10.004.

Chapter 5

5 Dislocation-based crystal plasticity finite element modeling of irradiation growth in α-zirconium

A mechanistic model for simulating irradiation growth strain in zirconium alloys is integrated into a non-local crystal plasticity finite element model. The results of the model are firstly compared to the previously published measurements of growth strain in both annealed single crystals and annealed as well as cold worked polycrystalline α-zirconium specimens irradiated with neutrons. This is followed by conducting a sensitivity analysis to characterize the evolution of average growth strain in polycrystals as a function of average grain size, texture, and prior cold work. The distributions of growth strain within and across the grains of the polycrystals are critically analyzed. It is shown that due to the heterogeneous distribution of the dislocation line densities at the grain level, a noticeable non-uniformity in growth strain is observed. In addition, it is shown that growth strain can be localized at grain boundaries. The magnitude of the localized growth strain significantly depends on the grain size, the magnitude of prior cold work, and irradiation dose.

5.1 Introduction

In nuclear reactors, zirconium alloys are exposed to an intensive neutron flux from fission reactions. During irradiation, neutrons pass through zirconium cladding and knock atoms off from their regular positions in the lattice towards interstitial sites and leave vacancies behind. This phenomenon, also known as irradiation damage, results in the formation of two different types of dislocation loops in hexagonal closed-pack (HCP) zirconium crystals: interstitial loops and vacancy loops [1–4]. Formation of the interstitial and vacancy loops is accompanied by expansion and contraction of HCP crystals along the

crystal a-axis and c-axis, respectively. This anisotropic, but volume conserving dimensional change that takes place in the absence of an external load is known as irradiation growth. For the safe and efficient operation of a nuclear reactor, it is important to assure that the core components subjected to irradiation have dimensional stability over the effective lifetime of the reactor. This study focuses on the development of a mechanistic model for understanding and simulating the effects of irradiation growth at the grain and macroscopic scales.

The effects of irradiation damage on the deformation mechanisms of zirconium alloys have been experimentally studied over the last decades. A review of such effects can be found in [5]. Irradiation growth strain is affected by neutrons fluence and energy, the operating temperature of the reactor, as well as zirconium's composition, texture, prior cold work, and average grain size. For example, it was shown that irradiation growth in annealed polycrystalline zirconium is generally about ten times greater than that of single crystals [6]. This study showed that grain boundaries are strong sinks for irradiation-induced defects. In another study by Fidleris [7], it was shown that irradiation growth is inversely dependent on grain size in annealed polycrystalline zirconium. Murgatroyd and Rogerson [8] also observed a significant grain size dependence, with specimens having 5 μm grains exhibiting a higher strain than those with 40 μm grains. However, Cann et al. [9] showed that growth strain may not be affected by grain size for specimens with grain sizes bigger than 50 μm. Prior cold work can also have a significant influence on the growth strain of zirconium. An experimental study by Rogerson showed that cold-worked specimens with smaller grain sizes have significantly higher growth strain compared to annealed ones with bigger grain sizes [6]. It was also shown that with cold working zirconium and increasing stored dislocation density, irradiation growth strain increases [10,11].

In addition to the macro-scale experimental measurements, several micro-scale investigations have been conducted on irradiated samples. For example, Griffith et al. [12] analysed the dislocation loops sponge and crystal-bar zirconium, neutron irradiated to a fluence of 4.5×10^{25} nm^{-2} and 1.6×10^{26} nm^{-2}, respectively, using transmission electron microscopy (TEM). It was shown that while the mid-grain region contains equal number of vacancy and interstitial loops, the regions adjacent to the grain boundary contains only vacancy loops. Furthermore, cavities (vacancy clusters) were found close to the grain boundaries, but not in the mid-grain regions. Recently, an in-situ TEM study on electron irradiated magnesium was conducted by Dong et al. [13]. It was shown that dislocation loops preferentially nucleate and grow only in 10-200 nm from grain boundaries. Therefore, the presence of grain boundaries was seen to locally accelerate the formation of dislocation loops. In another study by Zhang et al. [14], dislocation loops were analysed in an ion irradiated nano layered Zr-2.5Nb specimen using TEM. A dislocation loop denuded zone was found close to the beta-phase, within the alpha phase. The width of this defect free zone was measured to be 30-40 nm, and it was shown to decrease with decreasing the size of the alpha phase. Although these TEM measurements have been conducted to study the distribution of dislocation loops within grains, there is a lack of information on the distribution of the resulting growth strain at the grain level. Modeling techniques can be helpful for such investigations. In addition, numerical models may be used for predicting the long-term effects of irradiation damage on the core components of next generation nuclear reactors.

There are two general approaches for modeling irradiation growth in the literature: empirical and mechanistic. Empirical models mainly use measured data for curve fitting of the model parameters. For determining irradiation growth strain, several empirical models have been proposed [15–17]. Although these models account for texture, irradiation dose, and temperature effects, they are mainly valid for the range of the test

conditions used for model calibration. While being simple and fast, these empirical models neglect the interaction between crystallographic texture, grain morphologies, and irradiation damage at the grain scale. Another approach for simulating the effects of irradiation damage is to use physically-based mechanistic models. Molecular dynamics (MD) and dislocation dynamics (DD) are the two nanoscale approaches used to understand the interaction between dislocations with point defects, as well as to calculate their densities or distributions during irradiation cascades [18–24]. Such atomistic simulations provide crucial insight towards understanding the nature of the interaction between point defects and line defects or how dislocations climb. However, there is a need for linking the nanoscale simulations to macroscale models. This is to ensure that the time scale used in modeling is representative of the process, and the effects of materials texture and microstructure are included by studying the response of many grains.

Crystal plasticity is a class of constitutive equations that can be used to study the heterogeneous deformation of individual or cluster of grains. It is a mesoscale modeling approach where plastic strain is calculated by determining the amount of slip that occurs on all active slip systems within individual grains of the polycrystal [25–27]. Crystal plasticity has been implemented in different frameworks, e.g., self-consistent [28,29], fast Fourier transform (CP-FFT) [30,31], and finite element (CPFE) [32–34]. In the self-consistent framework, each grain interacts with a homogenous medium that represents the average properties of the aggregate except for the grain that is investigated. The limitation of this framework is that it cannot capture the "true" interaction among neighboring grains. Unlike the self-consistent framework, local stress variations, stress concentration within individual grains, and the effects of the local neighborhood on the response of each grain can be studied using FE and FFT frameworks [35–41].

The mechanistic irradiation growth models have primarily been developed based on a rate-theory approach [19,42–45]. The reader is referred to the reference [5] for a comprehensive review of the various physically-based irradiation growth models. For example, a reaction-diffusion model for irradiation growth of HCP materials was proposed by Golubov et al. [45]. In this model, the evolution of vacancy and interstitial loops follows a dose-dependent formulation, leading to a dose-dependent irradiation growth strain model for single crystal HCP zirconium. This model was implemented in a self-consistent crystal plasticity framework to study the evolution of grain-average irradiation growth strain [46]. It was shown that the effects of texture and grain size on the calculated growth strain are significant. However, the possible effects of the local grain neighborhood were ignored. In addition, the distribution of growth strain between and within grains was not studied. Such studies can be conducted in dislocation-based CPFE models.

In this chapter, the irradiation growth model of Golubov et al. [45] is adopted to integrate into a dislocation-based CPFE model. The results of the new model are compared to those measured for both single crystals as well as polycrystals, either annealed or cold worked. In addition, the effects of texture, prior cold work, and average grain size on the average irradiation growth strain of polycrystal are investigated. The distribution of the growth strain between different grains and within individual grains is subsequently analyzed using both polycrystal and bi-crystal models. Finally, the role of grain boundary sink strength on the formation of localized irradiation growth strain and the effects of irradiation hardening on the numerical results are discussed.

5.2 Model

The constitutive equations used for crystal plasticity and irradiation growth models are described in this section. These equations are implemented into a user material (UMAT) subroutine developed by Sedaghat and Abdolvand [47].

5.2.1   Crystal plasticity constitutive equations

A brief description of the key equations of the CPFE model is provided here, a comprehensive explanation is given elsewhere [47]. The code is a UMAT subroutine that calculates the stress increment, the material Jacobian matrix, and updates solution dependent state variables (SDVs) based on a given strain, rotation, and time increment. For a given strain increment we have:

$$\Delta \boldsymbol{\varepsilon} = \Delta \boldsymbol{\varepsilon}^{el} + \Delta \boldsymbol{\varepsilon}^{pl} + \Delta \boldsymbol{\varepsilon}^{gr} \qquad (5\text{-}1)$$

where $\Delta \boldsymbol{\varepsilon}$ is the total strain increment given by the FE solver, $\Delta \boldsymbol{\varepsilon}^{el}$ is the elastic strain increment, $\Delta \boldsymbol{\varepsilon}^{pl}$ is the plastic strain increment as a result of slip, and $\Delta \boldsymbol{\varepsilon}^{gr}$ is the irradiation growth strain. In this chapter, tensors are presented using a bold font, and vectors are identified with an arrow on the top. Strain rates are firstly calculated and then time integrated to calculate the increments. The rate of the plastic strain ($\dot{\boldsymbol{\varepsilon}}^{p}$) or the plastic part of the deformation rate ($\boldsymbol{D}^{p}$) can be calculated using the following equation:

$$\dot{\boldsymbol{\varepsilon}}^{p} = \boldsymbol{D}^{p} = \sum_{\alpha=1}^{N} \boldsymbol{P}^{\alpha} \dot{\gamma}^{\alpha} \qquad (5\text{-}2)$$

$$\boldsymbol{P}^{\alpha} = sym(\boldsymbol{S}^{\alpha}) \; where \; \boldsymbol{S}^{\alpha} = \vec{m}^{\alpha} \otimes \vec{n}^{\alpha}$$

in which $\boldsymbol{P}^{\alpha}$ is the symmetric part of the Schmid tensor for the slip system α, and $\dot{\gamma}^{\alpha}$ is the shear rate on the same slip system. $\vec{m}^{\alpha}$ and $\vec{n}^{\alpha}$ are the slip direction and normal of the

slip system α, respectively. A rate-dependent equation is used to calculate the shear rate on the slip system α, based on the resolved shear stress (τ^α) that acts on the same slip system [48]:

$$\dot{\gamma}^\alpha = \dot{\gamma}_0^\alpha \operatorname{sign}\left(\frac{\tau^\alpha}{g^\alpha}\right) \left|\frac{\tau^\alpha}{g^\alpha}\right|^n \tag{5-3}$$

where $\dot{\gamma}_0$ is a reference shear strain rate, n represents the sensitivity of the material to a strain rate and g^α is the critical resolved shear stress (CRSS) of the slip system α. The resolved shear stress acting on the slip system α is proportional to Kirchhoff stress ($\boldsymbol{\psi}$) through the following equation [49]:

$$\tau^\alpha = \boldsymbol{P}^\alpha : \boldsymbol{\psi} \tag{5-4}$$

The Jaumann rate of the Kirchhoff stress tensor ($\boldsymbol{\breve{\psi}}$) is related to the elastic part of the deformation rate tensor ($\boldsymbol{D}^e$) and the elastic stiffness tensor ($\mathbb{C}$) of the HCP crystal after rotation to the deformed configuration as:

$$\boldsymbol{\breve{\psi}} = \mathbb{C} : \boldsymbol{D}^e \tag{5-5}$$

The elastic modulus of zirconium single crystal used in this study is the one determined by Fisher and Renken [50]: C_{11}=143.5 GPa, C_{33}=164.9 GPa, C_{12}=72.5 GPa, C_{13}=65.4 GPa, and C_{44}=32.1 GPa. The objective rate of Kirchhoff stress, in Eq. (5-5), is defined with respect to an observer attached to the crystal lattice:

$$\boldsymbol{\breve{\psi}} = \dot{\boldsymbol{\psi}} - \boldsymbol{\Omega}^e \boldsymbol{\psi} + \boldsymbol{\psi} \boldsymbol{\Omega}^e \tag{5-6}$$

where $\boldsymbol{\Omega}^e$ is the elastic part of the spin tensor and is calculated by subtracting the provided total spin tensor and the calculated plastic spin [47]. The strength of each slip system (α) follows a dislocation-based hardening law [29,51–54]:

$$g^\alpha = g^\alpha_{*,0} + \frac{H^\alpha}{\sqrt{D}} + \xi G b^\alpha \sqrt{\sum_{\beta=1}^{N} q^{\alpha\beta} \left(\rho^\beta_{GND} + \rho^\beta_{SSD} \right)} \tag{5-7}$$
$$+ z^\alpha_{loop} G b^\alpha \sqrt{\rho^\alpha_{loop}}$$

where g^α is the current strength of the slip system α, $g^\alpha_{*,0}$ is the CRSS, D is the equivalent grain diameter, H^α is the Hall-Petch parameter, ξ is a material constant, G is the shear modulus, b^α is the size of the Burgers vector for the slip system α, ρ^β_{GND} and ρ^β_{SSD} are the geometrically necessary dislocation (GND) and statistically stored dislocation (SSD) densities on the slip system β, z^α_{loop} is the irradiation hardening parameter for each slip system, and ρ^α_{loop} is the dislocation loop density on the slip system α. z^α_{loop} is assumed to be 0.80, 0.55, and 0.40 on the prism and basal, and pyramidal slip systems [29]. A hardening matrix $q^{\alpha\beta}$ is introduced to consider the effects of self and latent-hardening. It is assumed that the GND and SSD densities have the same hardening matrix $q^{\alpha\beta}$. The shear modulus, G in Eq. (5-7), is assumed to be the average value of C_{44}, C_{55}, and C_{66} [55]. The material constant ξ is assumed to be 0.5.

At the early stages of plasticity, dislocations are mainly generated but with further loading, dislocation density will be high enough such that dislocations with opposite signs are annihilated. Here, it is assumed that the evolution of SSD densities follows the equation below [53,56]:

$$\dot\rho^\alpha_{SSD} = \frac{|\dot\gamma^\alpha|}{b^\alpha} \left(K^\alpha \sqrt{\rho^\alpha_{SSD} + \rho^\alpha_{GND}} - 2 y^\alpha_c \, \rho^\alpha_{SSD} \right) \tag{5-8}$$

where K^α is the dislocation accumulation constant and y_c^α is the dislocation annihilation length of the slip system α. The first term on the right-hand side of the Eq. (5-8) is the dominant term at the early stages of plasticity, while with further loading, the effects of the second term will be non-negligible. The density of GNDs on the slip system α is determined using the following equation [57]:

$$\left(curl\left(\mathbf{F}^{p^T}\right)\right)^T = \sum_{\alpha=1}^{N}\left(\rho_{GND,s}^{\alpha}\ \vec{b}^{\alpha}\otimes\vec{m}^{\alpha} + \rho_{GND,et}^{\alpha}\ \vec{b}^{\alpha}\otimes\vec{t}^{\alpha} + \rho_{GND,en}^{\alpha}\ \vec{b}^{\alpha}\otimes\vec{n}^{\alpha}\right) \tag{5-9}$$

ρ_{GND}^{α} for each slip system can be decomposed into three components, one for screw type dislocation $\rho_{GND,s}^{\alpha}$ with the dislocation line vector along the slip direction, m^{α}, and two edge types dislocations, $\rho_{GND,en}^{\alpha}$ and $\rho_{GND,et}^{\alpha}$ with dislocation line vectors along the slip normal and $t^{\alpha} = m^{\alpha}\times n^{\alpha}$, respectively. This method has infinite solutions where a minimization scheme is usually used to find a solution. One solution can be obtained by minimizing the sum of the squares of GND densities [58]:

$$\{\rho_{GND}^{\alpha}\} = A^T(AA^T)^{-1}B \tag{5-10}$$

where $\{\rho_{GND}^{\alpha}\}$ is 3N×1 column vector containing edge and screw components of GND for slip system α, B is a 9×1 vector, containing the components of the tensor in the left-hand side of Eq. (5-9), and A is a 9×3N matrix containing the basis tensors of the right-hand side of Eq. (5-9). The method developed by Abdolvand [33] was adopted to calculate the curl of $\mathbf{F}^p$ which was subsequently implemented in the UMAT as described in [47].

5.2.2   Irradiation growth model

The irradiation growth model developed by Golubov et al. [45] is used and briefly described in this section. The model assumptions can be summarized as follows. The

primary defects generated during neutron irradiation are interstitial and vacancy point defects, moving in 3D, and interstitial clusters, moving along the prismatic directions on the basal plane of the HCP crystal [59]. It is assumed that the concentrations of these defects have reached the steady state condition. Interstitial loops are only formed on the prismatic planes, while vacancy loops are formed on both prismatic and basal planes. The rate of irradiation growth strain can be written as [60,61]:

$$
\dot{\varepsilon}_j^{gr} = \begin{cases} \rho_j(D_iC_i - D_vC_v) + K_{GB}(D_iC_i - D_vC_v) + \text{n}D_{cl}C_{cl}K_{cl}^2 \ ; \quad j = a \\ \rho_j(D_iC_i - D_vC_v) + K_{GB}(D_iC_i - D_vC_v) \qquad ; \qquad j = c \end{cases}
\tag{5-11}
$$

where j is the direction of the growth strain in the local coordinate system of the HCP crystal, which is either along the a-axis or c-axis. D_i and D_v are the diffusivity of interstitial and vacancy point defects, C_i and C_v are the concentration of the interstitial and vacancy point defects, D_{cl} and C_{cl} are the diffusivity and concentration of the interstitial clusters, K_{cl}^2 is the sink strength of the interstitial clusters, and K_{GB} is the sink strength of the grain boundary. ρ_j is the total dislocation density including dislocation line density (ρ_d^j) and dislocation loop density of both interstitial and vacancy types:

$$
\rho_j = \rho_d^j + 2\pi r_i^j N_i^j + 2\pi r_v^j N_v^j
\tag{5-12}
$$

where N_i^j and N_v^j are interstitial and vacancy loop number density, r_i^j is interstitial loop radius, and r_v^j is vacancy loop radius. In the absence of twinning, plastic deformation in α-zirconium is generally controlled by 18 slip systems, i.e. three prism, three basal, and twelve pyramidal <c+a> slip systems. The dislocation line density on each slip variant is the sum of the SSD and GND densities from Eq. (5-8) and Eq. (5-10). The calculated dislocation line density on each slip variant is transformed into the local crystal coordinate system to be used in Eq. (5-12). The dislocation line densities of basal and

prismatic slip systems are calculated along the crystal a-axis. However, the dislocations along the pyramidal slip systems have both a-type and c-type components. Therefore, they are projected along the crystal a-axis and c-axis, following the procedure explained in [46]. That is, the angle between the pyramidal Burgers vector and the basal plane normal ($\theta \approx 30°$) is used. The dislocation line density on each pyramidal slip variant is multiplied by $\cos^2(\theta)$ and $\sin^2(\theta)$, respectively, to determine the projected components along the crystal c-axis and a-axis. This is to conserve the net dislocation density. Finally, the calculated dislocation densities along the three a-axis directions are averaged, assuming a uniform distribution of the dislocation densities along the prismatic directions.

The sink strength of dislocations for absorbing interstitial clusters is given as:

$$K_{cl}^2 = 2 \left(\frac{2}{\pi} \rho_a \, r_{cd} \right)^2 \tag{5-13}$$

where r_{cd} is the capture radius of dislocations for interstitial clusters. The sink strength of grain boundaries (K_{GB}) is calculated only for the elements located at the grain boundaries following [62]:

$$K_{GB} = \begin{cases} z_{GB}\rho_{GB} \; ; & \text{grain boundary elements} \\ 0 \; \; ; & \text{grain interior elements} \end{cases} \tag{5-14-1}$$

$$z_{GB} = 4\pi a \left(\frac{ka \cosh(ka) - \sinh(ka)}{\sinh(ka) - ka} \right) \tag{5-14-2}$$

$$\rho_{GB} = \frac{3}{4\pi a^3}, \quad k = \sqrt{\rho} \tag{5-14-3}$$

where a is the grain size, k is the square root of the total dislocation density on all slip systems, ρ_{GB} is the grain boundary density, and z_{GB} is the sink strength for a given grain boundary. K_{GB} is only calculated for the grain boundary elements and is set to zero for other elements.

The net flux of the point defects and interstitial clusters absorbed by dislocations and grain boundaries (Eq.5-11) are determined using the reaction-diffusion equations of the point defects [44,45,60]:

$$\frac{dC_v}{dt} = G(1 - f_c) - D_v C_v (\rho + K_{GB}) \tag{5-15-1}$$

$$\frac{dC_i}{dt} = G(1 - f_c)(1 - f_i^{cl}) - D_i C_i (\rho + K_{GB}) \tag{5-15-2}$$

$$\frac{dC_{cl}}{dt} = G(1 - f_c)\frac{f_i^{cl}}{3n} - D_{cl} C_{cl} K_{cl}^2 \tag{5-15-3}$$

where G is the defect production rate, ρ is the total density of dislocation lines and dislocation loops on all the slip systems, f_c is the fraction of the point defects that are recombined and varies between 0.9 to 0.97 [46,61], and f_i^{cl} is the fraction of the interstitial point defects which are clustered. Since we are assuming steady state condition, the left-hand side of Eq. (5-15) is zero. Therefore, the multiplication of the defects diffusivity and concentration is determined as a function of the total dislocation density (ρ) and grain boundary sink strength (K_{GB}). By knowing the radius and number density of dislocation loops, irradiation growth strain in Eq. (5-11) can be determined. Two sets of equations are required to determine the evolution of the loop number density and the loop size. It is assumed that loop number density saturates after a certain amount of irradiation. While the loop density along the a-axis is linearly proportional to

irradiation dose, the one along the c-axis initiates after a specific amount of irradiation [44,45]:

$$
N_{v,i}^a = \begin{cases} N_{v,i}^{a,max} \dfrac{\varphi}{\varphi_{v,i}^{max}} & ; \varphi \leq \varphi_{v,i}^{a,max} \\ N_{v,i}^{a,max} & ; \varphi > \varphi_{v,i}^{a,max} \end{cases}
$$

(5-16-1)

$$
N_v^c = \begin{cases} 0 & ; \quad \varphi < \varphi_{v0}^c \\ N_v^{c,max} \dfrac{\exp\left[A \dfrac{\varphi - \varphi_{v0}^c}{\varphi_{v0}^{c,max} - \varphi_{v0}^c}\right] - 1}{\exp(A) - 1} & ; \varphi_{v0}^c \leq \varphi < \varphi_v^{c,max} \\ N_v^{c,max} & ; \quad \varphi \geq \varphi_v^{c,max} \end{cases}
$$

(5-16-2)

where $\varphi_{v,i}^{a,max}$ is the irradiation dose at the end of the nucleation stage of the prismatic loops, $N_{v,i}^{a,max}$ is the maximum density of prismatic loops, φ_{v0}^c is the irradiation dose at the start of the nucleation of basal loops, and $\varphi_{v0}^{c,max}$ is the irradiation dose at the end of the nucleation of basal loops. $N_v^{c,max}$ is the maximum density of basal loops, and A is a dimensionless parameter.

In order to find the radius of dislocation loops, a mean size approximation approach is used in which the mean values of radii for vacancy and interstitial loops are found via the relationship between the total number of defects in the loops of any particular type (*S*) and the loop number densities [44,45]:

$$S_v^a = \pi (r_v^a)^2 b_a N_v^a$$

(5-17-1)

$$S_i^a = \pi (r_i^a)^2 b_a N_i^a$$

(5-17-2)

$$S_v^c = \pi (r_v^c)^2 b_c N_v^c$$

(5-17-3)

The total number of defects (S) in the loops change with time according to the following equations [44,45]:

$$\dot{S}_v^a = 2\pi r_v^a N_v^a (D_v C_v - D_i C_i) - k_v^2 n\, D_{cl}\, C_{cl} \tag{5-18-1}$$

$$\dot{S}_i^a = 2\pi r_i^a N_i^a (D_v C_v - D_i C_i) + k_i^2 n\, D_{cl}\, C_{cl} \tag{5-18-2}$$

$$\dot{S}_v^c = 2\pi r_v^c N_v^c (D_v C_v - D_i C_i) \tag{5-18-3}$$

Where k_v^2 and k_i^2 are the sink strengths of vacancy and interstitial loops for interstitial clusters, given by:

$$k_v^2 = 2\pi^2\, r_{cvl} r_v^a N_v^a \left(\frac{\pi r_{cd}}{2} \rho_d^a + \pi^2 r_{cvl} r_v^a N_v^a + \pi^2 r_{cil} r_i^a N_i^a \right) \tag{5-19-1}$$

$$k_i^2 = 2\pi^2\, r_{cil} r_i^a N_i^a \left(\frac{\pi r_{cd}}{2} \rho_d^a + \pi^2 r_{cvl} r_v^a N_v^a + \pi^2 r_{cil} r_i^a N_i^a \right) \tag{5-19-2}$$

where r_{cvl} and r_{cil} are the capture radii of vacancy and interstitial type prismatic loops for clusters.

5.2.3   Numerical implementation and model parameters

The UMAT developed by Sedaghat and Abdolvand [47] is updated to include the irradiation growth effects using Eqs. 11-19. The subroutine developed by Golubov et al. [45] is adopted and used for this purpose. This subroutine is modified by reading the dislocation line densities (GND and SSD) calculated in the UMAT at each time increment. Table 5.1 shows the flowchart of the model. At the beginning of each time increment, Abaqus FE solver provides the total strain increment, rotation increment, deformation gradient, and solution dependent state variables (SDVs). $\boldsymbol{F}^p$ of the last time increment is restored in a common block and used to evaluate $curl(\boldsymbol{F}^{p^T})$ and GND

densities using Eq. (5-9)-(5-10). Please note that $\boldsymbol{F}^p$ only represents the plastic deformation by slip. The Newton-Raphson method is used to calculate the increments of plastic shear strain for each slip system ($\Delta\gamma^\alpha$), and update the density of SSDs, stress, and the material Jacobean matrix. Finally, $\boldsymbol{F}^p$ is updated and stored in a common block variable for the next time increment.

Table 5.1 Flow chart of the non-local CPFE model

(1) Abaqus FE solver provides total strain increment, rotation increment, and deformation gradient for the time increment *i,* as well as stress ($\boldsymbol{\sigma}^{i-1}$) and state variables ($SDVs^{i-1}$) for time increment i-1.
(2) If the irradiation step is running, calculate the irradiation growth strain using Eq. (5-11)-(5-19) in the crystal coordinate system. Rotate this growth strain increment to the global coordinate system.
(3) Calculate $curl\left(\boldsymbol{F}^{p^T}\right)$ and ρ_{GND} using Eq. (5-9)-(5-10)
(4) Using Eqs. (5-2)–(5-7) calculate elastic and plastic strain increments ($\Delta t\boldsymbol{D}^e$, $\Delta t\boldsymbol{D}^p$) using the Newton-Raphson method until shear strain increments ($\Delta\gamma^\alpha$) is converged.
(5) Update the $SDVs^i$ (τ^α, g^α, γ^α, n^α, m^α), ρ_{SSD}^i, stress ($\boldsymbol{\sigma}^i$) and material Jacobean matrix
(6) Evaluate $\boldsymbol{F}^{p,i}$ from Eqs. (5-2) and store in a common bock variable for the next time increment.

Crystal plasticity parameters for the slip systems of Zircaloy-2 are provided in Table 5.2. The single parameters were calibrated using neutron diffraction data for the same material [47]. For simplicity, the effects of deformation twinning are ignored in this study but are discussed in section 5.4. The irradiation growth parameters are provided in Table 5.3 and are taken from [44].

Table 5.2 The single crystal parameters used in the CPFE model [47]

	Prism	Basal	Pyramidal
N	20	20	20
$\dot{\gamma}_0^{\alpha}\ (S^{-1})$	3.5e-4	3.5e-4	1.0e-4
q^{ss} (self)	1	1	1
q^{st} (t=prism)	1	1	0
q^{st} (t=basal)	1	1	0
q^{st} (t=pyramidal)	0	0	1
Burgers vector (nm)	0.323	0.323	0.608
$H^{\alpha}\ (MPa\ \sqrt{m})$	0.109	0.146	0.292
$g_{*,0}^{\alpha}\ (MPa)$	95	135	266
K^{α}	0.05	0.05	0.30
$y_c^{\alpha}\ (nm)$	5	5	10

Table 5.3 Irradiation growth model parameters [44]

Symbol	Value	description
$\varphi_{v,i}^{a,max}$ (dpa)	3.84	Irradiation dose at the end of the nucleation stage for the prismatic loops
$N_{v,i}^{a,\ max}\ (m^{-3})$	10^{22}	The maximum density of prismatic loops
φ_{v0}^{c} (dpa)	3	Irradiation dose at the start of the nucleation stages for the basal loops
$\varphi_{v}^{c,max}$ (dpa)	23	Irradiation dose at the end of the nucleation stages for the basal loops
$N_{v}^{c,max}(m^{-3})$	10^{21}	The maximum density of basal loops
A	5	Dimensionless parameter
$r_{cvl},r_{cil}\ (nm)$	0.6	Capture radii of sessile vacancy/ interstitial type prismatic loops
$r_{cd}\ (nm)$	0.6	Capture radii of dislocations for interstitial clusters
f_{cl}^{i}	0.2	Fraction of the interstitial point defects which are clustered

5.3 Results

The irradiation-CPFE model is verified in this section by comparing the numerical results for the evolution of the irradiation growth strain to those measured experimentally. Results from both single crystal and polycrystals are compared. The single crystal specimen is annealed, while the polycrystal specimens are both annealed and cold worked. In addition, a sensitivity analysis using the irradiation-CPFE model is conducted to study the effects of texture, prior cold work, and grain size on the magnitude of the growth strain in polycrystalline zirconium specimens. Finally, the distribution of the growth strain within and across the grains of the polycrystalline model is analysed. It

should be noted that the grain boundary sink strength (K_{GB}) and the irradiation hardening term of Eq. (5-7) are switched off in this section. However, their effects on the numerical results are discussed in section 5.4.

5.3.1　Single crystal

The evolution of growth strain from the irradiation-CPFE model is compared to the measured one for an annealed single crystal Zircaloy-2 specimen irradiated at 553 K with neutrons of 1 MeV energy [63]. This specimen was prepared using electron beam zone melting from a 6 mm diameter rod. The measured strain is along the a-axis of the crystal, where it is expanded. The crystal was irradiated up to 2×10^{25} n/m^2, equivalent to ~7 dpa. A cubic single crystal with a side length of 20 mm is used for the FE input model. The applied boundary conditions are shown in Fig. 5.1a. The displacement on the ABFE, AEHD, and EFGH surfaces are fixed along X, Y, and Z directions, respectively, but other surfaces are free to move. The model is discretized with 1000 brick elements (C3D20R), with 10 elements in each direction. The initial dislocation density on each slip system and f_c parameter are set to 10^{12} m^{-2} and 0.9, respectively. These values are chosen to be consistent with the single crystal model parameters used in [44,45]. The single crystal model is irradiated in one step, without any prior deformation or any external load. The irradiation dose rate is set to 10^{-7} dpa/s with a total step time of 8×10^7 s resulting in 8 dpa irradiation damage.

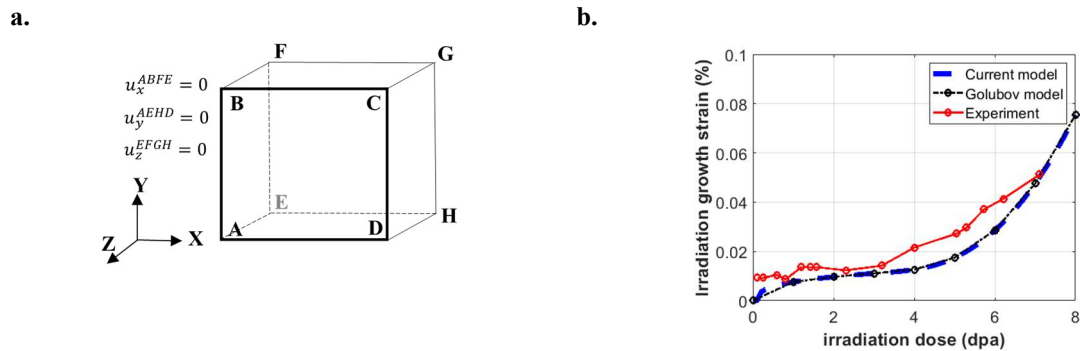a.   b.

Figure 5.1 (a) Applied boundary conditions for the single crystal model. (b) A comparison between the results of the current irradiation-CPFE model, the model by Golubov et al. [45], and the experiment by Carpenter et al. [63] for the irradiation growth strain along the a-axis of single crystal zirconium

Fig. 5.1b compares the evolution of the irradiation growth strain along the a-axis of the single crystal. Results are for the current irradiation growth enhanced CPFE model, the model by Golubov et al. [45], and the experiment by Carpenter et al. [63]. The single crystal expands along the a-axis in both models and in the experiment. Results from the developed CPFE model perfectly match with those from Golubov et al. [45]. Both numerical models can replicate the evolution of measured strain. For example, experimental results show that the slope of growth strain increases after ~4 dpa, a trend observed in the irradiation-CPFE model. In addition, both model and experimental results show that after 7 dpa of neutron irradiation, almost 0.05% of growth strain develops along the crystal a-axis.

5.3.2   Polycrystal: average response

The measured growth strain for Zircaloy-2 polycrystals from [6] are studied and compared to model calculations. The two sets of experimental data used here are summarised in Table 5.4. The first set, called A1, is for an annealed specimen with an

average grain size of 20 μm. The second set is for 25% cold worked specimen with average grain sizes of 8 μm for the A2 specimen. All experiments were conducted at 553 K. The measured textures of the specimens were reported using Kearns factor, which represents the average volume fraction of basal poles in the longitudinal (F_L), transverse (F_T), and radial (F_R) directions. These values for the two specimens are shown in Table 5.4. The growth strains were measured in the longitudinal direction of the tubes.

Two FE input models were prepared to represent specimens A1 and A2. Each model has the same average grain size and Kearns factors as the ones reported in the corresponding specimen. Both models have 1038 grains discretized with 125,000 brick elements (C3D20R) as shown in Fig. 5.3a. The orientations of grains, however, are different for each input model. The basal pole figures of the FE models for A1 and A2 are shown in Figs. 2a and 2b, respectively. The calculated values of F_L, F_T, and F_R for each reconstructed model are provided in Table 5.4. As shown in Fig. 5.3a, displacements on the ABFE, BCGD, and EFGH surfaces are fixed along X, Y, and Z directions, respectively. For the cold worked specimen A2, three loading steps are used. First, a uniaxial tensile deformation is applied onto the AEHF surface along the Y-direction (longitudinal direction) to the macroscopic strain of 33.3%, i.e. equivalent to 25% cross-section area reduction. In the second step, the model is unloaded to zero macroscopic load. These two steps are to "resemble" the effects of prior cold work. In the last step, the model is irradiated to 20 dpa with an irradiation dose rate of 10^{-7} dpa/s. Please note that our CPFE simulations indicate that Kearns factors are hardly affected by the cold work or irradiation, especially in the absence of twinning. That is, the cold worked texture used before irradiation in the model is very close to the measured one in the experiment. For the annealed specimen A1, only one irradiation step is used, without prior loading. The initial dislocation line density on each slip system is set to 10^{10} m^{-2} for both models. The influence of the initial dislocation density for the annealed model A1 and the effects of

the applied boundary conditions for the cold worked model are further discussed in section 5.4.

Table 5.4 Polycrystalline specimens used for the irradiation growth experiments [6]

Specimen	F_L	F_T	F_R	Prior irradiation condition	Grain size
Experiment A1	0.10	0.20	0.70	Annealed	20 μm
CPFE A1	0.09	0.22	0.69		
Experiment A2	0.10	0.50	0.40	25% cold working	8 μm
CPFE A2	0.09	0.56	0.35		

a. A1   b. A2   c. Random
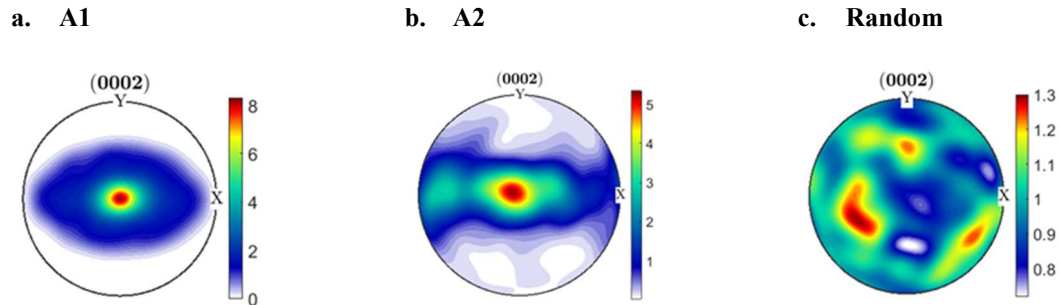
Figure 5.2 The basal pole figures of the two CPFE models that represent specimens (a) A1 and (b) A2. The longitudinal direction is along the Y-axis. (c) The basal pole figure of the CPFE model with random orientations.

Fig. 5.3b compares the average irradiation growth strain of the two CPFE models to those from experiments. The experimental results show that both specimens are expanded along the longitudinal direction. However, cold-worked specimen A2 has higher growth strains compared to specimen A1. The average growth strain is calculated using all integration points. As shown, the results of the model are in excellent agreement with the experimental data. In agreement with the measurements, the calculated irradiation growth strains of model A1 are lower than model A2. However, some differences are observed in

the magnitudes of the growth strains for specimen A1. The possible sources of such differences between the model and experiment are discussed in section 5-4.

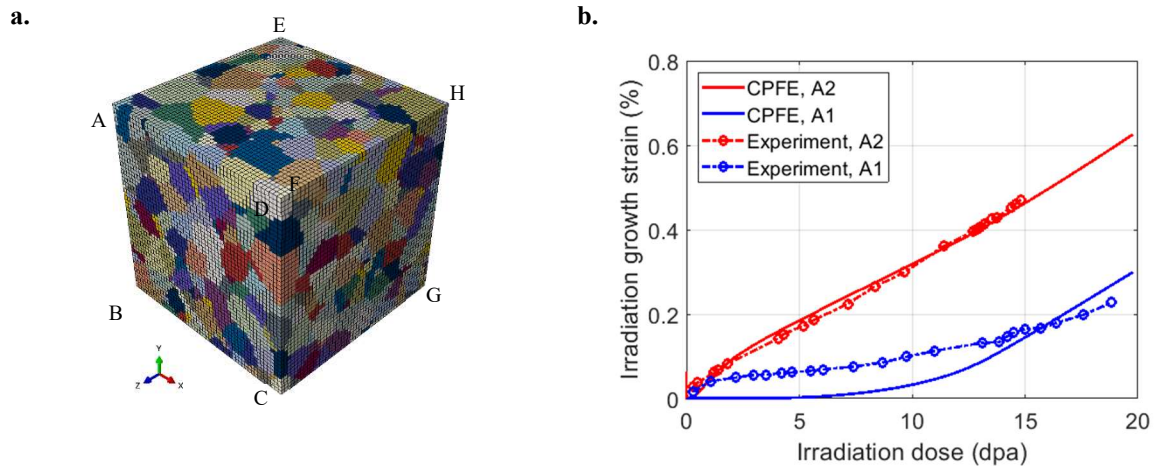a.   b.

Figure 5.3 (a) The CPFE input model used for simulating neutron irradiation effects. Random colors are assigned to elements to distinguish grains. (b) A comparison between the calculated average growth strains from the CPFE models and those measured by Rogerson [6]

The calculated average growth strain is a function of model texture, prior cold work, and average grain size. A sensitivity analysis is required to quantify the contribution of each parameter, in the absence of the others. The model used for this purpose is the one used for specimen A2, but the texture of the model is altered. The textures shown in Figs. 2a, 2b, and 2c are assigned to this model for sensitivity analysis. Fig. 5.4 compares the evolution of average growth strain from the models. The effect of model texture is shown in Fig. 5.4a where the numerical results of the three different textures in Fig. 5.2a (A1), Fig. 5.2b (A2), and Fig. 5.2c (random) are compared. It is shown that the model with random texture has nearly zero growth strain, as expected. Fig. 5.4b shows a comparison between the calculated growth strains for the models with cold work levels of 10%, 15%, and 25%. In these simulations, the texture of specimen A2 is assigned to all models, but

the amount of prior cold work varies. Numerical results indicate that the growth strain increases with cold working due to the increase in the total dislocation density.

Fig 4c compares the growth strains from models with the same texture and the same prior cold work, but different average grain sizes of 4 μm, 8 μm, and 20 μm. It is shown that the magnitude of growth strain is inversely related to the average grain size. The effects of grain size are taken into account through the use of the non-local formulation in the current dislocation-based model. The trend observed here is due to the geometrical effects of grain size which interestingly appear to be consistent with the experimental observations [7,8].
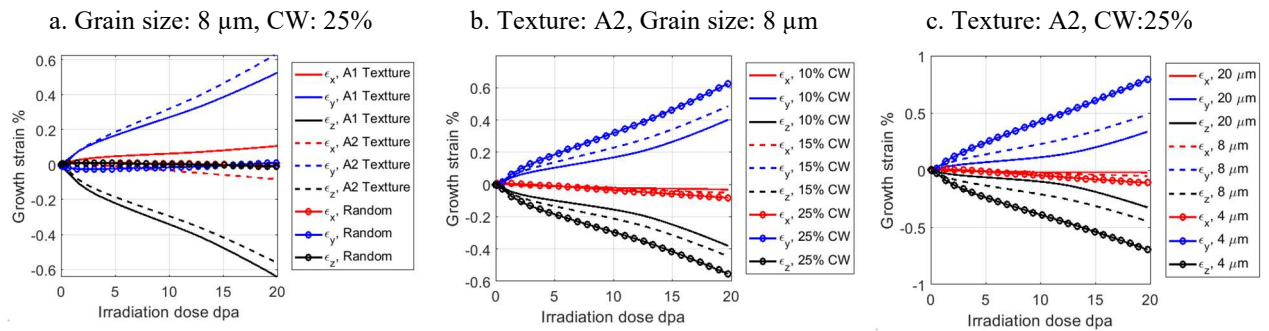
Figure 5.4 The results of the polycrystal model for average irradiation growth strain: the effects of (a) texture, (b) prior cold work, and (c) average grain size.

5.3.3   Polycrystal: local response

The numerical and experimental results presented so far show that the magnitude of average growth strain is highly affected by the texture and average grain size of the specimen as well as by the amount of prior cold work. However, there is a lack of information on how the growth strain is distributed within and across grains. In this section, the results of model A2 are used to analyse the distribution of growth strain. All reported irradiation growth strains are in the local coordinate system, along the crystal a-

axis. In addition, all reported GND and SSD densities are the total values summed over all slip systems.

Fig. 5.5 shows the distribution of the growth strain as a function of the grain size. The grain-average growth strain, GND density, and SSD density are calculated for each grain at the end of the irradiation step. The calculated values are sorted based on their corresponding grain sizes and are categorized into five groups with an equal number of data points, i.e., 207 grains in each group. The results of each group are shown using box plots with the horizontal axis representing the average grain size. A decreasing trend is observed in Fig 5a, which indicates that bigger grains accommodate less growth strain compared to the smaller grains. This can be due to the magnitude of the GND density, which is lower for bigger grains (see Fig. 5.5b). The SSD density is not really affected by the grain size (Fig. 5.5c).
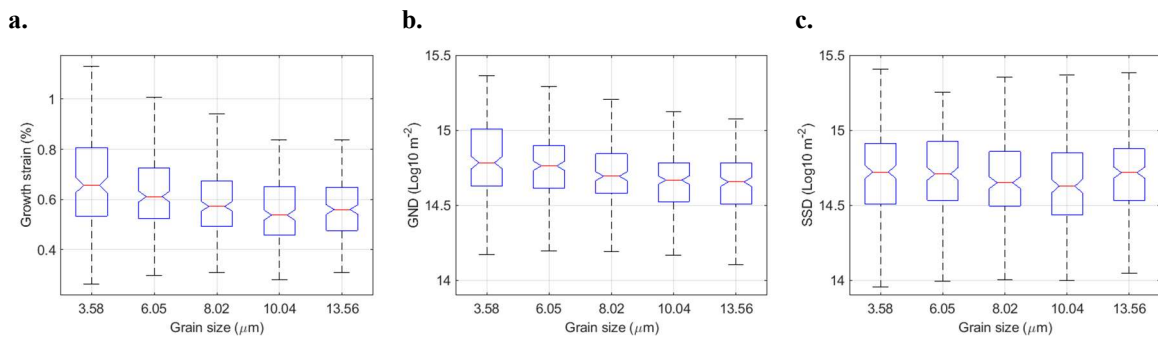
Figure 5.5 Grain-average (a) growth strain, (b) GND density, and (c) SSD density as a function of grain size for the cold worked model A2. Each box represents 207 data points

Fig 6 shows the spatial distribution of growth strains, GND density, and SSD density for model A2. Figs. 6d to 6f show the distribution of the same state variables in the mid-height cross-section of the cubic model. The growth strain is heterogeneously distributed within the grains. The shape of the non-uniformity is very similar to what is captured by

dislocation densities. For example, the growth strain is highly localized in the vicinity of the grain boundaries. In addition, growth strain localization is observed where the GNDs are localized within grains G1 and G2 (Fig. 5.6e).
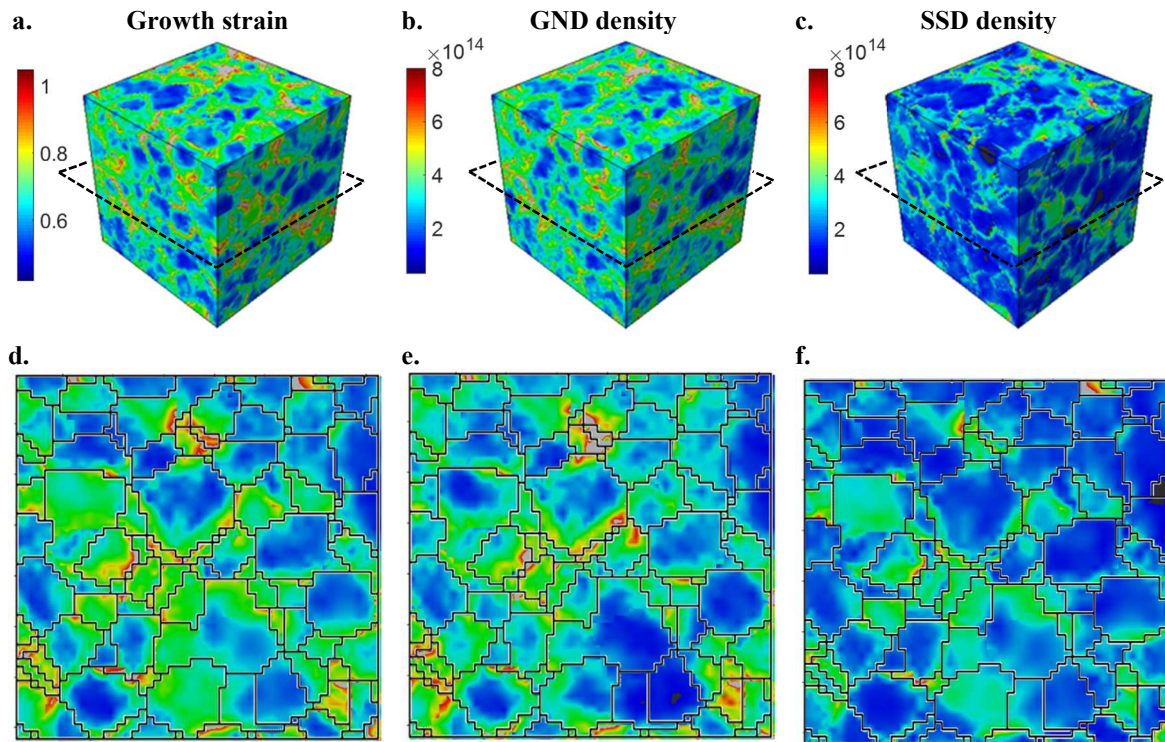
Figure 5.6 Distribution of (a) growth strain (%), (b) GND density (m^{-2}), and (c) SSD density (m^{-2}) of the 3D model of A2 sample. Cross-section at the mid-height of the model for (d) growth strain, (e) GND density, and (f) SSD density

Fig. 5.7 shows the spatial distribution of growth strain, GND density, and SSD density within one of the bigger grains of model A2 with the size of 20.8 μm. Fig. 5.7a shows that growth strain is localized where the GNDs are concentrated, and it is minimum where the GND density is minimum. The normal distribution of growth strains, GND density, and SSD density are respectively shown in Figs. 7d to 7f. The blue curve is after irradiation and the red curve is before the irradiation step. It is shown that the average

SSD density is slightly increased after the irradiation step. However, the average GND density after irradiation is the same as the one before irradiation. Fig. 5.7i shows that the increase in the SSD densities is more pronounced when all grains of the polycrystal are taken into account. The increase in the dislocation density is due to the fact that our dislocation-based CPFE model is coupled with the irradiation model. Our simulations show that neutron irradiation induces large localized strains in the areas where the dislocation densities are concentrated due to prior cold work, e.g. grain boundaries or slip bands. Such strain localization may result in further plastic deformation and subsequently further increase in dislocation density. Since the irradiation hardening effects are neglected in the current simulations, the reported increase in dislocation densities due to neutron irradiation simply represents the upper bound value. The influence of the irradiation hardening on the simulation results is further discussed in section 5.4.
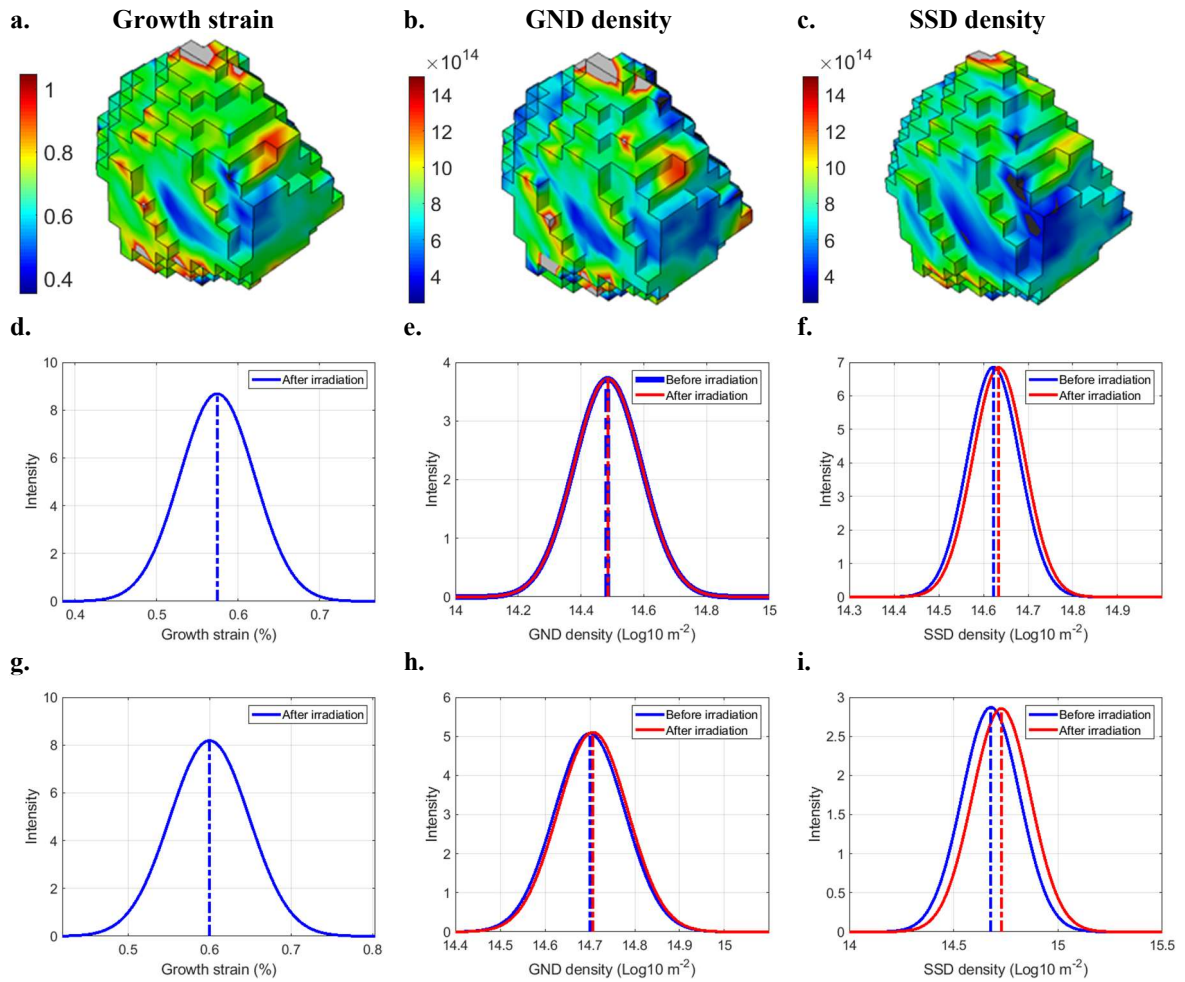
Figure 5.7 Distribution of (a) growth strain (%), (b) GND density (m⁻²), and (c) SSD density (m⁻²) in one of the large grains of model A2. The normal distribution of (d) growth strain, (e) GND density (log10 m⁻²), and (f) SSD density (log10 m⁻²) for the same grain. The normal distribution of (g) growth strain, (h) GND density (log10 m⁻²), and (i) SSD density (log10 m⁻²) for all integration points of the polycrystal model A2.

5.4   Discussion

The current model is developed by integrating the irradiation growth model of Golubov et al. [45] into a dislocation-based CPFE framework [47]. Several assumptions are made in the polycrystal simulations to study how the average growth strain is influenced by the grain size, texture, and prior cold work. These simulations showed a non-uniform distribution of growth strain within grains. In this section, the distribution of growth strain is further investigated using a bi-crystal model. In addition, the effects of grain boundary sink strength, irradiation hardening, and the applied boundary conditions on the CPFE results are discussed.

5.4.1   Bi-crystal simulations

A bi-crystal model is used to investigate the distribution of growth strain within the two grain shown in Fig. 5.8. The assumptions of section 5.3 are also used here, however, the effects of each assumption is further discussed. While the orientation of the front grain G1 is kept constant, the orientation of the grain G2 is altered to study the effects of crystal anisotropy. As shown in Fig. 5.8, the model is constrained from movement by setting $u_x^{AB} = 0$, $u_y^{AD} = 0$, and $u_z^{ABCD} = 0$. The misorientation angle between the c-axis of the grain G2 and loading direction is set at 30°, 45°, and 60° while the c-axis of the grain G1 is kept parallel to the loading direction to mimic a plastically "hard" grain. The model is discretized with 5,200 brick elements with a refined mesh used closer to the grain boundary. The model is deformed in three steps. First, a 10% tensile strain is applied uniaxially onto EFGH surface along the Z direction. In the second step, the model is unloaded and in the third step, it is subsequently irradiated for 10^8 s with an irradiation dose rate of 10^{-7} dpa/s. The size of each crystal is set to be 20 μm.
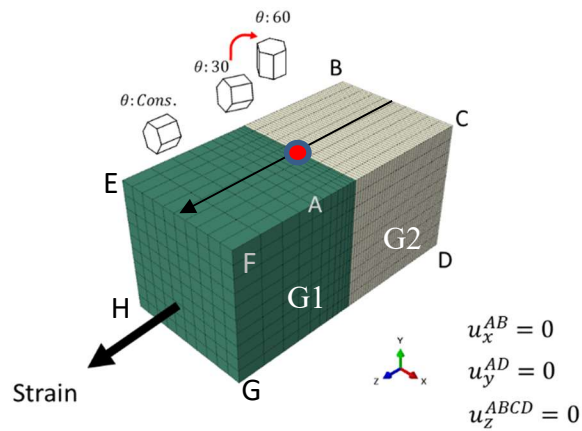
Figure 5.8 The bi-crystal input model and the implemented boundary conditions

Figs. 5.9a, 5.9b, and 5.9c show the distribution of GND densities calculated for the bi-crystal model after the unloading step, for the three different misorientation angles of 30°, 45°, and 60°. As shown, GNDs are localized at the grain boundary. For the models with 30° and 45° misorientations, the top and bottom edges of the grain G2 are the sites GNDs localize, while for the 60° case, the sides of the grain G2 are the GND concentration sites. In addition, the magnitude of GND densities localized at the grain boundary is increasing as the misorientation angle increases from 30° to 60°. Also, GNDs localize in the form of slip bands that are parallel to the most active slip systems which can be seen in all three figures [47].

Figs. 5.9d, 5.9e, and 5.9f show the distribution of growth strain in grain G2 after the irradiation step for different c-axis misorientation angles of 30°, 45°, and 60°. The grain boundary sink strength is still switched off for these simulations. The presented results are only for the soft grain G2. It is shown that growth strain tends to localize at the grain boundary as well as on the slip bands, where dislocation line density due to prior deformation concentrates.
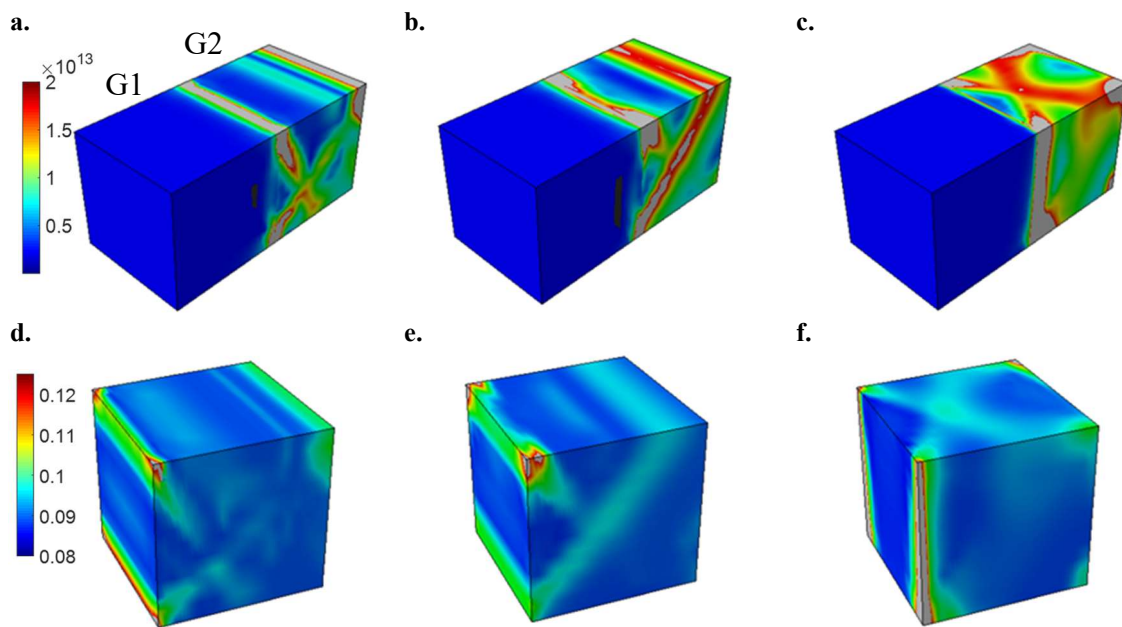
Figure 5.9 Distributions of GND densities (m⁻²) for the bi-crystal model at the end of the unload step: the c-axis misorientation angle with respect to the loading direction for grain G2 is (a) 30°, (b) 45°, and (c) 60°. The corresponding distribution of growth strain (%) for grain G2 at the end of the neutron irradiation step is shown in (d), (e), and (f)

5.4.2   The effects of grain boundary sink strength

In the previous section, we showed that in a deformed bi-crystal, growth strain localizes in the vicinity of grain. However, the effect of the grain boundary sink strength was ignored. Here, the bi-crystal model shown in Fig. 5.8 is used to study the effects of grain boundaries acting as sinks. The misorientation angle between the c-axis of the grain G2 and the loading direction is set to 45°. In addition, the irradiation time is increased to 2×10^8 s resulting in 20 dpa irradiation dose. Simulations are conducted for different grain

sizes, both for the deformed condition and the un-deformed condition, where no initial load is applied.

Fig. 5.10 shows the evolution of the calculated local growth strain along the crystal a-axis for one of the grain boundary elements. This element is marked with a red dot in Fig. 5.8. Results are compared to those without considering the grain boundary sink strength for both un-deformed (Fig. 5.10a) and deformed (Fig. 5.10b) cases. Further, grain size is varied from 1 µm to 10 µm. For the un-deformed case (Fig. 5.10a), when the grain boundary sink strength is switched off (dash line), the calculated growth does not depend on the grain size and the strain curves are nearly overlapped. However, a noticeable difference is observed when the grain boundary sink strength is switched on. The calculated strain curves can be divided into two regions, before and after irradiation dosage of ~13 dpa. When the sink strength is switched on, the calculated growth strain inversely correlates with the grain size and increases for the irradiation doses lower than 13 dpa. By increasing grain size, the growth strain curve nearly overlaps with the one with the sink strength switched off. For irradiation doses above 13 dpa, grain size has opposite effects, i.e., higher growth strains are calculated for larger grains. This trend is observed not only for this element, but also for all the grain boundary elements. Another observation is that in the absence of prior deformation, the effect of sink strength is negligible for large grains (> ~10 µm). The annealed polycrystal model A1 has the average grain size of 20 µm, i.e. higher than this threshold value. Consequently, the effects of the grain boundary sink strength term are expected to be negligible.

Fig. 5.10b shows the calculated growth strain after 20 dpa irradiation, when the bi-crystal model undergoes 10% prior plastic deformation. Both sets of simulations, i.e., with and without considering the sink strength, show significant grain size effect. This is due to the calculated magnitudes of GND densities at the grain boundary for different grain sizes

after 10% prior deformation. Although, the grain boundary sink strength does not appear to show any effects on the calculated growth strain.

a.   b.
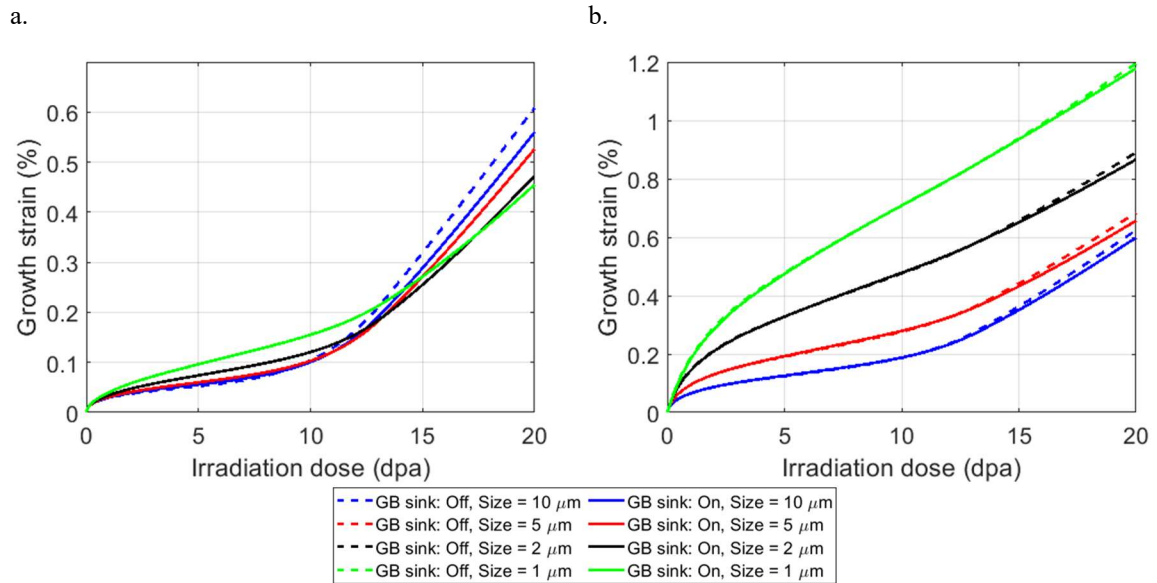
Figure 5.10 The effects of grain boundary sink strength on the evolution of growth strain for different grain sizes: (a) without prior deformation and (b) with 10% strain prior deformation. Results are for an element located at the grain boundary.

5.4.3　The effects of irradiation hardening

Irradiation hardening is the increase in the strength of slip systems as a result of neutron irradiation and the formation of dislocation loops. Such effects can be incorporated into the hardening law- see for example [29,41]. It has been shown that irradiation hardening significantly alters the post-irradiation mechanical response of zirconium [64,65]. In this study, no external load is applied, either during or after irradiation, and such effects were ignored for the sake of simplicity. During the irradiation step, this assumption leads to the calculation of an upper bound for the magnitude of dislocation densities. In this section,

the effects of the irradiation hardening on the results of the polycrystalline models A1 and A2 are investigated by considering the last term of Eq. (5-7).

Fig. 5.11 shows the evolution of the growth strain for the polycrsyal models A1 and A2 when the irradiation hardening is switched on (dash line). The results are compared to the ones where the irradiation hardening effects are switched off (solid line). It is shown that taking the irradiation hardening into account decreases the calculated growth strain. This is due to the increase in the strength of slip systems, which results in reduced plastic deformation and dislocation line density. For model A1, only a small difference is observed for irradiation doses higher than ~13 dpa. However, this difference is more pronounced for the cold-worked model A2.
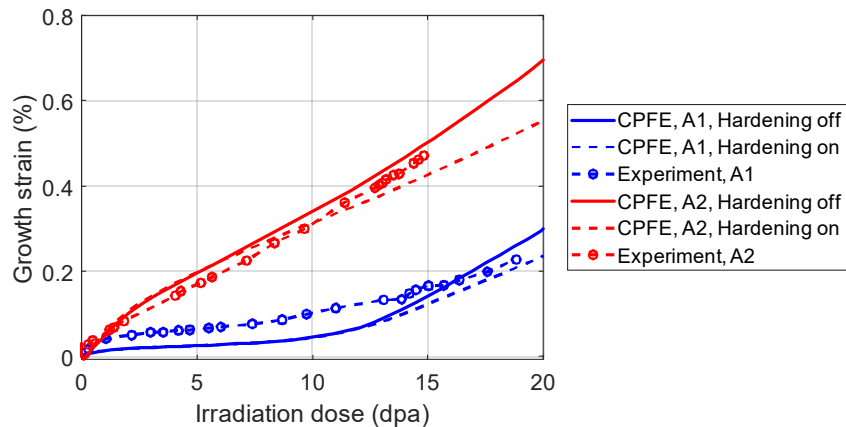

Figure 5.11 Effect of irradiation hardening on the irradiation growth strain for the A1 and A2 polycrystal models

5.4.4   The effects of boundary conditions

In this study, the cold work process was modeled by a uniaxial tension, followed by an unload step. However, the loading condition is rarely uniaxial during a cold work.

Another input model is prepared in which the loading condition is biaxial compression. The applied strain along X and Z directions is 13.4%, which induces a 25% area reduction. Fig. 5.12 compares the average growth strain of the model A2 with the biaxial loading condition to the one undergoing a uniaxial tension. It is shown that the model with biaxial deformation results in slightly higher growth strains. The calculated total dislocation density on all the slip systems prior to the irradiation step is 6.4×10^{14} m^{-2} and 6.2×10^{14} m^{-2} for the biaxial and uniaxial models, respectively.

Another assumption that was made in polycrystalline simulations was that the initial dislocation density on each slip system was 10^{10} m^{-2}. The influence of this assumption on the evolution of the average growth strain of the annealed polycrystal A1 is shown in Fig. 5.12. It is shown that by increasing the initial SSD density on each slip system from 10^{10} m^{-2} to 10^{12} m^{-2}, the average growth strain is increased for irradiation doses below 12 dpa, which is in a better agreement with the measured one. A negligible difference is observed between the two simulations after 12 dpa irradiation dosage. It is worth mentioning that the measured dislocation density of sample A1 prior to the irradiation step was reported to be less than 10^{13} m^{-2} [6].
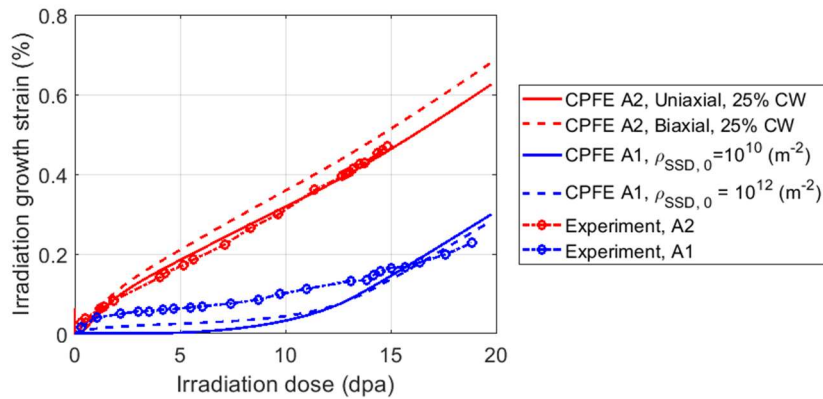
Figure 5.12 The influence of initial dislocation density on the magnitude of average growth strain calculated for model A1 and a comparison between a uniaxial and biaxial loading condition for model A2

Lastly, the contribution of twining to plastic deformation was switched off in the CPFE model. It should be noted that no effects of twinning were mentioned by Rogerson during the cold work of samples A2 [6], but if twins were formed, depending on the twin volume fractions, the texture and the average grain size of the specimens may be affected, which can consequently alter the magnitudes of the calculated growth strains. Although there are many studies focusing on the effect of irradiation on twinning [66,67], there is a lack of information on the effect of twinning on the evolution of growth strain during irradiation. This might be related to the study conducted by Carpenter et al. [63] in which it was shown that twin boundaries, with a regular arrangement of atoms, are not as efficient sinks as other types of grain boundaries with more disordered structure.

5.5 Conclusions

An irradiation growth model is adopted to integrate into a non-local crystal plasticity finite element model. The modeling results are compared against those measured for

neutron-irradiated single and polycrystalline zirconium specimens. The effects of prior cold work, as well as grain size and texture are studied in detail. It is shown that:

1. the calculated average growth strains for both annealed single crystal and cold worked polycrystal models agree well with the measured ones.

2. the average growth strains of the polycrystal models significantly depend on the polycrystals texture, average grain size, and prior cold work.

3. growth strain is non-uniformly distributed among different grains. Our statistical analysis shows that the growth strain is mainly accommodated by smaller grains, in which dislocation line densities are higher.

4. numerical results show localization of growth strains both at grain boundaries and on slip bands. The magnitude of localized growth strain is proportional to the amount of prior cold work and is inversely proportional to grain size.

5. the effect of the grain boundary sink strength on the calculated growth strain in the vicinity of the grain boundary is more significant for un-deformed crystals compared to the deformed ones.

References

[1]   G.S. Was, Fundamentals of Radiation Material Science: Metals and Alloys, Springer, Berlin, 2007.

[2]   M. Griffiths, R.A. Holt, A. Rogerson, Microstructural aspects of accelerated deformation of Zircaloy nuclear reactor components during service, J. Nucl. Mater. 225 (1995) 245–258. https://doi.org/10.1016/0022-3115(94)00687-3.

[3]   R.A. Holt, R.W. Gilbert, ⟨c⟩ Component dislocations in annealed Zircaloy irradiated at about 570 K, J. Nucl. Mater. 137 (1986) 185–189. https://doi.org/10.1016/0022-3115(86)90218-7.

[4]   C.H. Woo, Theory of irradiation deformation in non-cubic metals: Effects of anisotropic diffusion, J. Nucl. Mater. 159 (1988) 237–256. https://doi.org/10.1016/0022-3115(88)90096-7.

[5]   R.B. Adamson, C.E. Coleman, M. Griffiths, Irradiation creep and growth of zirconium alloys: A critical review, J. Nucl. Mater. 521 (2019) 167–244. https://doi.org/10.1016/j.jnucmat.2019.04.021.

[6]   A. Rogerson, Irradiation growth in zirconium and its alloys, J. Nucl. Mater. 159 (1988) 43–61. https://doi.org/10.1016/0022-3115(88)90084-0.

[7]   V. Fidleris, The irradiation creep and growth phenomena, J. Nucl. Mater. 159 (1988) 22–42. https://doi.org/10.1016/0022-3115(88)90083-9.

[8]   R.A. Murgatroyd, A. Rogerson, An assessment of the influence of microstructure and test conditions on the irradiation growth phenomenon in zirconium alloys, J. Nucl. Mater. 90 (1980) 240–248. https://doi.org/10.1016/0022-3115(80)90261-5.

[9]   C.D. Cann, D. Faulkner, K. Nuttall, R.C. Styles, A.J. Shillinglaw, C.K. Chow, A.J. Rogowski, Irradiation Growth in Zirconium and Zirconium Alloys Irradiated in the Dounreay Fast Reactor Croissance Par Irradiation Du Zirconium, 1986.

[10] R.A. Holt, Mechanisms of irradiation growth of alpha-zirconium alloys, J. Nucl. Mater. 159 (1988) 310–338. https://doi.org/10.1016/0022-3115(88)90099-2.

[11] R. Holt, A. Causey, N. Christodoulou, M. Griffiths, E. Ho, C. Woo, Non-Linear Irradiation Growth of Cold-Worked Zircaloy-2, Zircon. Nucl. Ind. Elev. Int. Symp. (1997) 623–637. https://doi.org/10.1520/STP16193S.

[12] M. Griffiths, R.W. Gilbert, C.E. Coleman, Grain boundary sinks in neutron-irradiated Zr and Zr-alloys, J. Nucl. Mater. 159 (1988) 405–416. https://doi.org/10.1016/0022-3115(88)90107-9.

[13] Q. Dong, P. Saidi, L.K. Béland, Z. Yao, C. Dai, M.R. Daymond, In situ TEM and multiscale study of dislocation loop formation in the vicinity of a grain boundary, J. Nucl. Mater. 528 (2020) 1–10. https://doi.org/10.1016/j.jnucmat.2019.151872.

[14] J.W. Zhang, S.M. Liu, W.Z. Han, Interfaces Reduce Dislocation Loop Formation in Irradiated Nanolayered Zr-2.5Nb, Scr. Mater. 200 (2021) 113902. https://doi.org/10.1016/j.scriptamat.2021.113902.

[15] D. G. Franklin, Zircaloy-4 Cladding Deformation during Power Reactor Irradiation, in: ASTM STP 754, Am. Soc. Test. Mater., 1982: pp. 235–267.

[16] K.J. Geelhood, W.G. Luscher, FRAPCON-3 . 5 : A Computer Code for the Calculation of Steady-State , Thermal-Mechanical Behavior of Oxide Fuel Rods for High Burnup Office of Nuclear Regulatory Research, 2014.

[17] R. Montgomery, C. Tomé, W. Liu, A. Alankar, G. Subramanian, C. Stanek, Use of multiscale zirconium alloy deformation models in nuclear fuel behavior analysis, J. Comput. Phys. 328 (2017) 278–300. https://doi.org/10.1016/j.jcp.2016.09.051.

[18] F. Christien, A. Barbu, Cluster Dynamics modelling of irradiation growth of zirconium single crystals, J. Nucl. Mater. 393 (2009) 153–161. https://doi.org/10.1016/j.jnucmat.2009.05.016.

[19] R.A. Holt, C.H. Woo, C.K. Chow, Production bias - a potential driving force for irradiation growth, J. Nucl. Mater. 205 (1993) 293–300. https://doi.org/10.1016/0022-3115(93)90092-D.

[20] G. Subramanian, C. Tome, Progress report on the incorporation of lower lengthscales into polycrystal plasticity models, 2012.

[21] Y. Li, N. Ghoniem, Cluster dynamics modeling of irradiation growth in single crystal Zr, J. Nucl. Mater. 540 (2020) 152312. https://doi.org/10.1016/j.jnucmat.2020.152312.

[22] M.E. Cazado, E. Goldberg, M.A. Togneri, A. Denis, A. Soba, A new irradiation growth model for Zr-based components of nuclear reactors for the DIONISIO code, Nucl. Eng. Des. 373 (2021) 111009. https://doi.org/10.1016/j.nucengdes.2020.111009.

[23] F. Christien, A. Barbu, Effect of self-interstitial diffusion anisotropy in electron-irradiated zirconium: A cluster dynamics modeling, J. Nucl. Mater. 346 (2005) 272–281. https://doi.org/10.1016/j.jnucmat.2005.06.024.

[24] S. Il Choi, G.G. Lee, J. Kwon, J.H. Kim, Modeling of sink-induced irradiation growth of single-crystal and polycrystal zirconiums in nuclear reactors, J. Nucl.

Mater. 468 (2016) 56–70. https://doi.org/10.1016/j.jnucmat.2015.11.014.

[25]   X. Lu, X. Zhang, M. Shi, F. Roters, G. Kang, Dislocation mechanism based size-dependent crystal plasticity modeling and simulation of gradient nano-grained copper, Int. J. Plast. 113 (2019) 52–73. https://doi.org/10.1016/j.ijplas.2018.09.007.

[26]   F. Han, F. Roters, D. Raabe, Microstructure-based multiscale modeling of large strain plastic deformation by coupling a full-field crystal plasticity-spectral solver with an implicit finite element solver, Int. J. Plast. 125 (2020) 97–117. https://doi.org/10.1016/j.ijplas.2019.09.004.

[27]   M. Kasemer, P. Dawson, A finite element methodology to incorporate kinematic activation of discrete deformation twins in a crystal plasticity framework, Comput. Methods Appl. Mech. Eng. 358 (2020) 112653. https://doi.org/10.1016/j.cma.2019.112653.

[28]   C. Mareau, M.R. Daymond, Study of internal strain evolution in Zircaloy-2 using polycrystalline models : Comparison between a rate-dependent and a rate-independent formulation, Acta Mater. 58 (2010) 3313–3325. https://doi.org/10.1016/j.actamat.2010.02.005.

[29]   F. Onimus, M. Bono, B. Verhaeghe, A. Soniak, P. Pilvin, Polycrystalline modeling of the behavior of neutron-irradiated recrystallized zirconium alloys during strain path change tests, Int. J. Plast. 134 (2020) 102835. https://doi.org/10.1016/j.ijplas.2020.102835.

[30]   R.A. Lebensohn, A. Needleman, Numerical implementation of non-local polycrystal plasticity using fast Fourier transforms, J. Mech. Phys. Solids. 97 (2016) 333–351. https://doi.org/10.1016/j.jmps.2016.03.023.

[31]   H. Wang, P.D. Wu, J. Wang, C.N. Tomé, A crystal plasticity model for hexagonal close packed (HCP) crystals including twinning and de-twinning mechanisms, Int. J. Plast. 49 (2013) 36–52. https://doi.org/10.1016/j.ijplas.2013.02.016.

[32]   A. Patra, D.L. Mcdowell, Acta Materialia Crystal plasticity investigation of the microstructural factors in fl uencing dislocation channeling in a model irradiated bcc material, Acta Mater. 110 (2016) 364–376. https://doi.org/10.1016/j.actamat.2016.03.041.

[33]   H. Abdolvand, Progressive modelling and experimentation of hydrogen diffusion

and precipitation in anisotropic polycrystals, Int. J. Plast. 116 (2019) 39–61. https://doi.org/10.1016/j.ijplas.2018.12.005.

[34] A. Alawadi, H. Abdolvand, Measurement and modeling of micro residual stresses in zirconium crystals in three dimension, J. Mech. Phys. Solids. 135 (2020) 103799. https://doi.org/10.1016/j.jmps.2019.103799.

[35] H. Abdolvand, K. Louca, C. Mareau, M. Majkut, J. Wright, On the nucleation of deformation twins at the early stages of plasticity, Acta Mater. 196 (2020) 733–746. https://doi.org/10.1016/j.actamat.2020.07.010.

[36] K. Louca, H. Abdolvand, C. Mareau, M. Majkut, J. Wright, Formation and annihilation of stressed deformation twins in magnesium, Commun. Mater. 2 (2021) 1–11. https://doi.org/10.1038/s43246-020-00105-y.

[37] A. Tondro, H. Abdolvand, Quantifying hydrogen concentration in the vicinity of zirconium hydrides and deformation twins, J. Mech. Phys. Solids. 148 (2021) 104287. https://doi.org/10.1016/j.jmps.2020.104287.

[38] A. Patra, D.L. McDowell, Continuum modeling of localized deformation in irradiated bcc materials, J. Nucl. Mater. 432 (2013) 414–427. https://doi.org/10.1016/j.jnucmat.2012.08.021.

[39] S. Berbenni, V. Taupin, R.A. Lebensohn, A fast Fourier transform-based mesoscale field dislocation mechanics study of grain size effects and reversible plasticity in polycrystals R, J. Mech. Phys. Solids. 135 (2020) 1–23. https://doi.org/10.1016/j.jmps.2019.103808.

[40] S. El Shawish, P.G. Vincent, H. Moulinec, L. Cizelj, L. Gélébart, Full-field polycrystal plasticity simulations of neutron-irradiated austenitic stainless steel: A comparison between FE and FFT-based approaches, J. Nucl. Mater. 529 (2020). https://doi.org/10.1016/j.jnucmat.2019.151927.

[41] T.O. Erinosho, F.P.E. Dunne, Strain localization and failure in irradiated zircaloy with crystal plasticity, Int. J. Plast. 71 (2015) 170–194. https://doi.org/10.1016/j.ijplas.2015.05.008.

[42] C.N. Tomé, N. Christodoulou, P.A. Turner, M.A. Miller, C.H. Woo, J. Root, T.M. Holden, Role of internal stresses in the transient of irradiation growth of Zircaloy-2, J. Nucl. Mater. 227 (1996) 237–250. https://doi.org/10.1016/0022-3115(95)00140-9.

[43] C.H. Woo, Modeling irradiation growth of zirconium and its alloys, Radiat. Eff. Defects Solids. 144 (1998) 145–169. https://doi.org/10.1080/10420159808229674.

[44] A. V Barashev, S.I. Golubov, R.E. Stoller, Theoretical investigation of microstructure evolution and deformation of zirconium under neutron irradiation, J. Nucl. Mater. 461 (2015) 85–94. https://doi.org/10.1016/j.jnucmat.2015.02.001.

[45] S.I. Golubov, A. V. Barashev, R.E. Stoller, On the origin of radiation growth of hcp crystal, ORNL/TM-2011/473. (2011).

[46] A. Patra, C.N. Tomé, S.I. Golubov, Crystal plasticity modeling of irradiation growth in Zircaloy-2, Philos. Mag. 97 (2017) 2018–2051. https://doi.org/10.1080/14786435.2017.1324648.

[47] O. Sedaghat, H. Abdolvand, A non-local crystal plasticity constitutive model for hexagonal close-packed polycrystals, Int. J. Plast. 136 (2021) 102883.

[48] R.J. Asaro, A. Needleman, Overview No. 42 Texture developement and strain hardening in rate dependant polycrystals, Acta Metall. 33 (1985) 923–953.

[49] R.J. Asaro, Crystal Plasticity, J. Appl. Mech. 50 (1983) 921–934.

[50] E.S. Fisher, C.J. Renken, Single-Crystal Elastic Moduli and the hcp ~ bcc Transformation in Ti, Zr, and Hf, Phys. Rev. 135 (1964) A482–A494.

[51] G.I. Taylor, The Mechanism of Plastic Deformation of Crystals. Part1. Theoretical, Proceeding R. Soc. 538 (1934) 362–387.

[52] M.F. Ashby, The deformation of plastically non-homogeneous materials, Philos. Mag. Philos. Mag. 21 (1970) 399–424.

[53] L.P. Evers, W.A.M. Brekelmans, M.G.D. Geers, Non-local crystal plasticity model with intrinsic SSD and GND effects, J. Mech. Phys. Solids. 52 (2004) 2379–2401. https://doi.org/10.1016/j.jmps.2004.03.007.

[54] A. Ma, F. Roters, D. Raabe, A dislocation density based constitutive model for crystal plasticity FEM including geometrically necessary dislocations, Acta Mater. 54 (2006) 2169–2179. https://doi.org/10.1016/j.actamat.2006.01.005.

[55] I.J. Beyerlein, C.N. Tome, A dislocation-based constitutive law for pure Zr including temperature effects, 24 (2008) 867–895.

https://doi.org/10.1016/j.ijplas.2007.07.017.

[56]   K.S. Cheong, E.P. Busso, A. Arsenlis, A study of microstructural length scale effects on the behaviour of FCC polycrystals using strain gradient concepts, Int. J. Plast. 21 (2005) 1797–1814. https://doi.org/10.1016/j.ijplas.2004.11.001.

[57]   A. Arsenlis, Modeling Dislocation Density Evolution in Continuum Crystal Plasticity, PhD thesis, Massachusetts Institute of Technology, 2001.

[58]   A. Arsenlis, D.M. parks, Crystallographic aspects of geometrically nesesary and statistically stored dislocation density, Acta Mater. 47 (1999) 1597–1611.

[59]   N. De Diego, Y.N. Osetsky, D.J. Bacon, Mobility of interstitial clusters in alpha-zirconium, Metall. Mater. Trans. A Phys. Metall. Mater. Sci. 33 (2002) 783–789. https://doi.org/10.1007/s11661-002-0145-y.

[60]   A. Patra, C.N. Tomé, S.I. Golubov, Crystal plasticity modeling of irradiation growth in Zircaloy-2, Philos. Mag. 6435 (2018) 0. https://doi.org/10.1080/14786435.2017.1324648.

[61]   A. V. Barashev, S.I. Golubov, R.E. Stoller, Theoretical investigation of microstructure evolution and deformation of zirconium under neutron irradiation, J. Nucl. Mater. 461 (2015) 85–94. https://doi.org/10.1016/j.jnucmat.2015.02.001.

[62]   P.T. Heald, J.E. Harbottle, Irradiation creep due to dislocation climb and glide, J. Nucl. Mater. 67 (1977) 229–233. https://doi.org/10.1002/pssa.2210640239.

[63]   G.J.C. Carpenter, R. Zee, A. Rogerson, Irradiation Growth of Zirconium Single-Crystals - a Review, J. Nucl. Mater. 159 (1988) 86–100. https://doi.org/10.1016/0022-3115(88)90087-6.

[64]   F. Long, L. Balogh, D.W. Brown, P. Mosbrucker, T. Skippon, C.D. Judge, M.R. Daymond, Effect of neutron irradiation on deformation mechanisms operating during tensile testing of Zr-2.5Nb, Acta Mater. 102 (2016) 352–363. https://doi.org/10.1016/j.actamat.2015.09.032.

[65]   L. Cogez, W. Li, O.T. Woo, MECHANICAL PROPERTIES OF ZIRCALOY-2 NEUTRON IRRADIATED TO HIGH FLUENCE, CNL Nucl. Rev. 6 (2017) 221–230.

[66]   Y. Higashiguchi, H. Kayano, T. Onchi, Effect of fast-neutron irradiation on

deformation twinning in zirconium deformed at 77 K, J. Nucl. Mater. 80 (1979) 24–34. https://doi.org/10.1016/0022-3115(79)90216-2.

[67] K. Wang, Y. Dai, P. Spätig, Deformation twinning in irradiated ferritic/martensitic steels, J. Nucl. Mater. 501 (2018) 336–346. https://doi.org/10.1016/j.jnucmat.2018.01.057.

Chapter 6

6 Nucleation and growth of $\{11\bar{2}2\}$ twins in titanium: Elastic energy and stress fields at the vicinity of twins

A crystal plasticity finite element (CPFE) model is updated to study nucleation, elongation, and thickening of deformation twins in a commercially pure titanium. The results of the CPFE simulations are compared with previously published data for an *in-situ* high resolution electron backscattered diffraction experiment that was conducted on a titanium micro-pillar. The evolution of both local resolved shear stress and elastic energy during twin formation are studied in detail. It is shown that twins are nucleated at the locations where the strain energy and resolved shear stress are maximum. After nucleation, resolved shear stresses at the twin tips stay positive which provide the driving force required for twin elongation, however, they are negative at the twin surface for short twins. It is shown that three-dimensional studies are necessary to understand nucleation and twinning.

6.1 Introduction

α-titanium has hexagonal close-packed (HCP) crystal structure and has been used vastly in aerospace industry due to its superior mechanical properties and light weight. Depending on the state of the applied stress, strain rate [1,2], temperature [3], and materials texture, twinning can be one of the dominant deformation mechanism in titanium polycrystals, where both tension and compression twins can form [4].

It is generally assumed that the formation of twins in HCP polycrystals follows three-steps: nucleation, propagation and thickening [5–7]. At the nucleation step, a twin

embryo forms. If enough driving force is provided, it will then propagate in the parent grain. The second step involves generation and glide of the twin partial dislocations along the primary shear direction, while the third step features transverse propagation mainly perpendicular to the primary shear direction [8]. In the recent years, crystal plasticity finite element (CPFE) as well as full-field Fast Fourier Transform (FFT) models have focused on capturing these three steps [9–12]. For instance, Cheng et al. have used an image-based CPFE approach for explicit simulation of twins in Mg alloys [13,14]. It was shown that after twin nucleation, twin tip stress concentration drives the twin front to propagate forward and accounts for the high twin propagation velocity [12]. This was done through a CPFE formulation where the elastic theory of dislocations were adopted to account for the energy change during twin nucleation.

In another study by Kumar et al [9], an elasto-visco-plastic FFT model was developed to study the driving forces of twin growth. It was shown that the twin transformation strain plays a major role in re-configuring the stress field in the parent grain. Such stress alteration can in fact be responsible for how a second twin nucleates in a grain [10] or even how they transmit across grain boundaries [15]. Furthermore, Liu et al. have recently used FFT model to calculate the stress distributions close to the twin tips that form during deformation of Mg micro-pillars [16]. The nucleation and growth of multiple twins in the pillar were studied particularly the effects of twins separation distance.

In this chapter, the subroutine developed by Abdolvand and Wilkinson [17] is used to simulate the three steps of twin formation in a titanium micro-pillar. We focus on the variation of the elastic energy and stress fields close to twins. This is to show that without using complex formulation, and by incorporating twinning transformation strain into CPFE models, it is still possible to capture the observed trends in the variation of the stress fields close to twins. The CPFE results are compared with the previously published

experimental data for an in-situ High Resolution Electron BackScatter Diffraction (HR-EBSD) experiment that was performed on a titanium micro-pillar [18].

6.2   Experiment

All of the three steps in twin formation was captured in the HR-EBSD experiment while the stress fields close to twins were measured in-situ. Details of the experiment can be found elsewhere [18]. Here a brief description is given. A titanium micro-pillar consisting of two grains was deformed by applying compressive load while monitoring nucleation and growth of twins. The pillar initially had two grains and a small twin that was formed during sample preparation. This twin is labeled as "top twin" as it was located close to the pillar's top surface. The test set-up and orientation analysis of the grains are provided in the Fig. 6.1. The analysis of the grain orientations indicated that the main bigger grain has its crystal c-axis along the loading direction and hence, tend to twin under compressive loading. In this notation, y is along the pillar's axis and coincide with the loading direction, x is perpendicular to y, and z is along the thickness of the pillar. HR-EBSD was conducted on the top face of the pillar. The smaller neighbouring grain, on the other hand, was plastically soft. The compressive load was applied at the strain rate of $(\sim 10^{-2} \text{ s}^{-1})$, but it was on-hold at different stages to measure stress fields in-situ. These strains are measured on the x-y surface of the pillar by cross-correlating backscattered diffraction patterns. A comprehensive explanation of the implemented HR-EBSD method is given in the references [17,19,20]. We focus on three main measurement steps which determine stress fields right before nucleation (EBSD-2), after elongation (EBSD-3), and after thickening (EBSD-4) of the "bottom twin". These steps are shown in the Fig. 6.1d. Orientation analysis indicated that both top and bottom twins were the same variant of the $\{11\bar{2}2\}$ $<11\bar{2}3>$ contraction twin family [18]. It was observed that the bottom twin nucleated and elongated firstly. This was followed by thickening as more strain applied,

while the top-twin started to propagate and thicken. In this chapter and by the use of CPFE modeling, we discuss why this particular sequence was observed.

6.3 Model

The measured sample geometry were used to construct the FE input model (Fig. 6.1d). The measured orientation of the twin and parent and the determined twin variant [18] were used to partition the FE model so that twin domains can be identified in 3D. To apply compressive load, a velocity was applied to the top of the pillar such that its corresponding strain rate matches with the one used in the experiment. The displacement measured in the experiment seem to suffer from the compliance of the nano-indentation device so as the measured strain, strain rate, and elastic modulus. Hence, the possible effects of such variations on the results are discussed.
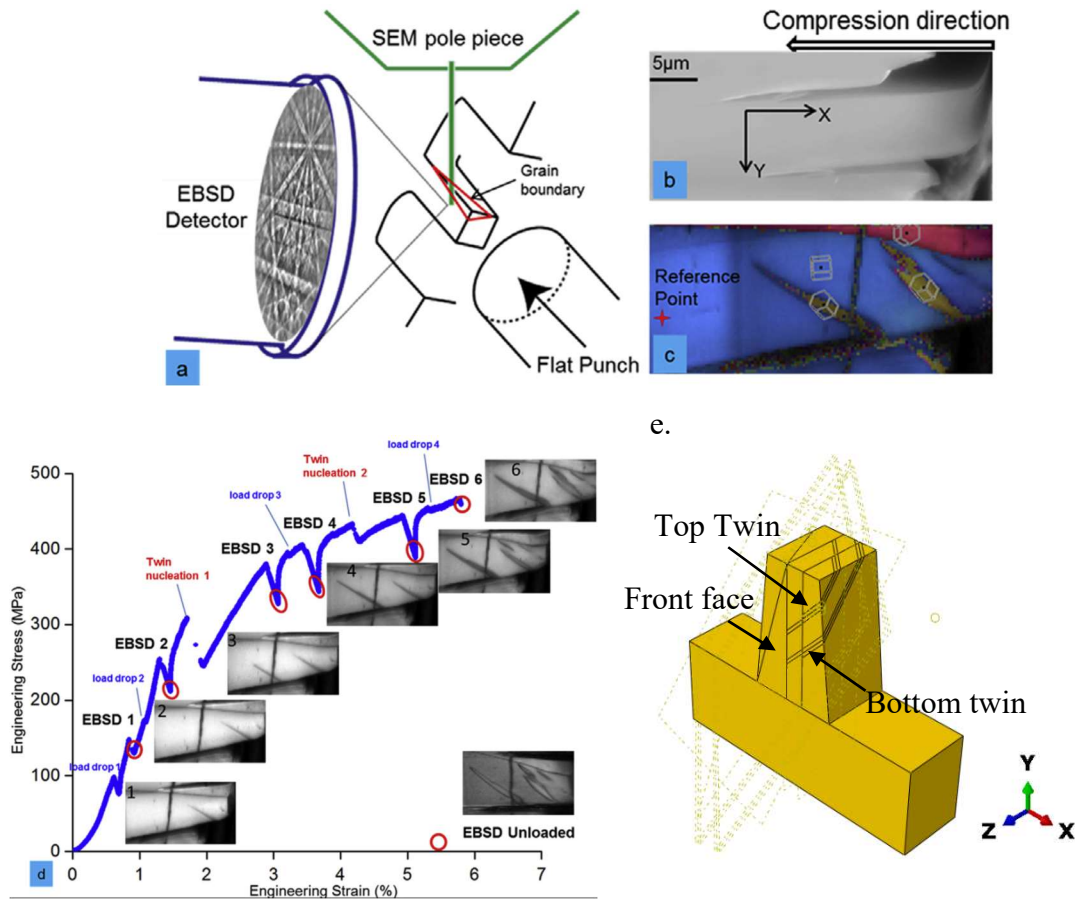
Figure 6.1 (a) Test set-up for the in-situ high resolution Electron backscatter diffraction experiment [18]. (b) Sample geometry and loading direction. (c) Orientation map of the pillar before deformation. (d) In-situ measured engineering stress-strain curve. In-situ HR-EBSD measurements were performed at the locations marked in (d). (e) Finite element input model. Planes in (e) represent the twin habit planes calculated by orientation analysis of twin-parent pairs. These planes were used to regenerate twins' geometries in 3D.

The User MATerial (UMAT) subroutine developed by Abdolvand and Wilkinson [21] was modified for CPFE modeling. This subroutine links to ABAQUS FE solver to calculate stress increment, based on a given strain and time increment provided. In brief, for a given strain increment, the contribution of slip to plastic strain can be determined by knowing active slip systems and the shear that they can accommodate. This shear can be calculated by time integration of the slip rate determined for each slip system. Slip rate correlates with the resolved shear stress acting on the slip system divided by the current strength of the slip system [22]. Following Kumar et al. [10] we assume that for titanium, basal $\langle11\bar{2}0\rangle$, prism $\langle11\bar{2}0\rangle$ and pyramidal $\langle11\bar{2}3\rangle$ are the active slip systems at room temperature. The critical resolved shear stresses for prism, basal, and pyramidal <c+a> systems are assumed to be 60, 120, and 180 MPa, respectively [23].

Twinning was modeled in three steps. To take into account the compliance of the nano-indenter, the nucleation step was set to happen at 1.5% applied strain. At this strain, the twin domain was reoriented and the twin transformation strain ($\Delta\gamma^{tw}$) was subsequently applied. This was done under constant applied strain, i.e., the applied velocity at the top of the pillar was set to zero. It was assumed that the reorientation step happened over one second, to let the twin domain re-equilibrate, while transformation strain was applied in 3940 seconds (T_{TST}) incrementally following Eq. 6-1

$$\Delta\gamma^{tw} = \frac{0.218}{T_{TST}}\Delta t$$

$$\Delta\varepsilon^{tr} = S^{tw}\Delta\gamma^{tw}$$

(6-1)

Where Δt is the time increment defined by FE solver, and S^{tw} is the twin variant Schmid tensor. The selected time step is to resemble quasi-static loading ($\dot{\varepsilon} = 5\times10^{-5}\ s^{-1}$) and is not meant to capture the real dynamic process, but rather to overcome the possible

numerical instabilities resulting from significant localized deformation. At the end of the twin nucleation step, stress and elastic fields in the pillar are studied to decide if it is preferable to nucleate another twin or let the current twin propagate or thicken. For propagation step, twin was elongated by assigning twin orientation into the new domain and applying twin transformation strain, whereas in the thickening step, twin size increased perpendicular to the twin habit plane.

6.4   Results and discussion

The results of the CPFE simulations for σ_{xy} are shown in Fig. 6.2a and are compared with those measured with HR-EBSD (Fig. 6.2b). This stress component was particularly selected as stress sign alternates quite distinctly in comparison to σ_{xx} or σ_{yy}. The corresponding CPFE result for each EBSD step is labeled with FE-EBSD-X where X represent the measurement step. In Fig 1a, the effects of twin nucleation strain and applied strain rate are studied in detail. In Fig. 6.2aI, the top twin is removed from the model, i.e. no twin exist prior to loading. FE results for applied strain of 0.6% indicate that under compressive force, the north part of the pillar tend to shear toward negative x. This is interesting as it indicates that a twin is required to accommodate such deformation. Both twins that formed in this pillar have a shear component in this direction.

In the rest of the FE results presented, the top twin was included in the model as a grain that existed before any load applied. In Fig. 6.2aII, it is shown that a negative stress field exist right above this twin that did not exist in Fig. 6.2aI. However with further loading, the size and magnitude of this negative stress field decreases (see Fig 1aII-VI). It is shown that at the applied strain of 1.5%, a tensile stress field form at the tip of the top twin (Fig. 6.2aIII). This is also captured in the experiment (Fig. 6.2b) and is marked with a red ellipse.

To study the possible effects of indenter compliance on the recorded strain, various strain rates were used in our CPFE simulation to investigate the resulting stress fields. As an example, results for strain of 10^{-5} s^{-1} are shown in Fig. 6.2aIV. At the applied strain of 1.5%, minor changes are observed in comparison to Fig. 6.2aIII. Perhaps, the most notifiable difference is the size of the compressive stress field that formed above the top-twin, where a smaller field was captured for the strain rate of 10^{-5} s^{-1}.

To be consistent with the experimental observation, at the applied strain of 1.5%, the bottom twin zone was reoriented and twin shear was applied to the twin domain. This was followed by further straining to 2.8% so that the results of the CPFE can be compared to EBSD-3. This results are shown in Fig. 6.2aV, where a negative stress fields was captured close to the head of the pillar and stronger positive stress was captured close to both top and bottom twins. Qualitatively, these results are in agreement with the experimental ones, however the magnitudes of the calculated stress fields are off. One of the reasons for such difference is that in the experiment it is possible that piles of dislocations form under surface. In diffraction patterns, this will be reflected by significant movement of the features in the pattern which lead to measuring high stress and lattice rotation. Such localized stress fields resulting from dislocation pile-up cannot be captured in the modeling approached used here. Further, extracting elastic strain in the existence of large lattice rotation is not straightforward as lattice rotations are normally 10 times bigger than elastic strains. Large lattice rotations have been reported at the vicinity of twins.

 At the applied strain of 2.8%, it was allowed to have the bottom twin elongated (see below). This step was followed by further straining to 3.24% where EBSD-4 was conducted. The result of CPFE simulation for this strain is shown in Fig. 6.2aVI, where in agreement with experiment, a higher positive stress filed is captured at the vicinity of

both twins. Further, the size of the negative stress field close to the top of the pillar has decreased significantly, which is also in agreement with the experiment.
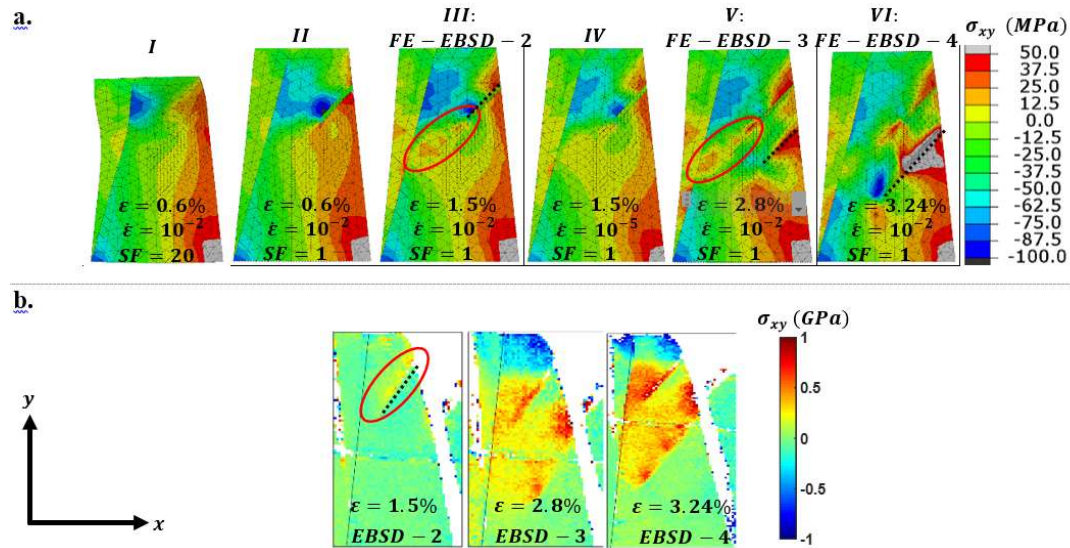

Figure 6.2 Comparison between the CPFE and HR-EBSD results for σ_{xy}. The applied strain and strain rate for CPFE results are given within each sub-figure. Scale Factor (SF) for aI was set to 20, while for the rest of the results was set to 1. Black dotted lines were drawn to indicate the trace of the twin.

Since CPFE results does not change notably between strain rates of 10^{-5} to 10^{-2} s^{-1}, the measured strain rate of 10^{-2} s^{-1} was used in the rest of the simulations. So far, results are given in the global coordinate system (see Fig. 6.3c), however, to understand the local stress fields acting on both twins, a new coordinate system is determined where 1 and 3 represent twin shear direction and normal to the twin plane, respectively. The second axis is determined by the cross product of the other two. Here, we focus on the shear stress that act on the twin plane and in the twin direction (σ_{13}^{L}).

In Fig. 6.3, the calculated local shear stress (σ_{13}^L) and the elastic energy ($E = \frac{1}{2}\sigma_{ij}\varepsilon_{ij}$) at different applied strains are shown and compared with the measured ones. In Fig. 6.3a, it is shown that σ_{13}^L generally increases at the vicinity of the twins as applied stress increases. Having positive σ_{13}^L is necessary for twin nucleation and propagation. The other key parameter is elastic energy, as twin formation tend to reduce the total elastic energy of the twin-parent pair [24]. In Fig. 6.3b, a plot of the elastic energy, the calculated energy from resolved shear stress and elastic resolved shear strain ($\sigma_{13}^L\varepsilon_{13}^L$), and resolved shear stress (σ_{13}^L) at the top right corner of the pillar is presented. CPFE simulation indicated that this corner is where these values peak. The distance on the horizontal axis is from the top right corner of the pillar toward positive z (See the blue arrow in Fig. 6.3c). All of the plotted parameters, E, $\sigma_{13}^L\varepsilon_{13}^L$, and σ_{13}^L, are normalized with respect to their corresponding values calculated at the top left corner of the pillar, i.e., 0.955 MJ/mm3, 0.4639 MJ/mm3, and 203 MPa, respectively. It is clear that both energy and σ_{13}^L peak at the locations where twins nucleated. The first one is at ~4.5 μm from the corner where the bottom twin nucleated and the second one is at ~8.5 μm where the top twin nucleated. Further, the first twin nucleated at the location where both energy and σ_{13}^L were at their maximum.

In Fig. 6.3c, the distributions of σ_{13}^L and E at the applied strain of 1.5% are shown. In Fig 2c-2h, the top twin was included in CPFE simulations before any load applied. In agreement with EBSD-2, CPFE results show a high concentration of σ_{13}^L at the head of the top twin on the x-y plane. Since EBSD was performed just on the front x-y surface, it was not possible to comment on why the second twin nucleated instead of having the top twin elongated. This could be misleading given that EBSD measurement does not show significant σ_{13}^L concentration at the location where the bottom twin nucleated. CPFE

simulation shows that in fact, the highest local shear stress (σ_{13}^L) occur on the z-y plane underneath the EBSD surface. This is where the second twin nucleated.

In Fig. 6.3d, the distributions of the σ_{13}^L and E after nucleation of the bottom twin under constant applied strain of 1.5% are shown. It is clear that applying the 0.219 twin transformation strain to the twin domain has led to significant reduction of both σ_{13}^L and E. At this stage, σ_{13}^L is positive only at the tip of the bottom twin. This means that the bottom twin tends to elongate rather than increasing its thickness. However, this might not be enough as the elastic energy is quite low, even close to the bottom twin's tip. The σ_{13}^L profile right before twin nucleation and after the twin shear transfer is shown in Fig. 6.3e. The distance is from the pillar edge and is along the red arrow, as shown in Fig. 6.3c. It is shown that the positive resolved shear stress becomes negative in the twin region right after shear transfer. This is in agreement with similar study on Mg alloys [9]. In Fig. 6.3f it is shown that with further straining of the sample, very high σ_{13}^L will develop close to both twin tips, but elastic energy is still maximum at the vicinity of the top twin, close to pillar's top surface, and hence it is favourable for this twin to elongate. It is interesting to report that σ_{13}^L is still quite low on the back of the bottom twin on the x-y surface. This means that the bottom twin should tend to elongate on this surface rather than increasing its thickness. This is also observed in the experiment. With further straining, the bottom twin elongated first and then thickened. Hence, at the applied strain of 2.8%, the size of the bottom twin increased to resemble elongation.
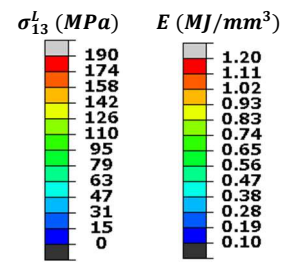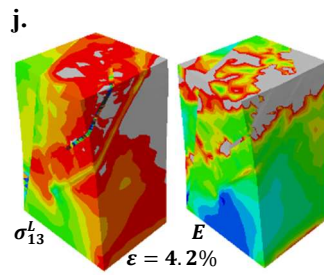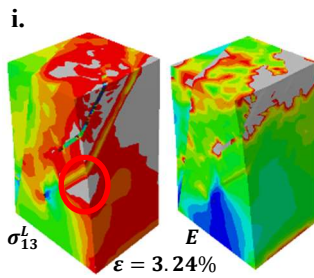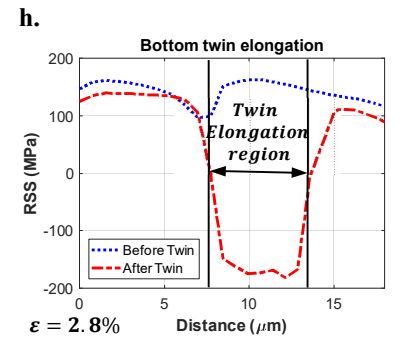
a.

EBSD − 2
$\varepsilon = 1.5\%$

EBSD − 3
$\varepsilon = 2.8\%$

EBSD − 4
$\varepsilon = 3.24\%$

EBSD − 5
$\varepsilon = 4.2\%$

b.

c. FE − EBSD − 2

σ_{13}^L E

$\varepsilon = 1.5\%$

d.

σ_{13}^L E

$\varepsilon = 1.5\%$

e.

Bottom twin nucleation

Twin Nucleation region

Before Twin
After Twin

$\varepsilon = 1.5\%$

f. FE − EBSD − 3

σ_{13}^L E

$\varepsilon = 2.8\%$

g.

σ_{13}^L E

$\varepsilon = 2.8\%$

h.

Bottom twin elongation

Twin Elongation region

Before Twin
After Twin

$\varepsilon = 2.8\%$

i.

σ_{13}^L E

$\varepsilon = 3.24\%$

j.

σ_{13}^L E

$\varepsilon = 4.2\%$

$\sigma_{13}^L \ (MPa)$ $E \ (MJ/mm^3)$

190	1.20
174	1.11
158	1.02
142	0.93
126	0.83
110	0.74
95	0.65
79	0.56
63	0.47
47	0.38
31	0.28
15	0.19
0	0.10
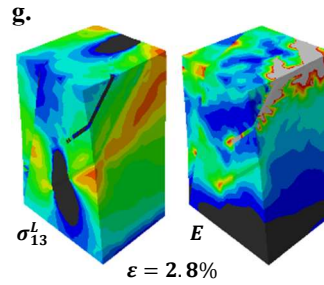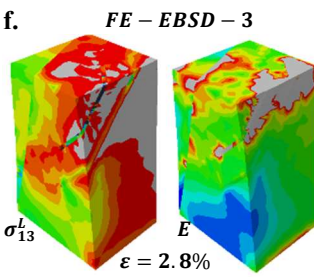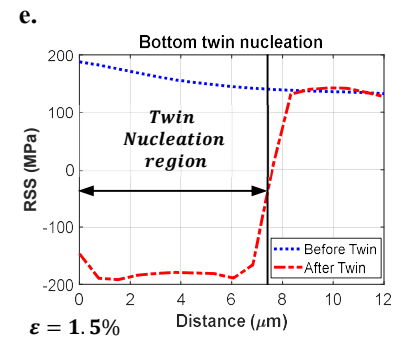
Figure 6.3 Comparison between measured and simulated local resolved shear stresses (σ_{13}^L) at different stages of twin formation. (a) HR-EBSD results at different applied strains. (b) Calculated elastic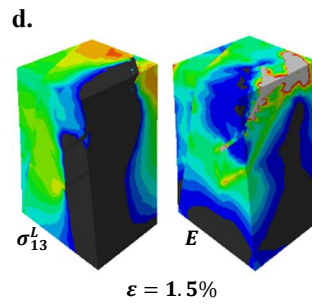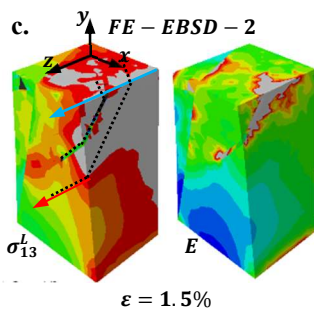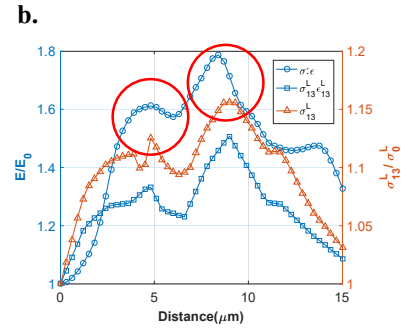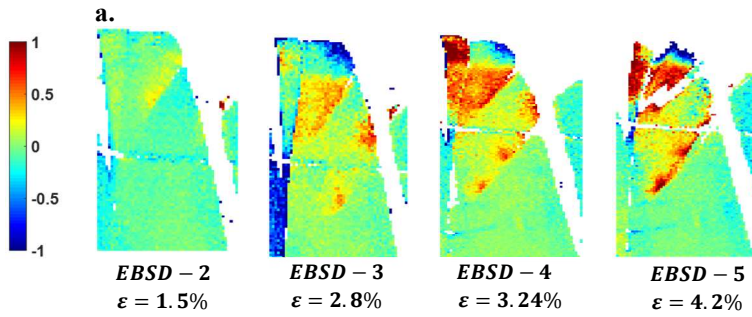 energy (E) as a function of the distance from the pillar's top right corner. This distance is shown with the blue arrow in (c). CPFE results for σ_{13}^L (left) and elastic energy (right) are shown in c, d, f, g, I, and j. In in (e) and (f) calculated resolved shear stress profile along the bottom twin at different applied strains are shown. The distance in (e) and (f) is from the pillar edge along the red arrow as shown in (c). Applied strain for each case is shown at the bottom of the sub-figure and the dashed lines in (c) show the position of the two twins

The distributions of σ_{13}^L and E after elongation of bottom twin under constant applied strain of 2.8% are shown in Fig. 6.3g. It is shown that while σ_{13}^L is negative around the newly added section, it is still positive at the back of the twin. This means that the bottom twin can now thicken from the back of the twin. The σ_{13}^L profile, before and after the twin elongation, is also shown in Fig. 6.3h. It is interesting to report that with more straining, σ_{13}^L within twin become positive, but after shear transfer, it becomes negative within the elongation zone. With further straining of the pillar, it was observed (red circle in Fig. 6.2i) that the highest σ_{13}^L and E happen right at the back of the bottom twin and hence, it is favourable for the bottom twin to thicken. This was also observed in the experiment. The comparison between Fig. 6.3i and 2a indicates that high positive σ_{13}^L exists both at the vicinity of the bottom twin and close to top twin. Further, high elastic energy is accumulated close to the top twin and it is possible that thickening of the bottom twin is accompanied with elongation or thickening of the top twin. At this stage, in CPFE simulation, the thickness of the bottom twin were increased by a factor of two. This step was followed by further straining to 4.2%. The distributions of σ_{13}^L and E at this strain are shown in Fig. 6.3j. It is clear that at this strain there is no driving force for having the

bottom twin elongated or thicken. Meanwhile, σ_{13}^L and E are quite high closer to the top twin. This is in agreement with the experiment where at this stage it was observed that the top twin elongates and thickens.

6.5 Conclusion

With the aim of understanding the mechanism of nucleation, propagation, and thickening of twins as well as the 3D features inherent in such processes, deformation of a titanium micro-pillar was modeled. It is shown that twins nucleated at the locations where energy and twin resolved shear stress are maximum. Once twin nucleated, shear stress at the twin tip is positive and provides enough driving force for twin elongation. It is shown that for short twins, this resolved shear stress on the twin tail is quite negative and twins do not tend to thicken, yet tend to elongate. With applying more strain and as a twin elongates, the local resolved shear stress in the back of the twin becomes positive which provides enough driving force for twin thickening

References

[1] D.W. Brown, I.J. Beyerlein, T.A. Sisneros, B. Clausen, C.N. Tomé, Role of twinning and slip during compressive deformation of beryllium as a function of strain rate, Int. J. Plast. 29 (2012) 120–135. https://doi.org/https://doi.org/10.1016/j.ijplas.2011.08.006.

[2] B.M. Morrow, R.A. Lebensohn, C.P. Trujillo, D.T. Martinez, F.L. Addessio, C.A. Bronkhorst, T. Lookman, E.K. Cerreta, Characterization and modeling of mechanical behavior of single crystal titanium deformed by split-Hopkinson pressure bar, Int. J. Plast. 82 (2016) 225–240. https://doi.org/https://doi.org/10.1016/j.ijplas.2016.03.006.

[3] A. Kauffmann, J. Freudenberger, D. Geissler, S. Yin, W. Schillinger, V.S. Sarma, H. Bahmanpour, R. Scattergood, M.S. Khoshkhoo, H. Wendrock, C.C. Koch, J. Eckert, L. Schultz, Severe deformation twinning in pure copper by cryogenic wire drawing, Acta Mater. 59 (2011) 7816–7823.

https://doi.org/https://doi.org/10.1016/j.actamat.2011.08.042.

[4] S. Xu, C. Schuman, J.-S. Lecomte, Accommodative $10\bar{1}2$ twins at high angle grain boundaries in rolled pure titanium, Scr. Mater. 116 (2016) 152–156. https://doi.org/https://doi.org/10.1016/j.scriptamat.2016.02.005.

[5] I.J. Beyerlein, C.N. Tome, A probabilistic twin nucleation model for HCP polycrystalline metals, Proc. R. Soc. A Math. Phys. Eng. Sci. 466 (2010) 2517–2544. https://doi.org/10.1098/rspa.2009.0661.

[6] H. Abdolvand, M.R. Daymond, Multi-scale modeling and experimental study of twin inception and propagation in hexagonal close-packed materials using a crystal plasticity finite element approach; Part II: Local behavior, J. Mech. Phys. Solids. 61 (2013) 803–818. https://doi.org/10.1016/j.jmps.2012.10.017.

[7] H. Abdolvand, M.R. Daymond, Multi-scale modeling and experimental study of twin inception and propagation in hexagonal close-packed materials using a crystal plasticity finite element approach—Part I: Average behavior, J. Mech. Phys. Solids. 61 (2013) 783–802. https://doi.org/https://doi.org/10.1016/j.jmps.2012.10.013.

[8] M.H. Yoo, J.K. Lee, Deformation twinning in h.c.p. metals and alloys, Philos. Mag. A. 63 (1991) 987–1000. https://doi.org/10.1080/01418619108213931.

[9] M. Arul Kumar, A.K. Kanjarla, S.R. Niezgoda, R.A. Lebensohn, C.N. Tomé, Numerical study of the stress state of a deformation twin in magnesium, Acta Mater. 84 (2015) 349–358. https://doi.org/10.1016/j.actamat.2014.10.048.

[10] M.A. Kumar, I.J. Beyerlein, C.N. Tom, Acta Materialia Effect of local stress fi elds on twin characteristics in HCP metals, Acta Mater. 116 (2016) 143–154. https://doi.org/10.1016/j.actamat.2016.06.042.

[11] J. Cheng, S. Ghosh, Crystal plasticity finite element modeling of discrete twin evolution in polycrystalline magnesium, J. Mech. Phys. Solids. (2016). https://doi.org/10.1016/j.jmps.2016.12.008.

[12] J. Cheng, J. Shen, R.K. Mishra, S. Ghosh, Discrete twin evolution in Mg alloys using a novel crystal plasticity finite element model, Acta Mater. 149 (2018) 142–153. https://doi.org/https://doi.org/10.1016/j.actamat.2018.02.032.

[13] J. Cheng, S. Ghosh, A crystal plasticity FE model for deformation with twin

nucleation in magnesium alloys, Int. J. Plast. 67 (2015) 148–170. https://doi.org/10.1016/j.ijplas.2014.10.005.

[14] J. Cheng, S. Ghosh, Crystal plasticity finite element modeling of discrete twin evolution in polycrystalline magnesium, J. Mech. Phys. Solids. 99 (2017) 512–538. https://doi.org/https://doi.org/10.1016/j.jmps.2016.12.008.

[15] M.A. Kumar, I.J. Beyerlein, R.J. Mccabe, C.N. Tome, Grain neighbour effects on twin transmission in hexagonal close-packed materials ´ 1, Nat. Commun. 7 (2016) 13826. https://doi.org/10.1038/ncomms13826.

[16] Y. Liu, N. Li, M. Arul Kumar, S. Pathak, J. Wang, R.J. McCabe, N.A. Mara, C.N. Tomé, Experimentally quantifying critical stresses associated with basal slip and twinning in magnesium using micropillars, Acta Mater. 135 (2017) 411–421. https://doi.org/10.1016/j.actamat.2017.06.008.

[17] H. Abdolvand, A.J. Wilkinson, Assessment of residual stress fields at deformation twin tips and the surrounding environments, Acta Mater. 105 (2016) 219–231. https://doi.org/10.1016/j.actamat.2015.11.036.

[18] Y. Guo, J. Schwiedrzik, J. Michler, X. Maeder, On the nucleation and growth of twin in commercial purity titanium: In situ investigation of the local stress field and dislocation density distribution, Acta Mater. 120 (2016) 292–301. https://doi.org/10.1016/j.actamat.2016.08.073.

[19] A.J. Wilkinson, G. Meaden, D.J. Dingley, High-resolution elastic strain measurement from electron backscatter diffraction patterns: New levels of sensitivity, Ultramicroscopy. 106 (2006) 307–313. https://doi.org/10.1016/j.ultramic.2005.10.001.

[20] T.B. Britton, a. J. Wilkinson, High resolution electron backscatter diffraction measurements of elastic strain variations in the presence of larger lattice rotations, Ultramicroscopy. 114 (2012) 82–95. https://doi.org/10.1016/j.ultramic.2012.01.004.

[21] H. Abdolvand, A.J. Wilkinson, On the effects of reorientation and shear transfer during twin formation: Comparison between high resolution electron backscatter diffraction experiments and a crystal plasticity finite element model, Int. J. Plast. 84 (2016) 160–182. https://doi.org/10.1016/j.ijplas.2016.05.006.

[22] R.J. Asaro, a. Needleman, Texture development and strain hardening in rate

dependent polycrystals, Acta Metall. 33 (1984) 923–953. https://doi.org/10.1016/0001-6160(85)90188-9.

[23] L. Wang, R.I. Barabash, Y. Yang, T.R. Bieler, M.A. Crimp, P. Eisenlohr, W. Liu, G.E. Ice, Experimental characterization and crystal plasticity modeling of heterogeneous deformation in polycrystalline α-Ti, Metall. Mater. Trans. A Phys. Metall. Mater. Sci. 42 (2011) 626–635. https://doi.org/10.1007/s11661-010-02498.

[24] R.Y. Zhang, M.R. Daymond, R. a. Holt, A finite element model of deformation twinning in zirconium, Mater. Sci. Eng. A. 473 (2008) 139–146. https://doi.org/10.1016/j.msea.2007.04.021.

Chapter 7

7 Conclusions and future work

7.1 Conclusions

A crystal plasticity finite element model was updated by integrating the strain-gradients and the resulting dislocation density terms (GNDs and SSDs) into the hardening law of slip systems. Two different methods were used for determining the evolution of the GND densities during plastic deformation of HCP zirconium. The results from the model were compared to those from neutron diffraction and HR-EBSD experiments. Further, the capability of the model in capturing the formation of localized deformation zones in unirradiated zirconium was examined. After validating the model for unirradiated zirconium, the model was further updated by integrating an irradiation growth subroutine with the updated hardening law. The results of the irradiation model were compared against those measured for neutron-irradiated single and polycrystalline zirconium specimens. The main conclusions of this study are summarized here.

The steps taken for updating the model with a non-local hardening law were discussed in Chapter 3. The numerical results from both conventional and non-local CPFE models were compared. It was shown that both conventional and non-local CPFE models can adequately capture the macroscopic stress-strain curves, as well as the evolution of internal lattice strains measured using neutron diffraction. However, the predicted elastic lattice rotation fields from the non-local model slightly deviate from those calculated by the conventional model. For the studied microstructure, the stress distributions within individual grains from both non-local and conventional models are shown to be quite

similar. However, the magnitudes of localized stresses were in better agreement with those measured by the HR-EBSD method. The difference between the conventional and non-local models are shown to be more pronounced in the regions where there are sharp strain gradients, e.g., in the vicinity of the twin tips and grain boundaries. The calculated GND densities in such areas are shown to be in good agreement with those measured by the HR-EBSD method.

In chapter 4, two different approaches for the determination of GND densities in the non-local CPFE model were compared. The non-local CPFE models revealed the formation of localized GND lines, parallel to the slip bands observed in the deformed specimen. While the GND densities obtained from the minimization-based approach (Method II) were uniformly distributed among all slip systems, the use of direct method (Method I) led to the non-uniform distribution of GNDs on the slip systems. It was shown that the calculated GND densities from the direct method are proportional to the calculated activity for the slip systems. The magnitude of the GND density calculated using Method II was larger than the one from Method I. However, the calculated total dislocation density, i.e., GND plus SSD, from the two methods was almost the same for the studied microstructure with the average grain size of 50 μm. As a result, the trends observed for the calculated stresses and lattice rotations at the grain level were also the same. However, it was shown that the calculated stresses from the two methods were different for smaller grains. A threshold value for the grain size was identified below which the geometrical effects became significant. This critical grain size was higher in Method II, compared to Method I. The dislocation-based hardening law used here was SSD driven for larger grains and GND driven for smaller grains and accurate implementation of both mechanisms is shown to be important when different grain sizes exist in the microstructure.

In chapter 5, it was shown that the irradiation CPFE model can capture the evolution of growth strains for both annealed single crystal and cold worked polycrystal models. For the polycrystal models, the magnitudes of the calculated growth strains increased with increasing the prior cold work or decreasing the average grain size. Special attention was given to the distribution of growth strain. A noticeable non-uniformity for the growth strain was observed among different grains and within individual grains. It was shown that the growth strain was mainly accommodated by smaller grains, in which dislocation line densities were higher. CPFE results demonstrated the localization of growth strains both at grain boundaries and in deformation zones. The magnitude of localized growth strain was shown to be proportional to the amount of prior cold work and, inversely proportional to the grain size. Finally, it was shown that the effect of the grain boundary sink strength on the calculated growth strain in the vicinity of the grain boundary was more significant for un-deformed crystals, compared to the deformed ones.

In chapter 6, the process of nucleation, propagation, and thickening of twins was modeled for a titanium micro-pillar. It was shown that twins nucleate at the locations where both elastic energy and twin resolved shear stress were maximum. The simulation results showed that once a twin is nucleated, the shear stress at the twin tip is positive, resulting in twin elongation. However, the resolved shear stress on the twin tail is initially negative, preventing the twin from thickening. As the deformation continues, the local resolved shear stress in the back of the twin becomes positive, providing enough driving force for twin thickening.

This research presented a dislocation-based CPFE model, which considers the non-local effects by calculating the GND densities as a function of the strain gradient. This capability is important when the localized plastic deformation at the vicinity of the micro-scale features is interested, e.g. twins, cracks, and precipitates. In addition, the size

dependency aspect of the current model is important, when the investigated polycrystal has the average grain size of less than ~10 μm, e.g. Zr-2.5Nb pressure tubes of CANDU nuclear reactors fuel channels.

7.2 Future work

Other irradiation-induced deformation mechanisms can be added to the updated CPFE model. Therefore, the following studies are recommended:

1. In order to accurately predict the possible contact between the pressure tube and calandria tube, both irradiation growth and irradiation-enhanced creep should be modeled, yet the effects of the latter were ignored in this study. Therefore, it is necessary to update the model by incorporating the effects of irradiation creep.

2. The formation of the slip bands can be simulated using higher-order strain gradient crystal plasticity models. The incorporation of higher order terms to the CPFE model can be in the scope of the future studies.

Curriculum Vitae

Name: Omid Sedaghat

Post-secondary Education and Degrees:

Iran university of science and technology
Tehran, Iran
2004-2009 B.Sc.

Technical university of Eindhoven
Eindhoven, the Netherlands
2009-2011 M.Sc.

The University of Western Ontario
London, Ontario, Canada
2018-2022 Ph.D.

Publications:

- O. Sedaghat, H. Abdolvand, Irradiation growth strain localization in α-zirconium: A numerical study using non-local crystal plasticity finite element modeling, Under review.

- O. Sedaghat, H. Abdolvand, Strain-gradient crystal plasticity finite element modeling of slip band formation in α-zirconium, Crystals, 11-1382, 2021.

- O. Sedaghat, H. Abdolvand, A non-local crystal plasticity constitutive model for hexagonal close-packed polycrystals, International Journal of Plasticity, 136, 2021.

- H. Abdolvand, O. Sedaghat, Y. Guo, Nucleation and growth of twins in titanium: Elastic energy and stress fields at the vicinity of twins, Materialia, 2018.